

Department of Civil and Structural Engineering

Orientation of short steel fibres in concrete: measuring and modelling

Marika Eik



Orientation of short steel fibres in concrete: measuring and modelling

Marika Eik

Dissertation for the Doctoral degree to be presented with due permissions of the School of Engineering, Aalto University and Tallinn University of Technology for public examination and debate in Auditorium R1 (Rakentajanaukio 4A) at the Aalto University (Espoo, Finland) on the 4th of April 2014 at 12 noon.

**Aalto University
School of Engineering**

Tallinn University of Technology

Supervising professor

Professor Jari Puttonen, Aalto University, Finland

Thesis advisor

Dr. rer. nat. Heiko Herrmann, Tallinn University of Technology,
Estonia

Preliminary examiners

Professor Holm Altenbach, Faculty of Mechanical Engineering, Otto-
von Guericke-Universität Magdeburg, Germany
Professor Kenneth Runesson, Department of Applied Mechanics,
Chalmers University of Technology, Sweden

Opponent

Professor Karin Lundgren, Department of Civil and Environmental
Engineering, Chalmers University of Technology, Sweden

Aalto University publication series

DOCTORAL DISSERTATIONS 28/2014

© Marika Eik

ISBN 978-952-60-5591-6

ISBN 978-952-60-5592-3 (pdf)

ISBN 978-9949-23-594-0 (pdf, TUT)

ISSN-L 1799-4934

ISSN 1799-4934 (printed)

ISSN 1799-4942 (pdf)

<http://urn.fi/URN:ISBN:978-952-60-5592-3>

Unigrafia Oy
Helsinki 2014

Finland



THESIS ON CIVIL ENGINEERING F45

**Orientation of short steel fibres
in concrete: measuring and
modelling**

MARIKA EIK

TALLINN UNIVERSITY OF TECHNOLOGY
Faculty of Civil Engineering
Institute of Cybernetics
Mechanics and Applied Mathematics Department

This dissertation was accepted for the defense of the degree of Doctor of Philosophy in Engineering on March 3rd, 2014.

Supervisor: Heiko Herrmann, Dr. rer. nat.
Mechanics and Applied Mathematics Department, Institute of Cybernetics,
Tallinn University of Technology, Tallinn, Estonia

Co-Supervisor: Jari Puttonen, Professor
Department of Civil and Structural Engineering ,
Aalto University School of Engineering, Espoo, Finland

Opponents: Holm Altenbach, Professor
Faculty of Mechanical Engineering,
Otto-von Guericke-Universität Magdeburg, Germany

Karin Lundgren, Professor
Opponent on the behalf of Aalto University

Defense of the thesis: April 4th, 2014

Declaration:

Hereby I declare that this doctoral thesis, my original investigation and achievement, submitted for the doctoral degree at Tallinn University of Technology and at Aalto University School of Engineering has not been submitted for doctoral or equivalent academic degree.

Marika Eik

EHITUS F45

**Metallist lühikiudude
orientatsioon betoonis:
mõõtmine ja modelleerimine**

MARIKA EIK

Author

Marika Eik

Name of the doctoral dissertation

Orientation of short steel fibres in concrete: measuring and modelling

Publisher School of Engineering

Unit Department of Civil and Structural Engineering

Series Aalto University publication series DOCTORAL DISSERTATIONS 28/2014

Field of research Structural Engineering

Manuscript submitted 8 November 2013

Date of the defence 4 April 2014

Permission to publish granted (date) 14 February 2014

Language English

Monograph

Article dissertation (summary + original articles)

Abstract

This research focuses on a cementitious composite formed by mixing of concrete matrix with short steel fibres, SFRC. This composite is quite extensively employed in the construction industry, for example in floors resting on soil and even in some load-bearing structures, such as floor-slabs. The complexity of SFRC is the presence of the anisotropic behaviour occurring due to different alignments of short fibres.

The examinations performed comprise two research branches: measuring of fibre orientations from the hardened concrete matrix and modelling of composite properties considering the orientation distribution of fibres. Two methods of measuring fibre orientations are developed: slicing method and X-ray micro-tomography. Parts extracted from the full-size floor-slabs are used as samples. The slicing with photometry approach is improved by DC-conductivity testing joined with image analysis. X-ray micro-tomography is performed on sufficiently large samples and the orientation of fibres is specified by the analysis of 3D voxel images of scanned fibres. The received measuring results proved that both DC-conductivity testing combined with photometry and X-ray micro-tomography have high accuracy and they can be applied in defining fibre orientations from real concrete samples reliably.

The material model developed for one meso-volume element of SFRC is based on an orthotropic hyperelastic material model where the second-order terms of the strain energy function are employed resulting in orthotropic St. Venant-Kirchhoff model. The orthotropic meso-symmetry of the composite is modelled by the structural tensors based on the eigenvectors of the second-order alignment tensor, which represent the dominating alignment of fibres. The material model developed for SFRC consists of an isotropic part presenting the concrete and the orthotropic part including the influence of short steel fibres. The orientation distribution function of fibres is utilized to evaluate the orthotropic effect in the defined material symmetry directions. The advantage of the material model developed is that it uses the full orientation information of fibres and employs tensor quantities, which are independent of any reference frame. Finally, the implementation of the model is demonstrated by examples based on fibre orientations measured from test samples.

Keywords short steel fibre orientation, constitutive mappings, slicing, micro-computed tomography, steel fibre reinforced concrete

ISBN (printed) 978-952-60-5591-6

ISBN (pdf) 978-952-60-5592-3

ISSN-L 1799-4934

ISSN (printed) 1799-4934

ISSN (pdf) 1799-4942

Location of publisher Helsinki

Location of printing Helsinki

Year 2014

Pages 226

urn <http://urn.fi/URN:ISBN:978-952-60-5592-3>

Tekijä

Marika Eik

Väitöskirjan nimi

Betoniin lisättyjen lyhyiden teräskuitujen suuntautuneisuuden mittaaminen ja mallintaminen

Julkaisija Insinööritieteiden korkeakoulu**Yksikkö** Rakennustekniikan laitos**Sarja** Aalto University publication series DOCTORAL DISSERTATIONS 28/2014**Tutkimusala** Talonrakennustekniikka**Käsitteilyajankohdan pvm** 08.11.2013**Väitöspäivä** 04.04.2014**Julkaisuluvan myöntämispäivä** 14.02.2014**Kieli** Englanti **Monografia** **Yhdistelmäväitöskirja (yhteenvedo-osa + erillisartikkelit)****Tiivistelmä**

Tutkimuksessa tarkastellaan betonin ja lyhyiden teräskuitujen muodostamaa yhdistelmäateriaalia, jota on laajasti käytetty rakennusallalla esimerkiksi maanvaraisissa lattioissa ja Suomen ulkopuolella myös kantavissa välipohjalaatoissa. Tämän yhdistelmäateriaalin toiminnan arvioinnissa haasteet liittyvät materiaalin anisotrooppisuuteen, joka aiheutuu kuitujen suuntautuneisuuden ja määrän vaihteluista betonissa.

Tutkimus jakaantui kahteen pääosaan, joista ensimmäisessä tarkasteltiin kuitujen suuntaisuuden määrittämistä kovettuneesta betonista ja toisessa kehitettiin menetelmä kuitujen orientaation huomioon ottamiseksi materiaalimallissa. Kuitujen suunnan määritykseen työssä syntyi kaksi menetelyä, jotka perustuivat joko näyteleikkauksen viipalointiin tai röntgensädeä hyödyntävään mikrotomografiaan. Menetelmiä kehitettiin testikappaleilla, jotka oli otettu mitoiltaan ja valmistustavaltaan todellisia välipohjalaattoja vastaavista koerakenteista. Viipaleiden fotometriasta tarkastelua parannettiin testaamalla pisteittäin viipaleiden pintojen välistä sähkönjohtavuutta robottiohjatulla tasasähkölähteellä. Mikrotomografiamittaus suoritettiin riittävän suurilla koekappaleilla, joista kuitujen suuntautuneisuus määritettiin analysoimalla kolmiulotteisia kuvamatriiseja. Saadut mittaustulokset osoittivat sekä fotometrian yhdistettynä tasasähkön johtavuuteen että mikrotomografian olevan tarkkoja menetelmiä, joita voidaan luotettavasti soveltaa kuitujen suuntautuneisuuden määrittämiseen todellisista betonikappaleista.

Kehitetty materiaalimalli kuitubetonin mesotilavuutta kuvaavalle osuudelle perustuu hyperelastiseen materiaaliin, jossa sovelletaan muodonmuutosenergian toisen kertaluvun termejä. Yhdistelmäateriaalin symmetria on kuvattu toisen kertaluvun suuntautuneisuustensorin ominaisvektoreilla, jolloin isotrooppinen St. Venat-Kirchhoff-malli voidaan täydentää ominaisvektoreista muodostetuilla rakennetensoreilla. Tuloksena saadaan ortotropinen St. Venant-Kirchhoff-materiaali, jonka isotrooppinen osa kuvaa betonin ortotropian kuvattua kuitujen vaikutusta. Kuitujen suuntautuneisuuden tiheysfunktioita hyödynnetään laskettaessa suunnasta riippuvien kimmovakioiden vaikutusta määrättyihin symmetriasuuntiin. Johdetun materiaalimallin etuna on, että siinä hyödynnetään kaikki tieto kuitujen suuntautuneisuudesta soveltaen tensorisuureita, jotka ovat valitusta koordinaatistosta riippumattomia. Lopuksi mallin soveltamista on havainnollistettu esimerkeillä, joissa on hyödynnetty koekappaleista mitattuja tietoja kuitujen suuntautuneisuudesta.

Avainsanat lyhyiden teräskuitujen suuntautuminen, konstitutiivinen malli, viipalointi, mikrotomografia, teräskuitubetoni

ISBN (painettu) 978-952-60-5591-6**ISBN (pdf)** 978-952-60-5592-3**ISSN-L** 1799-4934**ISSN (painettu)** 1799-4934**ISSN (pdf)** 1799-4942**Julkaisupaikka** Helsinki**Painopaikka** Helsinki**Vuosi** 2014**Sivumäärä** 226**urn** <http://urn.fi/URN:ISBN:978-952-60-5592-3>

Kokkuvõte

Käesolev väitekiri käsitleb tsemendipõhist komposiitmaterjali, mis on moodustatud betoonmassi (matriitsi) ja lühikeste teraskiudude kokku segamisega, mille tulemuseks on teraskiudbetoon. See komposiitmaterjal on juba laialdaselt kasutusel ehituskonstruksioonides, näiteks tööstuspõrandates ning isegi mõnedes kandekonstruksioonides nagu näiteks vahelaeplaadid. Teraskiudbetooni keerulisus seisneb tema anisotroopsetes omadustes, mis tulenevad lühikiudude erineva orientatsiooni jaotusest matriitsis.

Teostatud uuringud hõlmavad kahte teadusharu: lühikeste teraskiudude orientatsiooni jaotuse mõõtmise kivistunud betoonmatriitsis ning komposiidi omaduste modelleerimist võttes arvesse kiudude orientatsiooni jaotust. Uurimistöö käigus on arendatud kahte meetodit lühikiudude orientatsiooni jaotuse mõõtmiseks: viilutamine ja mikro-kompuutertomograafia. Katsekehadeks on kasutatud konstruktsiooni osasid, mis olid eraldatud täismõõtmelistest vahelaeplaatidest. Viilutamise ja fotomeetria lähenemine on täiustatud alalisvoolu juhtivuse mõõtmisega, mis omaette on kombineeritud fotoanalüüsiga. Mikro-kompuutertomograafia on teostatud piisavalt suurte katsekehadel ning lühikiudude orientatsioon on määratud analüüsides 3D voksel pilte skanneeritud kiududest. Saadud mõõtmistulemused on tõestanud, et mõlemad mõõtmismeetodid, st alalisvoolu juhtivuse mõõtmine kombineerituna fotoanalüüsiga ning mikro-kompuutertomograafia, omavad kõrget täpsust mõõtmistel ja neid saab usaldusväärselt kasutada terasest lühikiudude orientatsiooni jaotuse määramisel reaalses katsekehades.

Teadustöö käigus välja töötatud materjalimudel ühe teraskiudbetooni meso-ruumelemendi jaoks baseerub ortotroopsetel hüperelastsetel materjalimudelil, kus deformatsioonienergia funktsioonis kasutatakse teist järku liikmeid, mille tulemuseks on ortotroopne St. Venant-Kirchhoff'i mudel. Komposiidi ortotroopne meso-sümmeetria on modelleeritud struktuursete tensorite abil, mis on moodustatud teist järku joonduvustensori omavektoritest, sest joonduvustensor esitab

lühikiudude domineerivate orientatsioonide suundi. Ortotroopset St. Venant-Kirchhoff'i mudelit saab kasutada isotroopse juhtumi jaoks, kuna suunast sõltuvad struktuursed tensorid taanduvad erisuuna puudumisel. Sellest tulenevalt koosneb materjalimudel ühe teraskiudbetooni meso-ruumelemendi jaoks isotroopsest osast, mis kirjeldab betoonmatriitsi ning ortotroopsest osast, mis kirjeldab terasest lühikiudude mõju. Lühikiudude orientatsiooni jaotusfunktsioon on rakendatud komposiidi ortotroopse meso-elastsuse hindamisel meso-sümmeetria suunades. Formuleeritud materjalimudeli eeliseks on asjaolu, et ta rakendab täieliku infot lühikiu orientatsiooni kohta (sfäärilised koordinaadid) ning kasutab tensorsuurusi, mis ei sõltu koordinatsüsteemi valikust. Viimaks, formuleeritud mudeli rakendamine on esitatud näidetega, mis baseeruvad katsekehades mõõdetud lühikiudude orientatsiooni jaotusel.

Preface

This doctoral thesis is conducted under a convention for the joint supervision of thesis at Aalto University (Finland) and Tallinn University of Technology (Estonia). In Aalto University the research work was carried out at the School of Engineering, Department of Civil and Structural Engineering and in Tallinn University of Technology (TUT) at the Faculty of Civil Engineering, Institute of Cybernetics. The doctoral study at TUT was commenced in the year of 2007 and at Aalto in 2009. The experimental part of the work was implemented in the Testing Hall of Structural Engineering in Aalto University, in the X-ray micro-tomography laboratory, Department of Physics in Helsinki University, and in the Centre of Biorobotics in TUT. The tested real-size floor-slabs were cast and provided for the research by *Rudus Oy*. This research work was possible due to the support of the Doctoral Programme of the Built Environment (RYM-TO) funded through the Academy of Finland and due to the funding from the European Regional Development Fund, in particular through funding for the "Centre for Nonlinear Studies" as an Estonian national centre of excellence. In addition, the research has received funding from Estonian Ministry of Education. Furthermore, Jaanus Otsa doctoral Scholarship of TUT Development Foundation and TUT Alumni Association is gratefully appreciated.

I cordially thank my supervisors Professor Jari Puttonen and Dr. Heiko Herrmann, who believed in me and gave me a real opportunity to plunge into the world of science and to achieve positive results. Through the discussions with my supervisors and with the knowledge obtained during the study, I realised that the science is a key enabling a person to discover and understand the world around. This scientific work is a path that I overcame together with my supervisors and on which I have met so many good people. I express my gratitude to the pre-examiners Professor Kenneth Runesson and Professor Holm Altenbach for their professionalism, useful comments and objectivity in the evaluation of my thesis. I appreciate the opponent Professor Karin

Lundgren's interest in my research work, as well as the time she is willing to dedicate to its study.

I am very thankful to Andrus Räämet, who introduced me to Professor Jari Puttonen, as well as to Madis Listak, who organised a meeting with Dr. Heiko Herrmann. Thereby, these contacts resulted in a joint research work, which involved both Universities. I would like to thank Professor Andrus Salupere, Academician Jüri Engelbrecht, Professor Roode Liias, and Professor Juha Paavola, who supported and contributed to the idea of joint supervision of doctoral thesis. I cannot forget the help and good attitude of all administrative staff that I met in both Universities as their contribution was also necessary and important for signing the joint-supervision agreement. My special gratitude to Academician Jüri Engelbrecht for having acquainted me with an infinite variety and beauty of physical processes, as well as with the modelling possibilities of various natural phenomena. I would like to thank Professor Andrus Salupere for the discussions on topics of continuum mechanics. Furthermore, I am very thankful to Pentti Lumme for the maintenance of the experimental part of the study as well as for his good advises and interest in my research achievements. The experimental part of the study would have been impossible without the help of Veli-Antti Hakala and his colleagues from the Testing Hall in Aalto University, without the assistance of microtomography group Jussi-Petteri Suuronen, Aki Kallonen and Professor Ritva Serimaa from Helsinki University, and also without the experience of Karl Lõhmus, Martin Tigasson and Madis Listak from the Centre of Biorobotics in TUT. Special thanks to all my teachers who guided me on my way to the knowledge and also to all my colleagues from the Department of Civil and Structural Engineering in Aalto, from the Institute of Cybernetics and from the Faculty of Civil Engineering in TUT.

My special appreciation to my family and to my beloved son, who is accompanying my scientific growth already for 15 years. I am grateful to him for his endorsement and assistance that he is always willing to give me. The support and understanding from my mother and father are also gratefully appreciated. I am also thankful to my cousin Inga, her husband Jörgen and also to all my friends, who also worried and followed the progress of my research activity.

Scientia potentia est

Helsinki, March 3, 2014,

Contents

Preface	i
Contents	iii
List of Publications	v
Author's Contribution	vii
List of Conference Presentations	ix
List of Figures	xi
List of Tables	xvii
Notations and definitions	xix
1. Introduction	1
1.1 Unknowns and open questions with SFRC	3
1.2 Research goals and implementations	5
2. Methodology for measuring fibre orientations	9
2.1 Overview of measuring techniques	9
2.2 Selection of measuring methods	12
2.3 Slicing method as a combination of DC-conductivity testing with photometry	12
2.3.1 Experimental set up	13
2.3.2 Slicing with photometry	16
2.3.3 Slicing with DC-conductivity joined with photometry .	19
2.4 X-ray micro-tomography method (μ CT)	21
2.4.1 Procedure set up	21
2.4.2 Fibre orientation analysis	23
2.5 Summary of developed and implemented measuring methods .	24
	iii

3. Fibre orientation distributions in tested floor-slabs	29
3.1 Density distribution of the inclination angle θ	29
3.2 Variations of fibre orientation distributions along the X - and Y -axes of the slabs	32
3.3 Variations of fibre orientation distributions along the Z -axis of the slabs	34
4. Constitutive mappings	37
4.1 General terms and conditions for material models	37
4.2 Behaviour of SFRC	37
4.3 Orthotropic elasticity of one meso-volume element of SFRC . .	39
4.3.1 Modelling of isotropic concrete matrix and orthotropic influence of short steel fibres	40
4.3.2 State space for SFRC	46
4.3.3 Orientation-weighted meso-elasticity of fibres in mate- rial meso-symmetry axes	47
4.4 Constitutive relation for one meso-volume element of SFRC . .	49
4.5 Example calculations of orientation-weighted 4 th order meso- elasticity tensors based on experimental data	51
4.6 Application areas for the developed material model of SFRC . .	55
4.6.1 Application in numerical calculations	56
4.6.2 Application in production technology	56
5. Conclusions and future prospects	59
Bibliography	63
A. Appendicies	71
A.1 Orientation distribution function as a spherical harmonic function	71
A.2 Density distribution of the inclination angle θ	77
A.3 Variations of fibre orientation distributions along the X - and Y -axes of the slabs	78
A.4 Measured fibre alignments characterized by the eigenvectors of the 2 nd order alignment tensor in the tested slabs	83
A.5 Measured fibre orientation distribution functions in the tested slabs	86
Curriculum Vitae	93
Publications	105

List of Publications

This thesis consists of an overview and of the following publications which are referred to in the text by their Roman numerals.

- I** M. Eik and J. Puttonen. Challenges of steel fibre reinforced concrete in load bearing structures. *Rakenteiden mekaniikka (Journal of Structural Mechanics)*, 44, 1, 44-64, <http://rmseura.tkk.fi/rmlehti/2011/nro1/>, June 2011.
- II** H. Herrmann and M. Eik. Some comments on the theory of short fibre reinforced materials. *Proceedings of the Estonian Academy of Sciences*, 60, 3, 179-183, <http://dx.doi.org/10.3176/proc.2011.3.06>, June 2011.
- III** M. Eik and H. Herrmann. Raytraced images for testing the reconstruction of fibre orientation distributions. *Proceedings of the Estonian Academy of Sciences*, 61, 2, 128-136, <http://dx.doi.org/10.3176/proc.2012.2.05>, June 2012.
- IV** J.-P. Suuronen, A. Kallonen, M. Eik, J. Puttonen, R. Serimaa and H. Herrmann. Analysis of short fibres orientation in steel fibre reinforced concrete (SFRC) using X-ray tomography. *Journal of Materials Science*, 48, 3, 1358-1367, <http://dx.doi.org/10.1007/s10853-012-6882-4>, February 2013.
- V** M. Eik, K. Lõhmus, M. Tigasson, M. Listak, J. Puttonen and H. Herrmann. DC-conductivity testing combined with photometry for measuring fibre orientations in SFRC. *Journal of Materials Science*, 48, 10, 3745-3759, <http://dx.doi.org/10.1007/s10853-013-7174-3>, May 2013.
- VI** M. Eik, J. Puttonen and H. Herrmann. Fibre orientation phenomenon in concrete composites: measuring and theoretical modelling. *7th In-*

*ternational Conference FIBRE CONCRETE 2013, Technology, Design,
Application; Conference Proceedings, 1-4, September 2013.*

Author's Contribution

Publication I: "Challenges of steel fibre reinforced concrete in load bearing structures"

The author provided the ideas and wrote the paper with input from the coauthor.

Publication II: "Some comments on the theory of short fibre reinforced materials"

The author identified some of the weak points in present theories, provided knowledge within the field of civil engineering and wrote the paper together with the coauthor.

Publication III: "Raytraced images for testing the reconstruction of fibre orientation distributions"

The author provided knowledge within the field of civil engineering, performed image analysis and wrote paper together with the coauthor.

Publication IV: "Analysis of short fibres orientation in steel fibre reinforced concrete (SFRC) using X-ray tomography"

The author performed image analysis and statistics, provided knowledge within the field of civil engineering and wrote the paper together with the coauthors.

Publication V: “DC-conductivity testing combined with photometry for measuring fibre orientations in SFRC”

The author performed image processing, analysis and statistics, provided knowledge within the field of civil engineering and wrote the paper together with the coauthors.

Publication VI: “Fibre orientation phenomenon in concrete composites: measuring and theoretical modelling”

The author provided some of the ideas—in particular the idea for orthotropy based on eigenvectors (together with HH) and the idea and reasoning for linear elasticity (together with JP)—provided knowledge within the field of civil engineering and wrote the paper together with the coauthors.

List of Conference Presentations

- I M. Eik and H. Herrmann; **Measuring Fibre Orientation in Steel Fibre Reinforced Concrete**; 16th International Conference on Composite Structures (ICCS16), Porto, Portugal, June 28 - 30, 2011
- II M. Eik, J. Puttonen and H. Herrmann; **Orientation distribution of fibres in short fibre reinforced concrete: evaluation and introduction to constitutive relations**; 8th European Solid Mechanics Conference (ESMC16), Graz, Austria, July 9 - 13, 2012
- III M. Eik, J. Puttonen and H. Herrmann; **Fibre orientation phenomenon in concrete composites: measuring and theoretical modelling**; 7th International Conference FIBRE CONCRETE 2013 Technology, Design, Application, Prague, Czech Republic, September 12 - 13, 2013

List of Figures

1.1	Short fibres used for the reinforcement of concrete matrix. . . .	1
1.2	Cross-section of a cast SFRC structure. Concrete reinforced by short hooked-end steel fibres, SFRC.	2
1.3	Buildings where SFRC was used for load-bearing structures. . .	2
1.4	The comparison between a reinforced concrete and a SFRC beam. In the SFRC beam the orientation distribution of fibres is not specified.	3
1.5	Representation of a fibre in spherical coordinate system.	4
1.6	Graphical representation of the basic objectives during the research.	8
2.1	Ambiguity in the direction of a fibre in case of photometric analysis.	10
2.2	The casting order and the fibre types used.	13
2.3	Load-deflection diagram of tested floor-slabs during the bending test.	14
2.4	Representation of a floor-slab and sample cuboids. Dimensions in (cm).	14
2.5	The cutting and marking of sample cuboids.	15
2.6	The diamond saw used.	15
2.7	The tools used for photographing slice surfaces.	16
2.8	The positioning and marking of slices.	17
2.9	The identification of the left or right surface of a slice by the colour of a ruler.	17
2.10	Representation of a sample cuboid with slices, see also Fig. 2.8(b).	17
2.11	Image of a slice.	18
2.12	Definition of the orientation angles applying the image analysis.	18
2.13	The scanning robot (side and front view).	20

2.14	The scanning robot in use.	20
2.15	The position of an analysed cylinder in the floor-slab.	21
2.16	The scanner nanotom supplied by Phoenix x-ray Systems.	22
2.17	The representation of μ CT and slicing coordinate systems.	22
2.18	Thresholded volume image of a middle part of a cylinder sample scanned by μ CT. Still showing an artefact in the middle (data courtesy of Aki Kallonen [1]).	23
2.19	The influence of slice thickness on results while tracking the trace of a cut fibre.	24
2.20	Errors connected with the geometry of a fibre.	25
3.1	The coordinate system in the tested slabs and the location of samples.	29
3.2	Statistics of fibre orientations measured by DC-conductivity testing on slice 11 belonging to the cuboid 1.1. Figs. (b), (c) represent the density distribution–solid line–of the inclination angle θ and in-plane angle ϕ respectively. In Fig. (b) the skewness is compared with the Normal distribution–dashed line. In (a) the radius represents the inclination angle θ and in-plane angle ϕ is on circumference.	30
3.3	The effect of the measuring approaches on the probability density distribution of the inclination angle θ and in-plane angle ϕ . A dashed line represents the results received by photometry (cuboid 1.1) and a solid line the results of DC-conductivity testing (slice 11 from cuboid 1.1).	31
3.4	Scatter plots of fibre orientation variations measured by μ CT between the side (cylinder 1A) and centre (cylinder 1B), and along the height of the whole cylinder samples. In (a) the radius represents the inclination angle θ and in-plane angle ϕ is on circumference. Z-axis corresponds to the direction of the tensile stress in a slab, Fig. 3.1.	33

3.5	Fibre orientation variations measured by μ CT along the height of the whole cylinder sample 1A. Figs. (a),(b),(c) represent the statistics for the top; (d),(e),(f) for the middle and (g),(h),(i) for the bottom parts of the cylinder. Figs. (a),(b), (d),(e), (g),(h) represent the density distribution—solid line—of the inclination angle θ and in-plane angle ϕ . In Figs. (a),(d),(g) the skewness is compared with the Normal distribution—dashed blue line. Figs. (c),(f),(i) represent the bivariate densities of the inclination angle θ and in-plane angle ϕ	34
3.6	Differences in the probability density histograms of the inclination angle θ according to the location along the Z axis of the slabs, Fig. 3.1, in the middle sections of the cuboids 1.1–3.2 and cylinder samples 1A–3B. A dashed line represents the results of cuboids measured by photometry and a solid line the results of cylinder samples measured by μ CT.	35
3.7	Differences in the probability density histograms of the inclination angle θ according to the location along the Z axis of the slabs, Fig. 3.1, in the middle sections of the cuboids 4.1–6.2 and cylinder samples 4A–6B. A dashed line represents the results of cuboids measured by photometry and a solid line the results of cylinder samples measured by μ CT.	36
4.1	A bended concrete member. The stage at the very beginning of the formation of cracks in the tension zone. f^{ct} denotes the tension strength of concrete, σ^c is the concrete stress in compression zone, ε^{c1} is the concrete strain in compression, and ε^{ctu} is the concrete ultimate strain in tension.	38
4.2	One meso-volume element of SFRC.	39
4.3	Orthotropic material with three principal material directions $\mathbf{m}^1, \mathbf{m}^2, \mathbf{m}^3$ called as material symmetry axes. $\mathbf{l}^1, \mathbf{l}^2, \mathbf{l}^3$ are the unit vectors along the symmetry axes.	40
4.4	The orientation of a fibre (rod-like particle) in space. θ is the inclination angle, $\theta \in (0^\circ, 180^\circ)$, ϕ is the in-plane angle, $\phi \in (0^\circ, 360^\circ)$. In μ CT scanning the ranges of definitions $\theta \in (0^\circ, 90^\circ)$ and $\phi \in (0^\circ, 360^\circ)$ are used.	43
4.5	A macroscopic director \mathbf{d}^1 , i.e. the direction of average orientation of particles, corresponds to the eigenvector of the eigenvalue λ^1	45

4.6	Biaxiality. $\mathbf{d}^1, \mathbf{d}^2, \mathbf{d}^3$ are the eigenvectors of the 2^{nd} order alignment tensor.	46
4.7	The position of the unit vectors—fibres— $x'_1 \dots x'_l$ relative to structural X, Y, Z and material meso-symmetry $\mathbf{d}^1, \mathbf{d}^2, \mathbf{d}^3$ coordinates.	47
4.8	Transformation of a fibre from local to structural coordinates. $Y_{x'_i x'_i}^{(fid)}$ is the Young's modulus of a fibre along the longest axis in local coordinates. $Y^{(m)}$ is the Young's modulus of the matrix.	48
4.9	Definition of the inclination angle θ and in-plane angle ϕ	48
4.10	The mean-field homogenisations.	50
4.11	The transformation between a rectangular and a spherical volume element.	53
4.12	Scatter plots of fibre orientations with the triplets of the eigenvectors; \mathbf{d}^1 -solid red line, \mathbf{d}^2 -dashed green line, \mathbf{d}^3 -dot-dashed blue line. \mathbf{d}^1 is the director corresponding to according-to-amount-largest eigenvalue. In (a) the radius represents the inclination angle θ and in-plane angle ϕ is on circumference. Z-axis corresponds to the direction of the tensile stress in a slab, Fig. 3.1.	54
4.13	The isolines of the measured fibre orientation distributions and the ODFs of fibres approximated using the 2^{nd} order alignment tensor.	55
4.14	SFRC member with a preferred orientation of fibres represented by the triplets of the eigenvectors in each spatial (meso-volume) finite element.	56
A.3.1	Variations in bivariate densities of the inclination angle θ and in-plane angle ϕ measured by μ CT between the side ("Cylinder *.A") and centre ("Cylinder *.B"), and along the height of the whole cylinder samples.	79
A.3.2	Scatter plots of fibre orientation variations measured by μ CT between the side ("Cylinder *.A") and centre ("Cylinder *.B"), and along the height of the whole cylinder samples. In (a) the radius represents the inclination angle θ and in-plane angle ϕ is on circumference. Z-axis corresponds to the direction of the tensile stress in a slab, Fig. 2.4.	80
A.3.3	Variations in bivariate densities of the inclination angle θ and in-plane angle ϕ measured by μ CT between the side ("Cylinder *.A") and centre ("Cylinder *.B") cylinder samples.	81

A.3.4	Scatter plots of fibre orientation variations measured by μ CT between the side (Cylinder *.A) and centre ("Cylinder *.B") cylinder samples. In (a) the radius represents the inclination angle θ and in-plane angle ϕ is on circumference. Z-axis corresponds to the direction of the tensile stress in a slab, Fig. 2.4.	82
A.4.1	Fibre orientation distributions with the triplets of the eigenvectors $\mathbf{d}^1, \mathbf{d}^2, \mathbf{d}^3$ for the height of the whole cylinder samples 1A and 1B. \mathbf{d}^1 -solid red line, \mathbf{d}^2 -dashed green line, \mathbf{d}^3 -dot-dashed blue line. \mathbf{d}^1 is the director corresponding to according-to-amount-largest eigenvalue. In (a) the radius represents the inclination angle θ and in-plane angle ϕ is on circumference. Z-axis corresponds to the direction of the tensile stress in a slab, Fig. 2.4.	84
A.4.2	Fibre orientation distributions with the triplets of the eigenvectors $\mathbf{d}^1, \mathbf{d}^2, \mathbf{d}^3$ for the height of the whole cylinder samples 4A and 4B. \mathbf{d}^1 -solid red line, \mathbf{d}^2 -dashed green line, \mathbf{d}^3 -dot-dashed blue line. \mathbf{d}^1 is the director corresponding to according-to-amount-largest eigenvalue. In (a) the radius represents the inclination angle θ and in-plane angle ϕ is on circumference. Z-axis corresponds to the direction of the tensile stress in a slab, Fig. 2.4.	85
A.4.3	Fibre orientation distributions with the triplets of the eigenvectors $\mathbf{d}^1, \mathbf{d}^2, \mathbf{d}^3$ for the middle parts of the cylinder samples. \mathbf{d}^1 -solid red line, \mathbf{d}^2 -dashed green line, \mathbf{d}^3 -dot-dashed blue line. \mathbf{d}^1 is the director corresponding to according-to-amount-largest eigenvalue. In (a) the radius represents the inclination angle θ and in-plane angle ϕ is on circumference. Z-axis corresponds to the direction of the tensile stress in a slab, Fig. 2.4.	86
A.5.1	The top parts of the cylinder samples. The isolines of the measured fibre orientation distributions and the ODFs of fibres approximated using the 2^{nd} order alignment tensor.	87
A.5.2	The bottom parts of the cylinder samples. The isolines of the measured fibre orientation distributions and the ODFs of fibres approximated using the 2^{nd} order alignment tensor.	88
A.5.3	The middle parts of the cylinder samples 1A–3B. The isolines of the measured fibre orientation distributions and the ODFs of fibres approximated using the 2^{nd} order alignment tensor.	89

A.5.4	The middle parts of the cylinder samples 4A–5B. The isolines of the measured fibre orientation distributions and the ODFs of fibres approximated using the 2 nd order alignment tensor. . . .	90
A.5.5	The middle parts of the cylinder samples 6A–6B. The isolines of the measured fibre orientation distributions and the ODFs of fibres approximated using the 2 nd order alignment tensor. . . .	91

List of Tables

3.1	Results of the two-sample bootstrap Kolmogorov-Smirnov test (function <code>ks.boot</code> from [2]) applied on the density distribution of the inclination angle θ in the slab 1. Reduced cuboid refer to the cuboid, where only every fourth slice surface is taken into account.	31
4.1	The scalar-order parameter S and triplet of the eigenvectors from the 2^{nd} order alignment tensor in spherical coordinates. $S = 1$ corresponds to the transversely isotropic material symmetry, $S = 0$ to isotropy and $S = -\frac{1}{2}$ describes the plane isotropic case. The biaxiality b_S shows the non-symmetry of the distribution with respect to \mathbf{d}^1	55
A.2.1	Results of the two-sample bootstrap Kolmogorov-Smirnov test (function <code>ks.boot</code> from [2]) applied on the density distribution of the inclination angle θ in the slab 2. Reduced cuboid refer to the cuboid, where only every fourth slice surface is taken into account.	77
A.2.2	Results of the two-sample bootstrap Kolmogorov-Smirnov test (function <code>ks.boot</code> from [2]) applied on the density distribution of the inclination angle θ in the slab 3. Reduced cuboid refer to the cuboid, where only every fourth slice surface is taken into account.	77
A.2.3	Results of the two-sample bootstrap Kolmogorov-Smirnov test (function <code>ks.boot</code> from [2]) applied on the density distribution of the inclination angle θ in the slab 4. Reduced cuboid refer to the cuboid, where only every fourth slice surface is taken into account.	77

A.2.4	Results of the two-sample bootstrap Kolmogorov-Smirnov test (function <code>ks.boot</code> from [2]) applied on the density distribution of the inclination angle θ in the slab 5. Reduced cuboid refer to the cuboid, where only every fourth slice surface is taken into account.	77
A.2.5	Results of the two-sample bootstrap Kolmogorov-Smirnov test (function <code>ks.boot</code> from [2]) applied on the density distribution of the inclination angle θ in the slab 6. Reduced cuboid refer to the cuboid, where only every fourth slice surface is taken into account.	78
A.4.1	Fibre orientation distribution characteristics for the top parts of the cylinder samples.	83
A.4.2	Fibre orientation distribution characteristics for the middle parts of the cylinder samples.	83
A.4.3	Fibre orientation distribution characteristics for the bottom parts of the cylinders.	83

Notations and definitions

Vectors and tensors are either denoted by bold letters or using index-notation for components with respect to an arbitrary fixed basis, for shortness the basis vectors will be omitted from the equations. Explicit calculations are performed in Cartesian coordinates. In index-notations, the Einstein summation convention is used.

A vector (bold small letters):

$$\mathbf{v} = v_i \mathbf{g}_i ,$$

A 2^{nd} order tensor (bold capital letters):

$$\mathbf{A} = A_{ij} \mathbf{g}_i \otimes \mathbf{g}_j .$$

A 4^{th} order tensor:

$$\langle 4 \rangle \mathbf{D} = D_{ijkl} \mathbf{g}_i \otimes \mathbf{g}_j \otimes \mathbf{g}_k \otimes \mathbf{g}_l .$$

An l -order tensor:

$$\langle l \rangle \mathbf{A} = A_{\mu_1 \dots \mu_l} \mathbf{g}_{\mu_1} \otimes \dots \otimes \mathbf{g}_{\mu_l} .$$

The 2^{nd} - and 4^{th} order identity tensors, respectively:

$$\mathbf{I} = \mathbf{g}_i \otimes \mathbf{g}_i , \quad \langle 4 \rangle \mathbf{I} = \mathbf{g}_i \otimes \mathbf{g}_j \otimes \mathbf{g}_k \otimes \mathbf{g}_l .$$

An outer product of two vectors (forming a second order tensor):

$$\mathbf{v} \otimes \mathbf{n} = v_i \mathbf{g}_i \otimes n_j \mathbf{g}_j .$$

An l -order symmetric irreducible (traceless) part of an l -order symmetric tensor formed by the l -order outer products of a vector \mathbf{n} with itself:

$$\underbrace{\mathbf{n} \otimes \dots \otimes \mathbf{n}}_{l\text{-times}} , \quad \overbrace{n_{\mu_1} \otimes \dots \otimes n_{\mu_l}} .$$

An inner product (also called scalar- or dot-product) of two second-order tensors:

$$\begin{aligned} \mathbf{A}\mathbf{B} &= \mathbf{A} \cdot \mathbf{B} = A_{ik}\mathbf{g}_i \otimes \mathbf{g}_k \cdot B_{kj}\mathbf{g}_k \otimes \mathbf{g}_j , \\ \text{if } \mathbf{B} &= \mathbf{A} , \text{ then } \mathbf{A}^2 = \mathbf{A} \cdot \mathbf{A} . \end{aligned}$$

A double inner product of two second-order tensors:

$$\mathbf{A} : \mathbf{B} = A_{ik}\mathbf{g}_i \otimes \mathbf{g}_k : B_{ki}\mathbf{g}_k \otimes \mathbf{g}_i .$$

An outer product of two second-order tensors:

$$\mathbf{A} \otimes \mathbf{B} = A_{ij}\mathbf{g}_i \otimes \mathbf{g}_j \otimes B_{kl}\mathbf{g}_k \otimes \mathbf{g}_l = C_{ijkl}\mathbf{g}_i \otimes \mathbf{g}_j \otimes \mathbf{g}_k \otimes \mathbf{g}_l .$$

A modified outer product of two second-order tensors:

$$\begin{aligned} \mathbf{A} \tilde{\otimes} \mathbf{B} &= A_{ij}\mathbf{g}_i \otimes \mathbf{g}_j \tilde{\otimes} B_{kl}\mathbf{g}_k \otimes \mathbf{g}_l = C_{iklj}\mathbf{g}_i \otimes \mathbf{g}_k \otimes \mathbf{g}_l \otimes \mathbf{g}_j , \\ \text{an example: } &A_{14}\mathbf{g}_1 \otimes \mathbf{g}_4 \tilde{\otimes} B_{23}\mathbf{g}_2 \otimes \mathbf{g}_3 = C_{1234}\mathbf{g}_1 \otimes \mathbf{g}_2 \otimes \mathbf{g}_3 \otimes \mathbf{g}_4 . \end{aligned}$$

Kelvin-Mandel variant of the Voigt notation preserving the tensor properties, especially regarding coordinate transformations [3]:

$$C_{\alpha\beta}^{\text{K-M}} = \begin{pmatrix} C_{1111} & C_{1122} & C_{1133} & \sqrt{2}C_{1123} & \sqrt{2}C_{1131} & \sqrt{2}C_{1112} \\ C_{1122} & C_{2222} & C_{2233} & \sqrt{2}C_{2223} & \sqrt{2}C_{2231} & \sqrt{2}C_{2212} \\ C_{1133} & C_{2233} & C_{3333} & \sqrt{2}C_{3323} & \sqrt{2}C_{3331} & \sqrt{2}C_{3312} \\ \sqrt{2}C_{1123} & \sqrt{2}C_{2223} & \sqrt{2}C_{3323} & 2C_{2323} & 2C_{2331} & 2C_{2312} \\ \sqrt{2}C_{1131} & \sqrt{2}C_{2231} & \sqrt{2}C_{3331} & 2C_{2331} & 2C_{3131} & 2C_{3112} \\ \sqrt{2}C_{1112} & \sqrt{2}C_{2212} & \sqrt{2}C_{3312} & 2C_{2312} & 2C_{3112} & 2C_{1212} \end{pmatrix}$$

$\alpha, \beta = 1, \dots, 6 .$

Some notations of continuum mechanics [4, 5]:

\mathbf{Lin} – a set of all linear mappings of a three-dimensional vector space \mathbb{R}^3 over real numbers into itself.

$\mathbf{Orth} = \{\mathbf{Q} \in \mathbf{Lin} : \mathbf{Q} = \mathbf{Q}^{-T}\}$ – the symmetry group of orthogonal transformations, where \mathbf{Q} is an orthogonal transformation matrix (rotations).

$W = W(\mathbf{F})$ – strain-energy density function.

\mathbf{X}, X_K – coordinates associated with the undeformed state; defined as *material* or *Lagrangian coordinates*. The undeformed state is chosen as a reference configuration.

\mathbf{x} , x_k – coordinates associated with the deformed state; defined as *spatial* or *Eulerian coordinates*.

$$\mathbf{F} = \frac{\partial \mathbf{x}}{\partial \mathbf{X}}, F_{kK} = \frac{\partial x_k}{\partial X_K} = x_{k,K} - \text{deformation gradient.}$$

$$\mathbf{C} = \mathbf{F}^T \cdot \mathbf{F} = \mathbf{C}^T, C_{KL} = \sum_k \frac{\partial x_k}{\partial X_K} \frac{\partial x_k}{\partial X_L} = x_{k,K} x_{k,L} - \text{Green deformation tensor.}$$

$\mathbf{E} = \frac{1}{2}(\mathbf{C} - \mathbf{I}) = \mathbf{E}^T = \frac{1}{2}(\nabla_{\mathbf{x}} \mathbf{U} + (\nabla_{\mathbf{x}} \mathbf{U})^T + (\nabla_{\mathbf{x}} \mathbf{U})^T \cdot \nabla_{\mathbf{x}} \mathbf{U}) = \frac{1}{2}(U_{K,L} + U_{L,K} + U_{M,K} U_{M,L}) - \text{Lagrangian strain tensor, where } U_{K,L}, U_{L,K}, U_{M,K}, U_{M,L} \text{ are displacement gradients. The term } U_{M,K} U_{M,L} \text{ refers to geometrical non-linearity. If } U_{M,K} U_{M,L} \ll 1, \text{ then:}$

$$\mathbf{E} \approx \boldsymbol{\varepsilon} = \boldsymbol{\varepsilon}^T = \frac{1}{2}(\nabla_{\mathbf{x}} \mathbf{u} + (\nabla_{\mathbf{x}} \mathbf{u})^T),$$

where $\boldsymbol{\varepsilon}$ is an infinitesimal strain tensor and \mathbf{x} represents undeformed position. A benefit of using *Lagrangian* strain tensor is that *Lagrange strain*, ε_L , can be measured based on experimental data, i.e.

$$\varepsilon_L = \frac{l^2 - l_0^2}{2l_0^2} = \frac{1}{2}(\beta^2 - 1),$$

where l_0, l are sample lengths in the beginning and end of a test, respectively and $\beta = \frac{l}{l_0}$ is a stretch ratio.

An infinitesimal strain—*engineering strain*, ε_e —may be experimentally defined as following:

$$\varepsilon_e = \frac{l - l_0}{l_0} = (\beta - 1).$$

$\mathbf{S} = 2 \frac{\partial W}{\partial \mathbf{C}} = \frac{\partial W}{\partial \mathbf{E}}$ – second *Piola-Kirchhoff pseudo-stress* tensor, expresses the stress with respect to the original (undeformed) surface area. Second Piola-Kirchhoff pseudo-stress tensor presents the stress at the material point X .

(c), (m), (f), (s) – refer to the composite, matrix, fibres, steel, respectively.

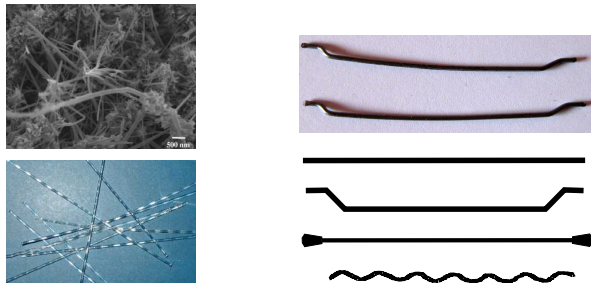
$^{ij}, i, j, i, j = 1, 2, 3$ – upper indices refer to material symmetry axes.

(f_{ms}), (f_{str}) – refer to orientation-weighted fibres in material meso-symmetry and structural coordinates, respectively.

S – refers to a symmetric part of a tensor (minor symmetry within last 2 indices).

1. Introduction

In the last decades the development of composites is connected with the need to improve the efficiency and economy of materials. A possibility to increase the strength of the base material or matrix is the addition of short fibres. Concrete-matrix composites are an example of short fibre-reinforced materials. They usually consist of a cement-based matrix and different types of short fibres: glass [6], polypropylene [7], carbon [8], and steel [9], Fig. 1.1. The short steel fibres are made of cold-drawn steel, which has a high strength, but insignificant deformation capacity compared to the ductility of common hot-rolled construction steels. The shapes of steel fibres depend on manufacturers as shown in Fig. 1.1(b).



(a) Upper: carbon nanofibres [8].
Lower: polypropylene fibres.

(b) Steel fibres with varying geometry.

Figure 1.1. Short fibres used for the reinforcement of concrete matrix.

The motivation to study concrete composites comes from the demand for using them in load-bearing structures to reduce the construction time and improve quality of structures. The addition of fibres may help to decrease brittle failure characteristics of concrete. The major role of fibres is to carry tensile stresses, while the concrete matrix carries compression as well as distributes and transfers the internal tensile forces to the fibres.

The present research concentrates on the study of the properties and the use of concrete reinforced by short hooked-end steel fibres (steel fibre reinforced concrete, SFRC). In contrast to concrete reinforced with steel bars, short steel fibres are added to the concrete mass at the mixing stage, Fig. 1.2.

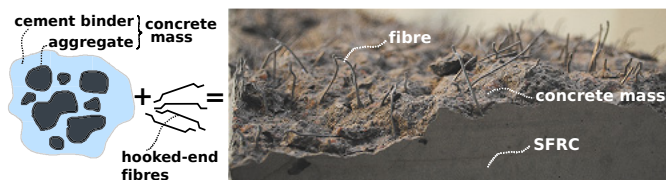


Figure 1.2. Cross-section of a cast SFRC structure. Concrete reinforced by short hooked-end steel fibres, SFRC.

Although the properties of SFRC have not been thoroughly explored, it is widely used in the construction industry and even for providing the load-bearing capacity of structures, Fig. 1.3. In recent years many scientists have



(a) Cast SFRC floor-slabs in Rocca Tower, Tallinn, Estonia.
 (b) Cast SFRC floor-slabs in the office building on Kotkapoja street, Tallinn, Estonia.

Figure 1.3. Buildings where SFRC was used for load-bearing structures.

devoted their research to the study of steel fibre reinforced concrete. For example, in the references [9, 10] the authors summarized both theoretical and experimental knowledges developed during the last 20-30 years of research. The studies such as [11, 12] were focused on constitutive mappings. In some recent works [13, 14, 15, 16, 17, 18, 16, 19] the authors utilised several advanced methods and approaches, such as computer-tomography, electrical and magnetic surveys, and image analysis, to investigate the mechanical properties of SFRC. The bearing capacity of SFRC largely depends on the orientation distribution of fibres. Fig. 1.4 demonstrates a basic difference between concrete beams reinforced with steel bars and short steel fibres. In a conventionally

reinforced concrete beam, the predicted tension coincides with the actual reinforcement. From Fig. 1.4, it is possible to conclude that the determination and further the quantification of fibre orientations play an important role in the specification of the bearing capacity of SFRC.

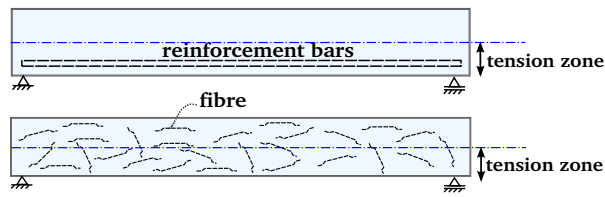


Figure 1.4. The comparison between a reinforced concrete and a SFRC beam. In the SFRC beam the orientation distribution of fibres is not specified.

1.1 Unknowns and open questions with SFRC

The development of any composite system requires to study its deformation and fracture mechanics. The adding of short steel fibres to the matrix leads to an anisotropic behaviour, i.e. direction dependent properties. SFRC exhibits anisotropic properties in accordance with the orientation distribution of fibres. When the alignment of fibres coincides with a principal stress in a structure, the contribution of fibres to the material strength is more pronounced than otherwise. Many empirical measuring techniques enable us to determine the orientation of short steel fibres [17, 20, 21]. Though, the main limitation of these methods is that they may define only the tendencies such as a measured average orientation of fibres and some degree of alignment [20, 21] instead of the attempt to evaluate the orientation of each fibre. In the earlier studies the casting of specimens is usually carried out under well defined and controlled laboratory conditions. These conditions may clearly differ from those at a construction site, where the casting depends on the technological process and is typically site-specific.

The behaviour of any material is determined by its properties, which are considered by constitutive equation (material model). This equation establishes the linkage between stresses and deformations. As the properties of the studied composite depend on the orientation of short steel fibres, a reliable material model for SFRC shall include the quantities, which give a representative description of fibre orientations.

The material models available for composites reinforced by short fibres usually either consider the orientation of fibres utilizing only a single one-dimensional

case with aligned fibres [22, 23] or assume a mean orientation with respect to a predefined axis and use one orientation angle as a parameter [11, 12]. One approach is the orientation number (ON), which is defined as an average projected length of fibres in a cross-section onto the normal of the cross-section divided by the fibre length [12]. Another approach is the orientation profile (OP) [11], which extends the concept of the orientation number counting the amount of fibres (out of the total number of fibres given) within different inclination intervals assuming a pre-defined statistical distribution.

An alternative would be the use of full orientation information of fibres and tensor quantities. In spherical coordinates the position of a point is specified by three numbers: radial distance, inclination angle θ , azimuth (in-plane) angle ϕ . For the description of the orientation of a fibre two angles are necessary and the radius is not needed, Fig. 1.5.

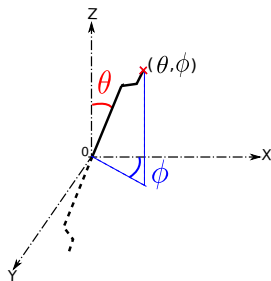


Figure 1.5. Representation of a fibre in spherical coordinate system.

Recently, a plastic approach (based on the formation of plastic hinges) has found a wide application in the design of load-bearing structures made of SFRC [24, 25, 26, 27]. This approach assumes a plastic dependence between the stress and strain and also redistribution of stresses in statically indeterminate structures [28]. Thereby, in a bended conventionally reinforced concrete member, the area of large local plastic deformations, called a plastic hinge, is assumed to be developed. This area includes the compressed concrete zone and tensioned steel bars. However, the behaviour of a bended SFRC member can be taken rather brittle than ductile, since the cracks in a tension zone are not gradually developing and, as a consequence, the failure may occur suddenly. In the case of SFRC, it is not possible to assume any yielding of short steel fibres since they are made of cold-drawn high-strength steel and their anchoring capacity is limited. These issues suggest to start the constitutive mappings for SFRC from the linear-elastic state, meaning that the cracking can be excluded from the material model.

The lack of an objective material model for SFRC, which includes the ori-

entation distribution of fibres required for predicting the bearing capacity of SFRC, suggests that a more fundamental, both theoretical and experimental, research is needed. In addition, the intention to use SFRC as a load-bearing component in concrete structures requires numerical simulations using the material models, which are independent of any reference frame.

The shortcomings of present theories for fibre reinforced materials and their limitations for the design of load-bearing structures made of SFRC are highlighted and presented in [Publication I](#).

1.2 Research goals and implementations

The mechanical properties of SFRC are directly dependent on the orientation distribution of short steel fibres. Only by knowing fibre orientations it is possible to determine the bearing capacity of this composite. The ability to measure the orientation of fibres may also provide a ground to monitor, track and influence on the orientation during the production or cast process. Thus, the main goals of this study can be classified as follows:

experimental: determination of fibre orientations in specimens

theoretical: development of an anisotropic linear-elastic material model, which includes the orientation distribution of fibres

The outcomes of the study can be used for developing the production process of SFRC structures, since the existing principles of casting concrete structures are not originally designed for SFRC and new technological solutions optimising the fibre orientations in the composite are needed.

In developing the methodology for measuring fibre orientations in SFRC products two methods are under elaboration: slicing and X-ray micro-tomography.

For both methods the parts extracted from the real-size structures were employed as specimens. The target of the slicing method developed is the intention to combine two approaches, i.e. the photometric image analysis and DC-conductivity measurements by a special robot. As an output, it is expected to obtain the full orientation information of each measured fibre in spherical coordinates. X-ray micro tomography (μ CT) is an advanced method for measuring the orientation distribution of fibres from hardened concrete samples. With this method, it is planned to obtain a voxel image of fibres directly in 3D and, later on, the orientation of each individual fibre can be calculated based on a skeletonized (centre line) representation of 3D image received.

The possible applicability of the developed methods for measuring fibre orientations, their precision, and feasibility are highlighted in [Publication IV](#), [Publication V](#).

The presence of short fibres in SFRC and the relevance of their orientation to the bearing capacity of the composite makes it necessary to consider these factors in governing equations. Besides, the brittle behaviour of the concrete matrix, the restricted anchoring of short steel fibres and small range of plastic deformations of high strength steel used for fibres justify the assumption of linear-elastic dependence between stress and deformation. Regarding to this, *the research includes the formulation of the orthotropic linear-elastic constitutive relation for one representative volume element of steel fibre reinforced concrete taking into account the orientation distribution of fibres.*

The approach is based on the use of the orientation distribution function and the alignment tensors [29, 30, 31]. These quantities have been successfully employed in e.g. liquid crystals (LCs) [29, 30], short fibre polymer composites [31], and penny shaped micro-cracks in brittle materials [32], where the orientation distribution of rod-like particles is relevant. The approach rests on the concepts of mesoscopic continuum theory, which is between a microscopic description, which uses the statistical methods, and macroscopic description, which usually does not take into account any micro-structure. Mesoscopic continuum theory introduces new variables as, for example, the mesoscopic distribution function, which in our case is a statistical orientation distribution function. It was developed about 50 years ago for LCs (rod-like particles) [33, 34, 35]. The orientation distribution function (ODF) defines a probability of finding a rod-like particle between the given angles on a sphere. Each point of this sphere is associated with the direction of a rod-like particle (LC molecule, fibre) represented by a unit vector. Thereby, all possible directions of a unit vector form a unit sphere (radius $r = 1$) [30]. Here, it is useful to introduce the l -order orientation tensor (OT), which is symmetric and can be composed by dyadic products of a unit vector with itself, then integrating the result with the ODF over the whole unit sphere [31]. The irreducible—symmetric traceless—part of the l -order OT, called the l -order alignment tensor (AT) [29, 30, 36], can recover the ODF. The orientation distribution function defined on a unit sphere can be expanded into the series of main spherical harmonics forming a complete orthonormal basis. The l -order symmetric tensorial product of a unit vector from which the trace is removed gives an l -order symmetric irreducible tensor, which is a spherical harmonic function [30]. The latter allows to decompose the ODF in a series by basis

formed by symmetric irreducible tensors and the ATs are acting as the expansion coefficients. This implies that if the expansion coefficients—ATs—in a complete orthonormal basis are known the original function—ODF—can also be considered as known [37].

The clear advantage of using the tools of mesoscopic continuum theory in the present research is achieved by the potential to describe the orientation state of short fibres in space employing the tensorial quantities: orientation and alignment tensors. The latter are able to include the complete data of fibre orientations (two angles in spherical coordinates) needed for specifying the position of a point in space. Moreover, the described mesoscopic orientation characteristics can be used in the material model for SFRC.

The main tasks that will be solved during the research are presented in Fig. 1.6. From the figure we may conclude that the concept of the whole work is the consolidation of theoretical and experimental branches. This is needed for enhancing the design and manufacturing in order to obtain the most favourable orientation of fibres in a structure.

The constitutive modelling of anisotropic material properties of SFRC employing the concepts of mesoscopic continuum theory is highlighted in [Publication VI](#).

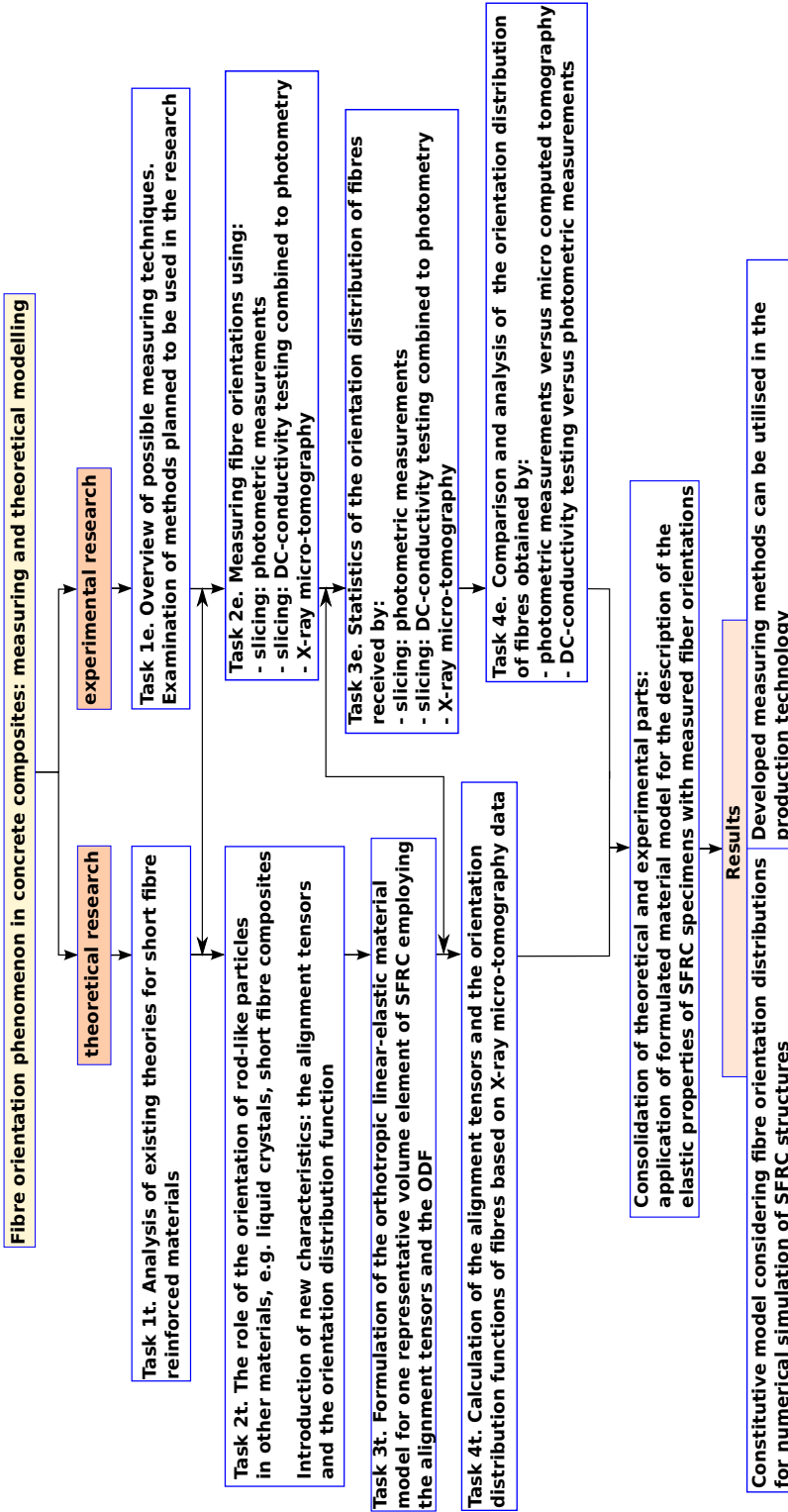


Figure 1.6. Graphical representation of the basic objectives during the research.

2. Methodology for measuring fibre orientations

The bearing capacity of SFRC has an anisotropic nature, and the level of anisotropy originates primarily from the orientation state of fibres. Thus, an experimental problem is the determination of the orientation distribution of fibres. In this Chapter, an overview of methods for measuring fibre orientations in SFRC precedes a detailed description of the methods elaborated and realized in the research work.

The measuring techniques developed and implemented in the research are highlighted in [Publication IV](#) and [Publication V](#).

2.1 Overview of measuring techniques

In recent years, various techniques have been utilised to investigate the orientation of short steel fibres in hardened concrete. These methods include photometric analysis [11, 12, 14, 15, 38, 39], X-ray computed tomography [16, 40, 41, 42] or they are based on different physical phenomena such as electrical conductivity and magnetism [20, 21, 43, 44].

Slicing with photometric analysis

The idea to utilize the photos of cut specimens—slices—to specify fibre orientations in fibre reinforced composites has already been widely used, e.g. by P. Stroeven and J.Hu, L.Ferrara *et al.*, P. Purnell *et al.* [14, 18, 45], by C.Redon *et al.* [17], who used a Fourier transform and by C. Redon *et al.*, P.Stroeven [43, 46], who used image analysis on 2D X-ray transmission images. Fourier image transform is an automatic method to assess fibre orientations. It involves the application of the Fourier transform depending on the orientation of a mask on a grey-level image and, further, the detection of the portions of fibres oriented into the defined direction. 2D X-ray images may be employed to trace manually the fibres on transparent films representing them by a num-

ber of distinguishable lines. Therein the precision of outcomes depends on the resolution of images, as the estimation of fibre orientations is based on the geometry of cut fibres. The shape detection of cut fibres may be performed using an image analysis software. Employing this method it is possible to define the orientation of a fibre in spherical coordinates, by the inclination θ and in-plane ϕ angles, Fig. 1.5. However, the in-plane angle can be measured only within the interval from $[0^\circ, 180^\circ]$ instead of the $[0^\circ, 360^\circ]$ and this leads to an ambiguity in the direction of a fibre, Fig. 2.1.

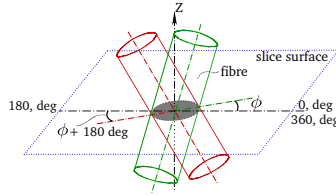


Figure 2.1. Ambiguity in the direction of a fibre in case of photometric analysis.

This is not a problem of the image analysis software employed, but fundamental to the analysis of 2D images, which can only contain limited information.

X-ray computed tomography

X-ray computed tomography (CT) has emerged as a powerful technique for non-destructive 3D visualization of the micro-structural features of objects [13, 47, 48, 49]. The method has also been used to study fibre and steel fibre reinforced concrete [16, 42, 50, 51]. The X-ray micro-tomography (μ CT) basically works on the same principle as conventional CT, except that in μ CT the sample is rotated instead of the X-ray source and detector. The main benefit of μ CT method is that it allows to determine the orientation of individual fibres in a sample based on their spatial (3D) representation. The major steps of μ CT are:

- scanning of composite sample;
- segmentation into constituent material phases and visualization as 3D image;
- application of skeletonization (centre line) algorithms;
- analysis of skeletonized objects, e.g fibres;
- determination of the inclination θ and in-plane ϕ angles of each individual fibre.

Indirect methods for conductive steel fibre reinforced composites

Indirect methods mainly rely on the electro-magnetic properties of steel fibres. Two recently used methods are a magnetic one, and another is based on the alternating current impedance. An advantage of these methods is their non-destructive nature. A drawback is the ability to assess only general tendencies, such as the average orientation of fibres and some order of their alignment, instead of the evaluation of the orientation of a single fibre.

A magnetic method

A magnetic method is one of those developed within last 3 years. It is a non-destructive method, based on monitoring the specimen surface and detecting or measuring the variation of the inductance of a probe [20]. The main idea of the method is that the presence of steel fibres within a specimen can modify the flux linked by the winding of a probe resulting in the variation of impedance. A magnetic permeability of cement-based matrix is much lower than that of fibres. Thereby, the macroscopic magnetic properties of the matrix material and the effective magnetic permeability dyad of the composite can be defined. The effective magnetic permeability depends on the volume fraction of fibres, on their orientation and aspect ratio (ratio of length to diameter), but it does not depend on their size. Therefore, the measuring of a parameter influenced by the effective permeability of SFRC element may allow to assess both the concentration and orientation of steel fibres.

Alternating Current Impedance Spectroscopy

Alternating Current Impedance Spectroscopy (AC-IS) is an electrical characterization method, which allows to study the various features of micro-structural materials [21]. AC-IS can also be utilised to obtain fibre dispersion parameters of conductive fibre reinforced composites owing to its unique dual-arc behaviour. The latter means that, due to the existence of a small portion of conductive fibres in a composite of finite matrix conductivity, one matrix impedance arc is divided into two separate low and high frequency arcs in the complex impedance plane. This effect is more pronounced when the fibres are highly conductive compared to the matrix material. The dual-arc mode is caused by the frequency dependent behaviour of conductive fibres, which are insulating under the low frequencies (Hz), but are conductive under the high frequencies (MHz). Thus, the idea of applying the AC-IS method on SFRC includes the impact of an alternating voltage on specimens (concrete and SFRC) and the measurement of a current responses. For this purpose,

the electrodes are positioned on the specimens and further the matrix and composite resistances are measured. Later on, it is possible to calculate the conductivities of the matrix and composite. The measurements result in normalized conductivity profiles of specimens.

2.2 Selection of measuring methods

Within the research work, slicing and X-ray micro-tomography methods are chosen as basic approaches for measuring fibre orientations in SFRC samples. Such selection is made by the following criteria:

The slicing method does not require any special or expensive devices: which makes it attractive for industrial applications too. X-ray micro-tomography (μ CT) is based on expensive devices operated by highly educated personal. In spite of this, its accuracy and clarity are greater than other methods for measuring of fibre orientations: thus, it sets a baseline for the calibration of the methods. μ CT method is also interesting as the integration of some, perhaps not so sophisticated, CT systems into the manufacturing process of SFRC may be feasible in the future.

2.3 Slicing method as a combination of DC-conductivity testing with photometry

Compared to those earlier studies, the slicing method developed in this research is based on the structural parts extracted from the full-size members (floor-slabs) and the use of multiple slices close to each other, which are analysed to improve the statistics, in contrast to the single-picture approach that is found in the literature [15]. In addition, the experimental full-size members are prepared not in controlled laboratory conditions, but following the site-specific casting. The slices are analysed utilizing approaches that are joined together: the coordinates received in the image analysis are employed as an input for a special robot measuring DC (direct current) conductivity.

The first phase of the slicing method presented includes the extraction of sample cuboids from the full-size floor-slabs, cutting them into the slices and taking the photos of slice surfaces. In the photos the fibres cut are visible as ellipses and circles. The image processing and analysis including the detection of the shapes of cut fibres are performed using the public domain software ImageJ [52]. Identification of the geometry of cut fibres makes it possible to measure the inclination θ and in-plane ϕ angles. As it was mentioned above,

the measurement of the in-plane angle ϕ by photometry is possible within the range of $[0^\circ, 180^\circ]$, which results in the ambiguity of the direction of a fibre. The measured orientation distribution of fibres by photometry needs to be adjusted/checked by some additional approaches in slicing. Therefore, the slicing with photometry is improved by a prototype of a special robot measuring DC-conductivity by scanning the slice surfaces and measuring the electrical conductivity between the cut ends of steel fibres. If the cross-sections of a cut fibre on the opposite slice surfaces belong to the same fibre, the current flows and the robot detects the electrical conductivity and saves the coordinates. The measurements by a robot are combined with photometric data and thus this approach is considered as an extension of slicing with photometry. The coordinates of cut fibres on both sides of a slice are known from the image analysis and one can use these as the input for a robot. The outcome received by combining two analysing approaches in slicing, i.e. photometry and DC-conductivity, improves the results of photometry. The main advantage by adding the DC-conductivity testing to the procedure is that it removes the ambiguity related to the in-plane ϕ angle.

2.3.1 Experimental set up

A horizontal structure was chosen to study the orientation distribution of fibres since the structure makes possible to observe both the compressive and tensile stresses as well as the features of fibre behaviour in the vicinity of the formwork and in the bulk. Thereby, six experimental full-size floor-slabs were cast in a factory using a bucket according to the scheme presented in Fig. 2.2(a). The concrete class was C30/37 and concrete was self-compacting, which means no vibration was needed. The fibres used had hooked-ends, the length of a fibre l_f was 50 mm and the diameter d_f was 1 mm, Fig. 2.2(b). The material for fibres was rod wire of types C4D or C7D steel according to standard EN 10016-2 and their amount per cubic meter of concrete was 80 kg, resulting in about 250 fibres per dm^3 .

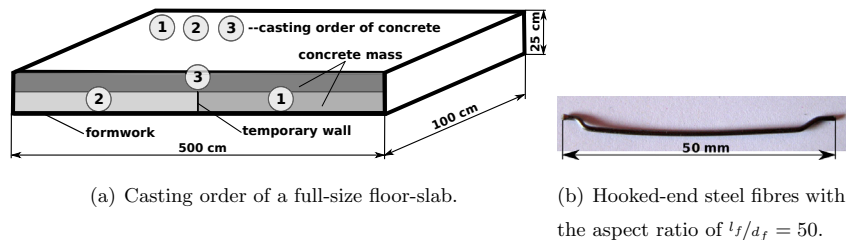


Figure 2.2. The casting order and the fibre types used.

The extraction of sample cuboids from the full-size floor-slabs has started on the 30th of September 2010 and was implemented in the Department of Civil and Structural Engineering in Aalto University (Finland). Before the extraction of cuboids, 28 days old slabs were tested using a three point bending test. During these tests three slabs have shown approximately the same capacity (slabs 1, 2, 3) and the capacity of the remaining three ones (slabs 4, 5, 6) was lower, Fig. 2.3. This behaviour could be explained either by different fibre orientations or by variations in matrix quality such as the existence of air pores. The tested slabs with sample cuboids are presented in Fig. 2.4.

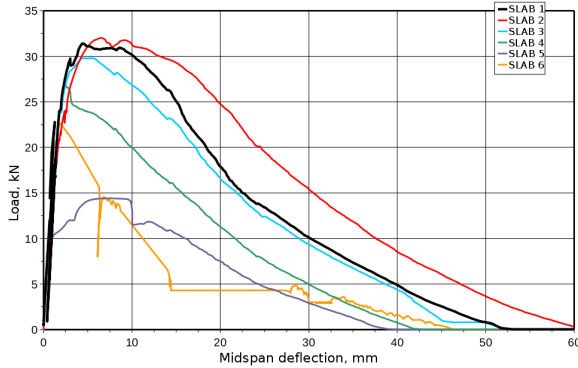


Figure 2.3. Load-deflection diagram of tested floor-slabs during the bending test.

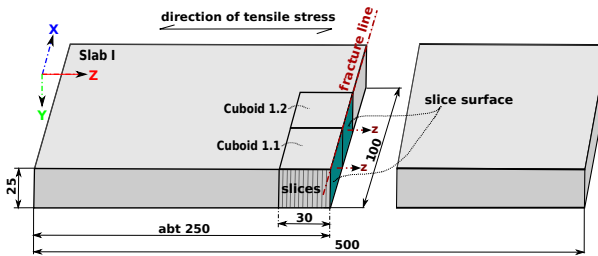


Figure 2.4. Representation of a floor-slab and sample cuboids. Dimensions in (cm).

The sample cuboids ($H \times W \times L : 25 \text{ cm} \times 30 \text{ cm} \times 30 \text{ cm}$) were extracted from the slabs using a diamond saw, Fig. 2.5(a). Each sample cuboid was numbered according to the number of a slab from which it was cut, Fig. 2.4. In addition, all cuboids were marked on a top by milled cross and on one edge by blue water-resistant colour, Fig. 2.5(b). Altogether twelve cuboids were taken. Six of them were sawn from the central part and the others were taken from the side of the slabs, Fig. 2.4. This was done to detect the influence of the formwork moulds on the arrangement of fibres in the matrix, i.e. the tendency of fibres to align themselves in the vicinity of a formwork. Onwards, the sample cuboids were cut into the slices. The cutting of slices has began on



(a) The process of cutting the sample cuboids using a diamond saw. (b) The marking of cuboids by a milled cross and water resistant blue colour.

Figure 2.5. The cutting and marking of sample cuboids.

the 8th of October 2010. The sample cuboids were transported to a company specializing in the cutting of hard stones. As the sample cuboids had the height of 25 cm, a special stationary diamond saw was needed, Fig. 2.6. Due to the cutting method, the material was lost in the range of 5 – 10 mm in each cut section.



(a) The disc of a saw with diamond in-cisors. (b) The measuring of a slice.

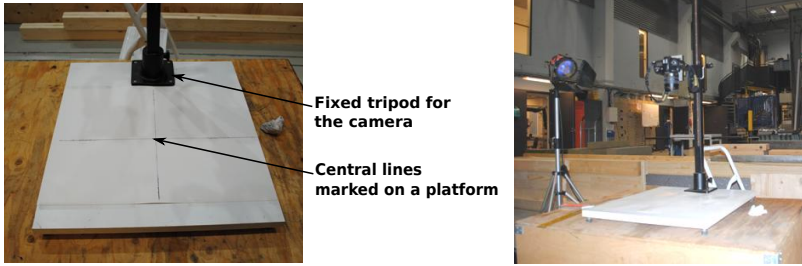
Figure 2.6. The diamond saw used.

It was planned to cut each sample cuboid into 15 slices with the thickness of 2 cm and, hence, to produce 180 slices. However, the cutting of the cuboids into the slices by a diamond saw has caused a considerable loss of the material and instead of the expected 15 slices there were only 11 or 12 slices. Consequently, approximately 60 mm of the material were lost during the cutting process if the number of slices was 12 and in the case with 11 slices the material lost was 80 mm. The numbers of slices received from the sample cuboids were:

- Slab 1: Cuboid 1 – 12 slices, Cuboid 2 – 12 slices;
- Slab 2: Cuboid 1 – 11 slices, Cuboid 2 – 11 slices;
- Slab 3: Cuboid 1 – 11 slices, Cuboid 2 – 11 slices;
- Slab 4: Cuboid 1 – 11 slices, Cuboid 2 – 12 slices;
- Slab 5: Cuboid 1 – 11 slices, Cuboid 2 – 11 slices;
- Slab 6: Cuboid 1 – 11 slices, Cuboid 2 – 11 slices.

2.3.2 Slicing with photometry

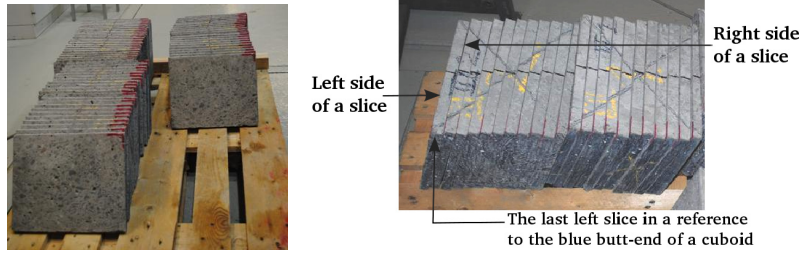
The process of photometry has began on the 25th of October 2010. When the sample cuboids had been cut into the slices the photos were taken from each slice surface. Fig. 2.7(a) represents a platform used for taking the pictures. A tripod for the photo-camera was fixed on the platform, Fig. 2.7(b). In order to place the slice surface to the centre of the platform, the central lines were marked as shown in Fig. 2.7(a). The central lines of the platform coincided



(a) The platform for taking a picture of slice surface. (b) The tripod fixed on a platform.

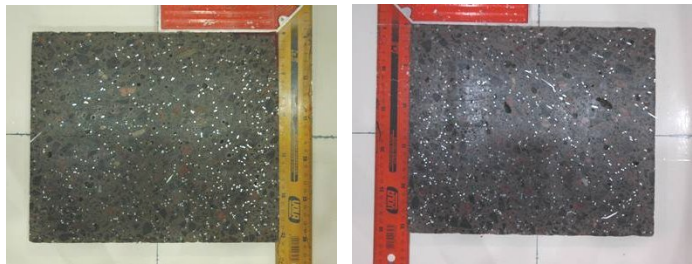
Figure 2.7. The tools used for photographing slice surfaces.

with the central lines of the camera lens. Middle points were marked on two edges of each slice, which further have been merged with the central lines on the platform. To avoid the loss of the correct position of a slice in a cuboid, a corner of each slice was denoted by the red colour. The marked red corner was on the left surface from the blue butt-end of a slice, Fig. 2.8(a). Taking the photos of slice surfaces required a correct lighting. By wetting the slice surface the concrete matrix was made non-reflective and the steel fibres started to reflect the light like a mirror. However, if the slice surface became too wet, the concrete matrix started to reflect the light as well, and it was necessary to wait a moment till the concrete surface had dried a little and become opaque. Taking the photos of slice surfaces in a cuboid were started from the last left slice in a reference to the blue butt-end of a cuboid, Fig. 2.8(b). At first, the photos of the left surface of a slice were taken and then the photos of the right surface, Fig. 2.8(b). In photos, the indication of the left or right surface of a slice was made by the colour of a ruler. The left slice surface was identified by a yellow-red and the right one by a red ruler, Fig. 2.9. The graphical representation of a sample cuboid with slices is shown in Fig. 2.10.



(a) The marked red corners of slices. (b) The order of taking the photos of slice surfaces in a cuboid.

Figure 2.8. The positioning and marking of slices.



(a) The left surface of a slice and a yellow-red ruler. (b) The right surface of a slice and a red ruler.

Figure 2.9. The identification of the left or right surface of a slice by the colour of a ruler.

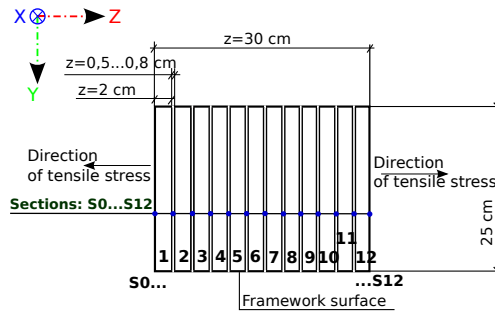


Figure 2.10. Representation of a sample cuboid with slices, see also Fig. 2.8(b).

The photos were saved in two formats at a time: RAW–nef and JPG–basic. The image processing and analysis was done on the RAW images because of their higher resolution and using the public domain software ImageJ [52]. A photo of a slice after its filtering with pseudo-flat-field filter [53] and cleaning in binary format is presented in Fig. 2.11. As the fibres are cylindrical, which is a degenerated cone, the intersection of a cone with a plane gives an ellipse as a closed curve. Hence, the bright inclusions in Fig. 2.11(a) are the cut cross-

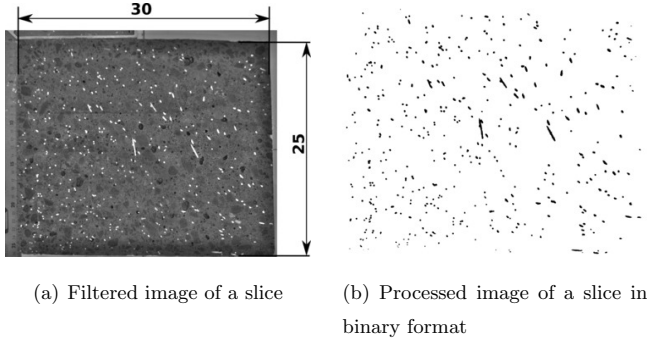


Figure 2.11. Image of a slice.

sections of fibres. The data obtained after the analysis of slice surface include: the coordinates X_i, Y_i determining the position of the centre of fitted ellipses from the origin, the major and minor axes of the ellipses and the in-plane ϕ angle, Figs. 2.12(a), 2.12(b). The shape of an ellipse can give an assessment of the inclination angle θ as the ratio of minor and major axis, Fig. 2.12(a),

$$\theta = \arccos \left(\frac{\text{Ellipse Minor axis}}{\text{Ellipse Major axis}} \right). \quad (2.1)$$

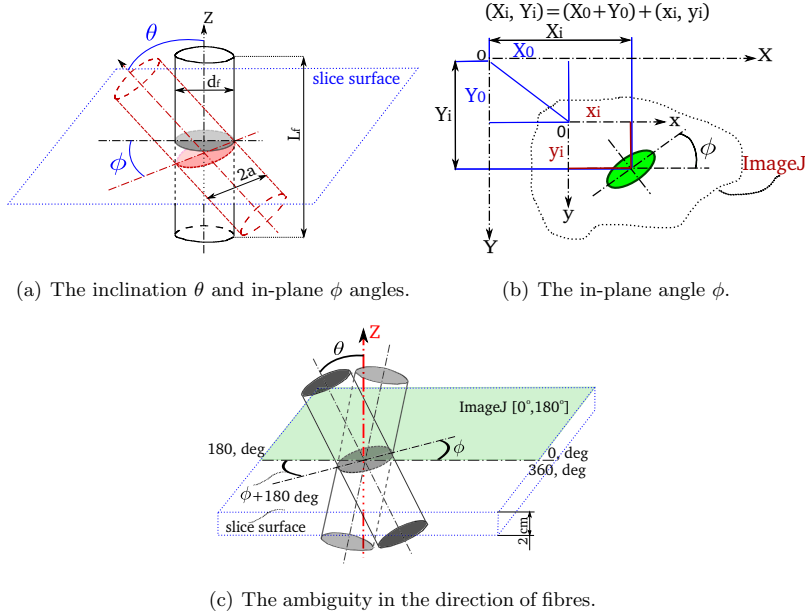


Figure 2.12. Definition of the orientation angles applying the image analysis.

If a fibre is aligned parallel with the normal Z of the slice surface, then the cross section of a cut fibre is a circle with a diameter d_f and the ratio

$$1 = \lim_{\theta \rightarrow 0} \cos(\theta) = \lim_{2a \rightarrow d_f} \frac{d_f}{2a}, \quad (2.2)$$

which implies, that the inclination angle θ is equal to 0° . On the contrary, if a fibre is perpendicular to the normal Z , then the ratio

$$0 = \lim_{\theta \rightarrow 90^\circ} \cos(\theta) \approx \lim_{2a \rightarrow L_f} \frac{d_f}{2a}, \quad (2.3)$$

what means, that the inclination angle θ is 90° . The in-plane angle ϕ is measured between the orientation of the major axis of an ellipse and the horizontal coordinate axis, Fig. 2.12(b).

As Fig. 2.12(c) illustrates, the in-plane angle determines the direction of a fibre. This direction can be counted from 0° up to 180° degrees, which leads to an ambiguity in the direction of a fibre. In more detail this ambiguity can be formulated as follows: if the direction of a fibre has the ϕ angle of 45° , this cannot be distinguished from the fibre at the ϕ angle of $45^\circ + 180^\circ$, since for both cases the shape of cut fibre on slice surface will be the same, Fig. 2.12(c).

2.3.3 Slicing with DC-conductivity joined with photometry

As it was noted in Section 2.3.2, the measurement of the in-plane angle ϕ by photometry is possible within the interval from $[0^\circ, 180^\circ]$ only. Thus, the measured orientation distribution of fibres needs to be checked by some additional approaches in slicing or by another measuring method. DC-conductivity testing was concluded to be an appropriate extension of slicing with photometry, as it can utilize the coordinates of cut fibres defined in the image analysis. Since the fibres are of steel, they have a good electrical conductivity. The robot scans the opposite surfaces of a slice and measures electrical conductivity between the endpoints of cut fibres. If the cut cross-sections of a fibre on the opposite slice surfaces belong to the same fibre, the current flows and the coordinates (in Cartesian system) are recorded to a '.txt' file. The next step is to process the coordinates measured by the robot to get the directions of cut fibres. This can be implemented by the subtraction of the coordinates on one slice surface from those on the opposite surface:

$$d = \begin{pmatrix} X \\ Y \\ 0 \end{pmatrix} - \begin{pmatrix} U \\ V \\ 20 \end{pmatrix}, \quad (2.4)$$

where 20 is a slice thickness in mm. The limit inclination angle measured by a robot depends on the thickness of a slice and the length of used fibres. For example, the 20 mm thick slice and 50 mm long fibres give the limit inclination angle of $\theta_c = \arccos\left(\frac{20 \text{ mm}}{50 \text{ mm}}\right) = 1.159 = 66.4^\circ$. The in-plane ϕ angle is measured in the interval $[0^\circ, 360^\circ]$, there is no ambiguity here.

The scanning robot was built in cooperation with the Centre of Biorobotics at Tallinn University of Technology (TUT). This robot has four linear axis and

two probes, Figs. 2.13, 2.14(b), 2.14(c). Each axis has a separate drive, so that the probes can be moved independently on a 2D plane: one probe on one side and the other on the opposite side of a slice, see Figs. 2.13, 2.14(a), 2.14(b).

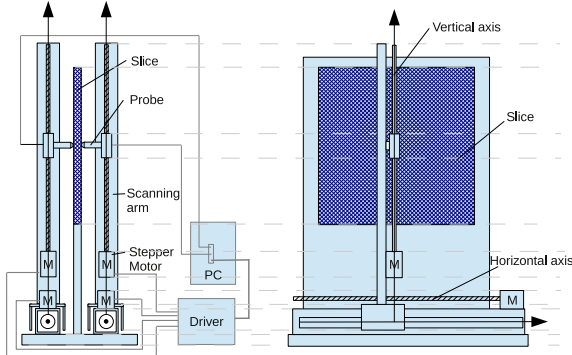
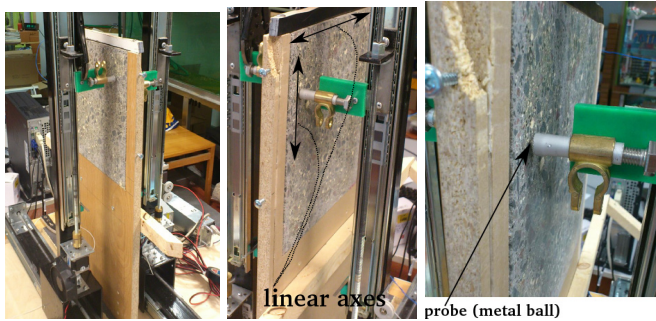


Figure 2.13. The scanning robot (side and front view).



(a) Scanning of one side of a slice.

(b) Scanning of the opposite side of a slice.

(c) A probe.

Figure 2.14. The scanning robot in use.

Each probe is made of a spring, tube and a steel ball, Fig. 2.14(c). The input data were the coordinates of the cross-sections of cut fibres on the both sides of a slice and the output data should be the coordinates of connected cross-sections. The Emc2 (Enhanced Machine controller) software [54] was selected to control the scanning robot. It is a free Linux program for computer control of different machines. The program was configured to control 4 linear axes at the speed of 10 mm per second. Two methods were considered for scanning the slice surface. One was to scan the whole surface area (step 0.9 mm), which would take about 5 years with the present prototype. The other method was to check only the coordinates of the cross-sections of cut fibres defined in image analysis. The second method was selected as it reduced the scanning time remarkably. The algorithm for the movement of axis was made using

the G-code (DIN 66025/ISO 6983), which is widely used in the automation telling the computerized machines where, how fast, and which path to move. The G-code algorithm included about 25000 different combinations consisting about 180 000 lines. Therefore, another simple program was written in the C-language. This program calculates the range, where the cross-section of a cut fibre may locate on the opposite slice surface and accordingly generates the G-code.

2.4 X-ray micro-tomography method (μ CT)

The cylinder samples (sufficiently large in size) extracted from the same full-size floor-slabs as the sliced cuboids were scanned using μ CT equipment. With this method, the fibres in a samples were represented directly in 3D and, further, the application of 3D skeleton (centre line) processing algorithm made possible to specify the orientation of each individual fibre.

2.4.1 Procedure set up

SFRC cylinders were extracted from the floor-slabs according to Fig. 2.15. Two cylinder samples from each floor-slab: one from the central ("B"-samples) and one from the side ("A"-samples) region. As with the slicing method, the samples were taken also near the mould to investigate its effect on the orientation of fibres. Altogether twelve cylinder samples with a diameter of 10 cm each were

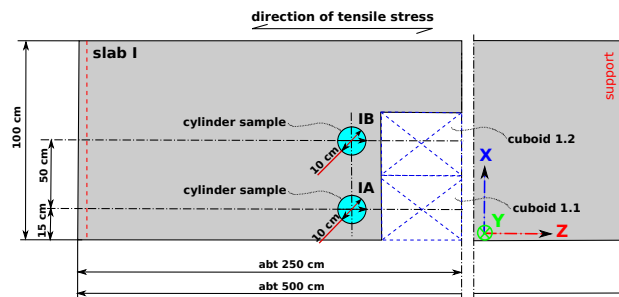
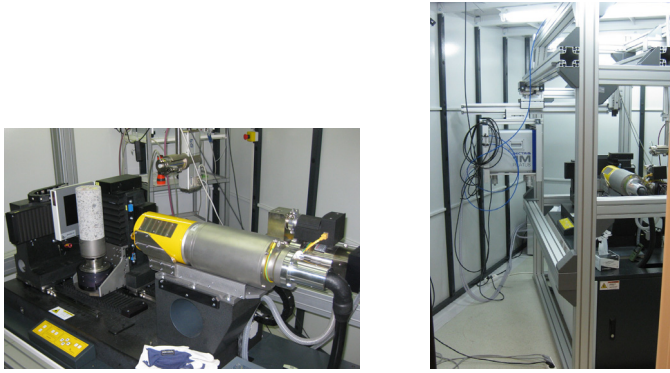


Figure 2.15. The position of an analysed cylinder in the floor-slab.

extracted. The cylinder samples were scanned in the Department of Physics in Helsinki University (Finland) using the experience of micro-tomography group, i.e. Jussi-Petteri Suuronen, Aki Kallonen and Prof. Ritva Serimaa. The X-ray Micro-tomography Laboratory is built around a state-of-the-art μ CT scanner Nanotom 180 NF supplied by phoenix|xray Systems + Services GmbH (Wunstorf, Germany), Fig. 2.16. The circumference of a cylinder sam-

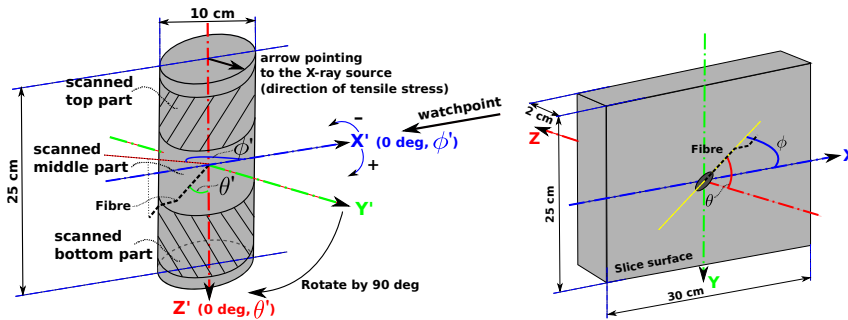


(a) A cylinder sample in the μ CT scanner.

(b) The room with the μ CT scanner.

Figure 2.16. The scanner nanotom supplied by Phoenix|x-ray Systems.

ple was scanned with an angular step of 1 deg leading to 360 projection images made. The scanning of a sample took approximately three hours. Within the first phase of scanning, the middle part of the cylinder samples was scanned, Fig. 2.17(a). The height of the middle part was about 7 cm. The second phase included the scanning of the top and bottom parts of four cylinder samples. The choice of the scanning area was connected with the technical capabilities



(a) Definition of the orientation angles θ' and ϕ' measured from the μ CT data. The position of the scanned top, middle and bottom parts. The coordinate system in Avizo Fire.

(b) The slicing coordinate system, considered as structural coordinates.

Figure 2.17. The representation of μ CT and slicing coordinate systems.

of the used scanning machine, i.e. the size of the detector (LCD screen) and with the intention to investigate the differences of fibre orientations in the bulk and close to formwork or free surface. Besides, the chosen scanning order made it possible to analyse fibre orientation distributions in compressed and tensioned cross-sectional areas.

To improve the quality of projection images, a median filter (implemented

in ImageJ) was applied prior to reconstruction. The reconstruction from the projection images was implemented using an FDK-algorithm-based [55] reconstruction software 'datos|x rec' supplied by the manufacturer. Within the reconstruction procedure 'highEdge' filtering was used to intensify the contrast between the fibres and concrete matrix. A 3D edge preserving smoothing algorithm [56], followed by a dual threshold binarisation (function hysteresis in Avizo Fire), was applied for enhancing the purity of images. A 3D volume image obtained by μ CT scanning provided a picture of actual fibre orientations in the concrete matrix, Fig. 2.18.

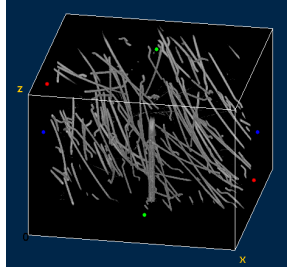


Figure 2.18. Thresholded volume image of a middle part of a cylinder sample scanned by μ CT. Still showing an artefact in the middle (data courtesy of Aki Kallonen [1]).

2.4.2 Fibre orientation analysis

Before analysing the orientation of fibres, a skeletonised representation (centre lines) of the fibres was calculated using Avizo Fire 6.2 software (VSG, France). The centre lines of the fibres were received as a thinning of binarised data using the XSkeleton pack extension to Avizo. However, as many fibres in the data were touching each other, the skeleton also contained the connections between the fibres. To solve this problem, the skeleton processing algorithm was applied as a function in Matlab software (Mathworks Inc., USA), which can be called directly from Avizo Fire. After the application of skeleton processing algorithm, the 3D-orientation (the inclination θ' and in-plane ϕ' angles) of fibres was calculated using Avizo. From Fig. 2.17 it is clear, that the coordinate system in Avizo Fire does not coincide with the slicing system. In order to match the coordinates from Avizo Fire with those of the slicing, it is necessary to rotate the Y' and Z' about the X' axis by 90 degrees anticlockwise, Fig. 2.17(a). Since the position of each skeleton-object—fibre—in Avizo Fire is defined in spherical coordinates, it is transformed into Cartesian coordinates and rotated by 90 degrees anticlockwise around the X' -axis using the rotation matrix. Afterwards, the rotated Cartesian coordinates should be again

transformed to spherical ones. Finally, Avizo Fire coordinates considered as laboratory ones are adjusted to the slicing coordinates which are regarded as the structural ones.

2.5 Summary of developed and implemented measuring methods

During the research two methods for measuring fibre orientations have been developed and implemented: coupled measuring approach in slicing—DC-conductivity testing combined with image analysis— and μ CT scanning.

The slicing method is obviously suitable for straight and hooked-end fibres. In the case of corrugated fibres this method probably will not give good results, since the reconstruction or tracking of the whole length of a fibre will be a tricky task. When applying the slicing method, one should take into account the ratio between the thickness of a slice and the length of a fibre. The shorter the fibres are, the thinner the slices should be. But the minimum thickness of a slice will still depend on a type of used equipment, i.e. cutting method (diamond saw, water jet cutting, laser etc.). The maximum thickness of a slice depends on a method for the reconstruction of fibre orientations. While using the slicing with photometry, the maximum thickness of a slice is conditioned by the length of an aligned fibre added by some increment to guarantee that the trace of a fibre appears only on one slice surface. In the case of the ‘tracking the trace’ of a fibre, the slice should be as thin as allowed by machine tooling. In the inclined state the fibre should leave two traces, i.e. one trace per slice surface, Fig. 2.19(a). The precision of the results in photometric analysis depends

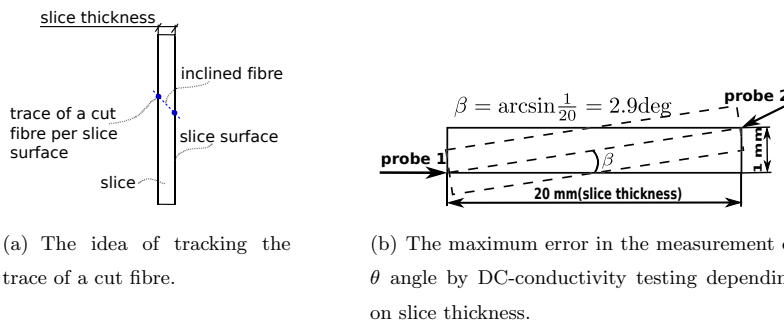
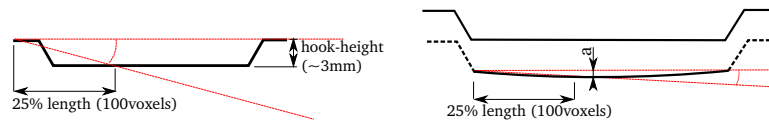


Figure 2.19. The influence of slice thickness on results while tracking the trace of a cut fibre.

a lot on the resolution of the image. The higher the resolution, the more accurately the shape of a cut fibre can be detected. In addition, the accuracy of photometric analysis can be increased by the polishing of slice surface [15].

The biggest drawback of the slicing with photometry is the inability to measure the in-plane angle ϕ in the range from $[0^\circ, 360^\circ]$. Thus, the application of this method is not sufficient for the analysis of the spatial orientation of fibres. DC-conductivity testing utilizing the coordinates received in the image analysis acts as an extension of photometry and solves the ambiguity in the direction of a fibre as it measures the in-plane angle within the interval from $[0^\circ, 360^\circ]$. The possible sources for the errors while utilizing DC-conductivity testing are:

- input coordinates from photometry: accuracy of fibre coordinates is about 1 px, drift after correction up to ± 0.5 mm;
- probe not in the centre of the fibre trace: the maximum error in the measurement of θ angle can be 2.9° , Fig. 2.19(b);
- step size of a step motor. The full step size of a motor can be received as the division of a circle, i.e. 360° , by the amount of steps in a motor. The latter data comes from the technical characteristics of a motor. An error from one step size of a probe has a minor influence on the precision of measurements while the influence of an error arising from the conversion of coordinates, i.e. from pixels to millimetres has the main impact;
- touching fibres: if the fibres are touching, then it is possible to have the conductivity, even if the traces on opposite surfaces belong to different fibres. This seems to be a rare event, as the statistics from the photometry and DC-conductivity testing have similar tendencies;
- hooked-ends of the fibres: if one cut appears to be within the hooked-end of a fibre, this can lead to an error of $\max 10^\circ$ ($\arctan \frac{\text{hook-height}}{\text{slice thickness}}$) in the orientation of this fibre, depending on the thickness of a slice and angle of the fibre, Fig. 2.20(a);
- slightly curved middle part of a fibre, Fig. 2.20(b). This can lead to an error below 2° – 3° in the fibre orientation ($\arctan \frac{a}{\min \text{ obj.length}}$).



(a) Maximum error due to only part of fibre being in scanned volume. (b) Maximum error due to curvature of fibre.

Figure 2.20. Errors connected with the geometry of a fibre.

There is one more factor affecting the accuracy of DC-conductivity measurements: the probability of measuring a fibre is θ -dependent and large inclination angles are underestimated. The probability for one fibre to “leave a trace” on the second surface, under the condition that it “left a trace” on the first surface, is

$$p = \max \left\{ \cos \theta - \frac{\text{slice thickness}}{\text{fibre length}}, 0 \right\}. \quad (2.5)$$

X-ray micro-tomography (μ CT) method allows to look inside a robust material such as concrete and obtain 3D data about the spatial orientation distribution of fibres. With the equipment used in the research, the actual scanning time was 2–2.5 hours, depending on the imaging parameters, and the reconstruction of a series of the scans into 3D map of a sample took a few minutes. It should be emphasized, that the used μ CT equipment is primarily for scanning millimetre-sized samples at sub-micrometer resolution, (i.e. three orders of magnitude higher than the 128.3 μm per voxel) and lacks the beam power necessary to image large samples of highly absorbing materials like concrete. The CT systems which are more suitable for scanning SFRC have a lower precision and higher beam power. The time required for the image processing and statistical analysis is largely dependent on the available computer hardware. The measuring results received by μ CT scanning are incomparable in accuracy to other methods. The main sources of error while applying μ CT scanning to SFRC are:

- only one of the hooked-ends is within the scanning area, max. error is 13° , from $\Delta\alpha = \arctan \frac{\text{hook-height}}{\text{min obj.length}}$, Fig. 2.20(a). This error could be reduced or eliminated by cutting the hooks away with the kink-detection algorithm;
- resolution of the scan, error about 1 px (0.1283 mm), max error is $\Delta\alpha = \arctan \frac{0.1283\text{mm}}{12.83\text{mm}} = 0.6^\circ$ (1 px off the correct position and 100 px length of object);
- the middle part of the fibres is not exactly straight, but slightly curved, Fig. 2.20(b);
- manual setting of the thresholds;
- skeleton processing: touching fibres and corresponding automatic splitting by the self-written program.

Having reviewed the sources of errors in both measuring methods, it can be stated, that the precision of DC-conductivity testing is close to the one of μ CT. The last two error points in DC-conductivity (hooked-ends of the fibres and slightly curved middle part of a fibre) are of the same magnitude as in μ CT scanning.

3. Fibre orientation distributions in tested floor-slabs

Numerical estimates of the distribution parameters of fibre orientations in the samples taken from the tested slabs were calculated using the R-programming language [57] and several packages for statistical computing and graphics [2, 58, 59, 60, 61, 62, 63, 64, 65]. The statistical outcomes revealed the variations of fibre orientation distributions along the all axes of the tested slabs: along the X -axis between the side and centre samples, along the Y -axis between the top, middle and bottom parts of the cylinder samples and along the Z -axis between the cuboids and cylinder samples, Fig. 3.1.

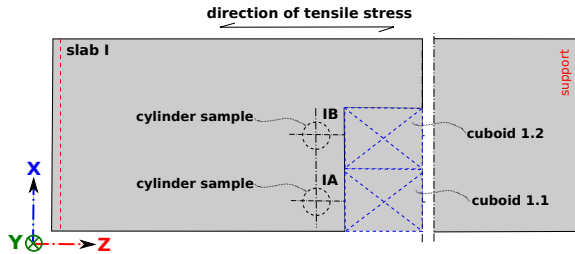


Figure 3.1. The coordinate system in the tested slabs and the location of samples.

These features indicate that a theory capable to consider the spacial—three-dimensional—nature of SFRC material properties is needed. The floor slabs tested were cast applying a casting (site-specific) technology, which can be used in actual construction works. The observed three-dimensional nature of fibre orientations confirms the need to elaborate the manufacturing and the casting processes for SFRC, which will allow to track and control the orientation distribution of fibres.

3.1 Density distribution of the inclination angle θ

The problem with the photometry approach is the ambiguity in the direction of a fibre as the measurement of the in-plane angle ϕ covers only the range

from $[0^\circ, 180^\circ]$. Accordingly, DC-conductivity measurements acting as the improvement of the photometry were performed on the surfaces of the slice nr 11, which belongs to the cuboid 1.1, Fig. 2.10. This choice was done in order to examine the statistics of fibre orientations in the slab with the highest bending capacity, Fig. 2.3.

Fig. 3.2 represents the statistics received by DC-conductivity measurements from the slice 11 (cuboid 1.1). Fig. 3.2(d) actually demonstrates the optimal orientation distribution of fibres since the alignment of fibres almost coincides with the direction of the tensile stress in the slab, Fig. 3.1.

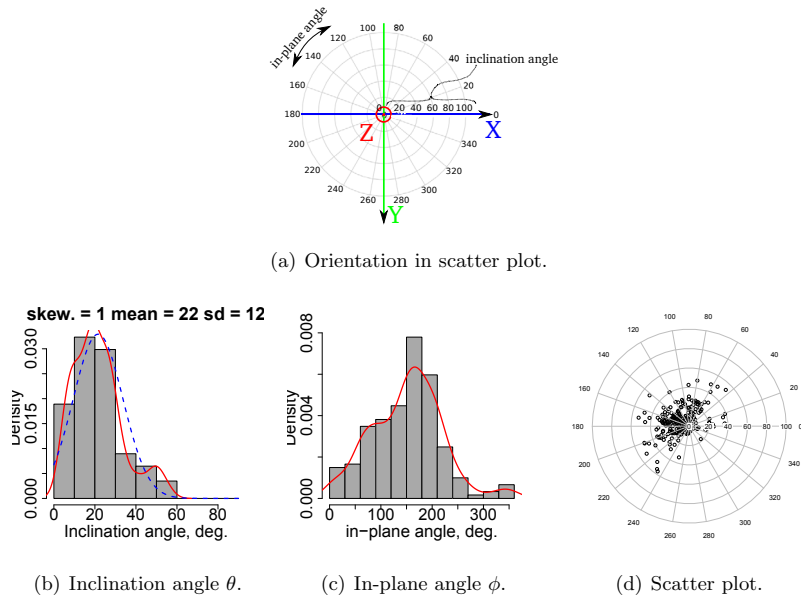


Figure 3.2. Statistics of fibre orientations measured by DC-conductivity testing on slice 11 belonging to the cuboid 1.1. Figs. (b), (c) represent the density distribution—solid line—of the inclination angle θ and in-plane angle ϕ respectively. In Fig. (b) the skewness is compared with the Normal distribution—dashed line. In (a) the radius represents the inclination angle θ and in-plane angle ϕ is on circumference.

The influence of DC-conductivity testing on the results of photometry is presented in Fig. 3.3, where a quite similar behaviour in the density histograms of the inclination angle θ can be noticed. Both analysing approaches gave a positive skewness for the probability density distribution of the θ angle. The density histogram of the in-plane angle ϕ measured by DC-conductivity testing covers the whole range from $[0^\circ, 360^\circ]$, which makes DC-conductivity more preferable to photometry.

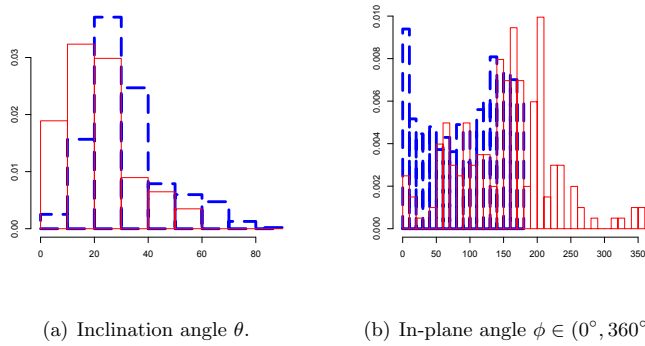


Figure 3.3. The effect of the measuring approaches on the probability density distribution of the inclination angle θ and in-plane angle ϕ . A dashed line represents the results received by photometry (cuboid 1.1) and a solid line the results of DC-conductivity testing (slice 11 from cuboid 1.1).

The photos of slice surfaces were utilised to check the compliance of the density distributions received for the inclination angle θ . Checking was made by the two-sample bootstrap Kolmogorov-Smirnow-test (K-S test, function `ks.boot` from [2]) with a significance level of $\alpha = 5\%$ as threshold. The density distributions for the inclination angle θ are obtained considering every fourth slice surface in a cuboid to account each fibre only once within a given volume. According to the results given in Table 3.1, only the distribution functions of the central cuboids have received higher p -values. In the cuboid 1.2 the p -value received for the inclination angle θ with the null hypothesis of Gumbel distribution was 0.04, which is close but still below the acceptance threshold of 5%.

Table 3.1. Results of the two-sample bootstrap Kolmogorov-Smirnov test (function `ks.boot` from [2]) applied on the density distribution of the inclination angle θ in the slab 1. Reduced cuboid refer to the cuboid, where only every fourth slice surface is taken into account.

	Cuboid 1.1 (side of a slab)				Cuboid 1.2 (centre of a slab)			
Inclination angle θ								
	whole cuboid		reduced cuboid		whole cuboid		reduced cuboid	
Distribution	D	p -value	D	p -value	D	p -value	D	p -value
Gaussian	0.114	e-16	0.125	e-16	0.076	e-16	0.078	e-09
Gamma	0.061	e-16	0.066	e-10	0.044	e-10	0.044	0.0033
Gumbel	0.069	e-16	0.065	e-09	0.035	1.7e-06	0.035	0.0374
Weibull	0.098	e-16	0.116	e-16	0.075	e-16	0.059	1.9e-05
Log-normal	0.049	e-16	0.058	1.7e-07	0.038	2.5e-07	0.040	0.0108

None of the distribution functions of the side cuboids have passed the testing and hence all null hypotheses should be rejected [66].

The most important conclusion of the performed statistical tests is that the

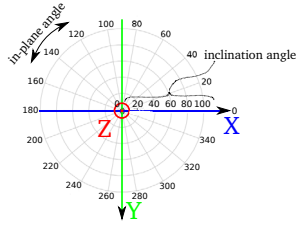
distribution of the inclination angle θ in the central cuboids (in a bulk) does not obey the Gaussian (Normal) distribution, in contrast to the results received earlier [11]. The results of the two-sample bootstrap Kolmogorow-Smirnow-tests in other cuboids are presented in Appendix A.2.

3.2 Variations of fibre orientation distributions along the X - and Y -axes of the slabs

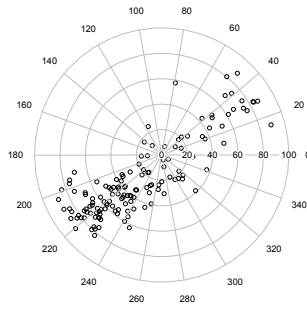
The statistical analysis included the definition of fibre orientation distributions in the side and centre cylinder samples scanned by μ CT. In addition, fibre orientation distributions were specified in the top, middle and bottom parts of the cylinder samples. The top and bottom sections were scanned in four cylinders: 1A, 1B, 4A, 4B, but the middle sections were scanned in all cylinder samples. Each section covers about 7 cm of the height of a cylinder, Fig. 2.17(a). The inclination θ and in-plane ϕ angles for each fibre are defined according to Fig. 2.17(b).

Fig. 3.4 demonstrates fibre orientation distributions in the side and centre cylinders and along the height of the whole cylinder samples 1A and 1B. In the bottom section of a cylinder 1A, Fig. 3.4(f), the orientation of fibres is the most optimal since it has the best coincidence with the direction of principal tensile stress of a floor-slab, Fig. 3.1. The fibre orientation distributions are different between the side, Fig. 3.4 (b),(d),(f), and centre, Fig. 3.4 (c),(e),(g), cylinders, and also along the height of the whole cylinder sample, Figs. 3.4(b), 3.4(d), 3.4(f). This indicates the locality of fibre orientation distributions meaning that this phenomenon may exist through the volume of the whole structure. Fig. 3.5 represents probability density histograms of the inclination angle θ and in-plane angle ϕ in the cylinder sample 1A. The outcomes belong to the top, middle and bottom parts of a cylinder. Fig. 3.5(g) demonstrates concentration of fibre alignments on smaller inclination angles. This can be explained by the influence of the formwork whereas the scatter of the inclination angles in Fig. 3.5(a) indicates a free surface.

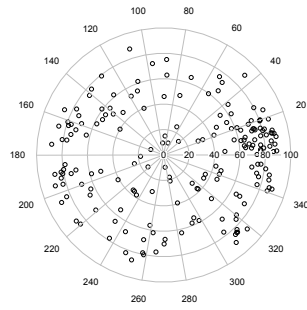
The statistics of fibre orientation distributions for the other cylinder samples scanned by μ CT are presented in Appendix A.3.



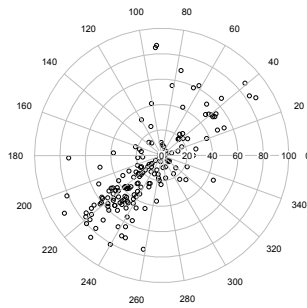
(a) Orientation in scatter plots.



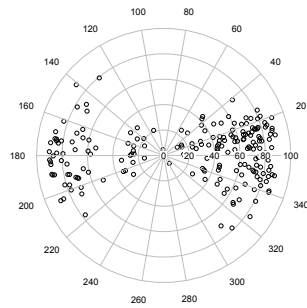
(b) **Top part.** Cylinder 1A.



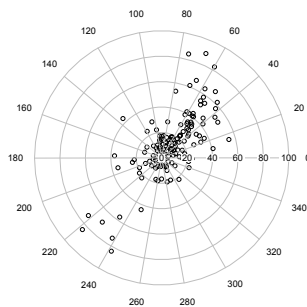
(c) Cylinder 1B.



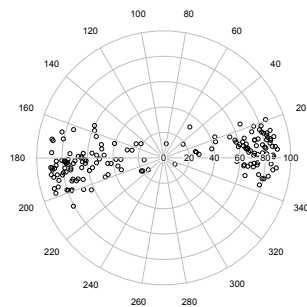
(d) **Middle part.** Cylinder 1A.



(e) Cylinder 1B.



(f) **Bottom part.** Cylinder 1A.



(g) Cylinder 1B.

Figure 3.4. Scatter plots of fibre orientation variations measured by μ CT between the side (cylinder 1A) and centre (cylinder 1B), and along the height of the whole cylinder samples. In (a) the radius represents the inclination angle θ and in-plane angle ϕ is on circumference. Z-axis corresponds to the direction of the tensile stress in a slab, Fig. 3.1.

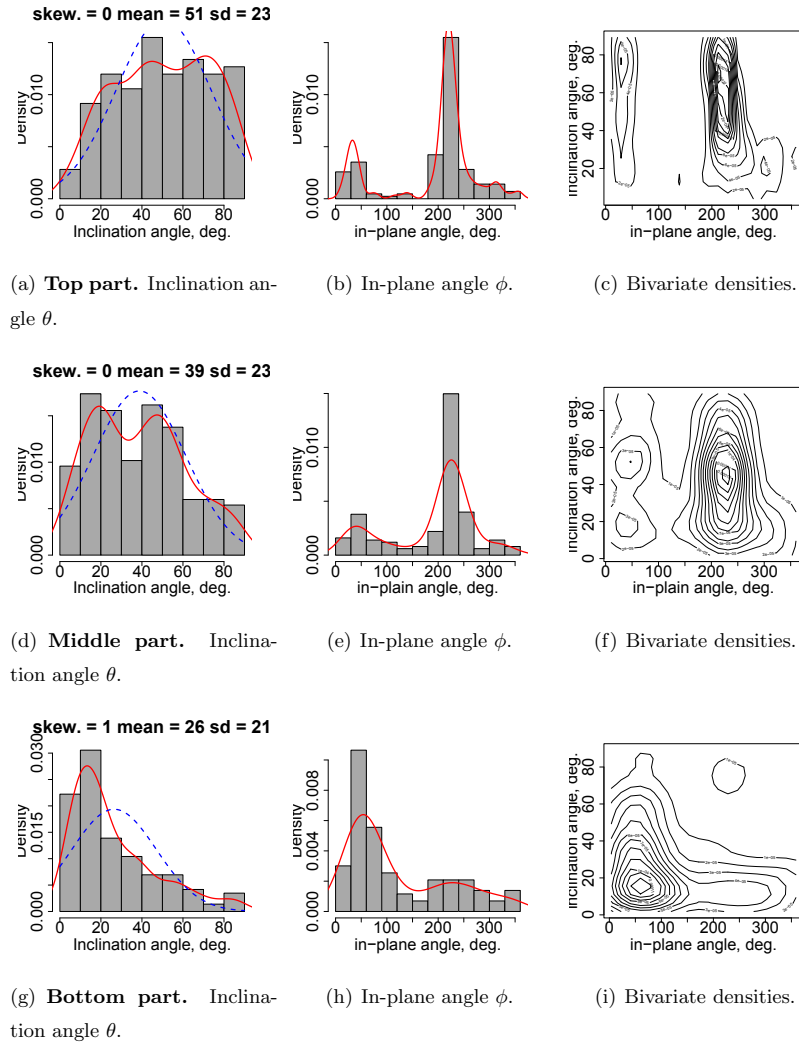


Figure 3.5. Fibre orientation variations measured by μ CT along the height of the whole cylinder sample 1A. Figs. (a),(b),(c) represent the statistics for the top; (d),(e),(f) for the middle and (g),(h),(i) for the bottom parts of the cylinder. Figs. (a),(b), (d),(e), (g),(h) represent the density distribution—solid line—of the inclination angle θ and in-plane angle ϕ . In Figs. (a),(d),(g) the skewness is compared with the Normal distribution—dashed blue line. Figs. (c),(f),(i) represent the bivariate densities of the inclination angle θ and in-plane angle ϕ .

3.3 Variations of fibre orientation distributions along the Z -axis of the slabs

Comparison of the outcomes of fibre orientation distributions in the samples taken from the different places along the Z -axis of the slabs, Fig. 3.1 (cuboids and cylinders), revealed the dissimilarity in the density distribution of the in-

clination angle θ , Figs. 3.6, 3.7. In cuboids, measured by slicing with photometry, the density distribution of the inclination angle θ had a positive skewness while in the cylinders, measured by μ CT, it was a negative one. Such location dependent variations of fibre orientation distributions point out a strong locality of fibre orientations in the studied structures.

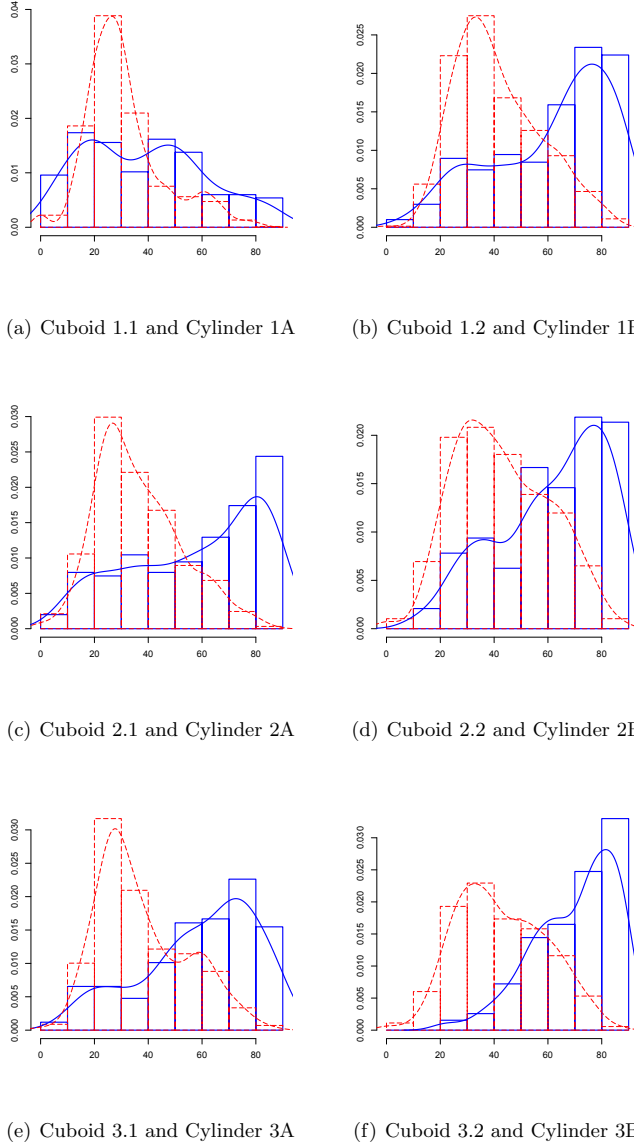
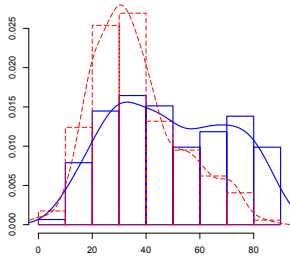
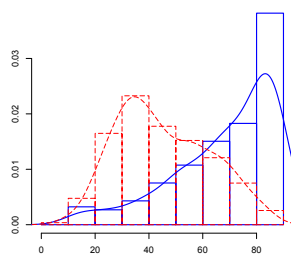


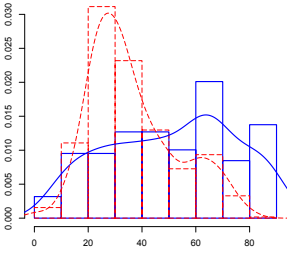
Figure 3.6. Differences in the probability density histograms of the inclination angle θ according to the location along the Z axis of the slabs, Fig. 3.1, in the middle sections of the cuboids 1.1–3.2 and cylinder samples 1A–3B. A dashed line represents the results of cuboids measured by photometry and a solid line the results of cylinder samples measured by μ CT.



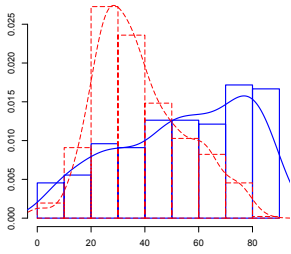
(a) Cuboid 4.1 and Cylinder 4A



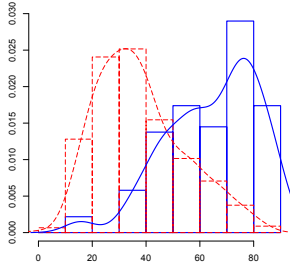
(b) Cuboid 4.2 and Cylinder 4B



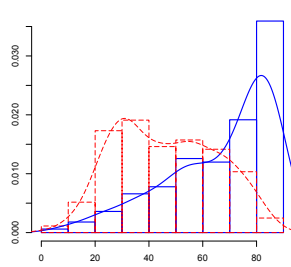
(c) Cuboid 5.1 and Cylinder 5A



(d) Cuboid 5.2 and Cylinder 5B



(e) Cuboid 6.1 and Cylinder 6A



(f) Cuboid 6.2 and Cylinder 6B

Figure 3.7. Differences in the probability density histograms of the inclination angle θ according to the location along the Z axis of the slabs, Fig. 3.1, in the middle sections of the cuboids 4.1–6.2 and cylinder samples 4A–6B. A dashed line represents the results of cuboids measured by photometry and a solid line the results of cylinder samples measured by μ CT.

4. Constitutive mappings

4.1 General terms and conditions for material models

The balance equations [67] are formed of basic and constitutive fields. The basic fields such as the mass density, momentum density and energy density are not linked to material properties. The constitutive fields depend on the thermodynamic process and on the material [29]. The constitutive equation establishes the linkage between the stress tensor \mathbf{S} and deformation tensor \mathbf{E} . The constitutive equations must hold material objectivity conditions implying two statements [29]:

All corresponding quantities of the domain and of the range of the constitutive mappings are objective meaning that they shall transform under changing of the reference frame by an Euclidean transformation rules (e.g. orthogonal transformation).

The analytical form of a constitutive function must be the same in any frame of reference meaning its invariance from the coordinate system.

The first statement specifies the type of the state space variables to be tensors. The second statement defines the type of functions satisfying coordinate invariance. Such functions are isotropic tensor functions meaning that a tensor function is isotropic if and only if the forms of its component functions are the same for all orthogonal bases [68, 69, 70].

4.2 Behaviour of SFRC

The tensile strength of SFRC depends on the alignment of fibres in the concrete matrix. In a tensioned SFRC member, where all fibres are aligned with

each other, as well as with the principal tensile stress, the fibres have the optimal orientation and thus contribute to structural tensile capacity with the highest efficiency. In an actual situation, the fibres can be oriented not only in one direction, but an amount of fibres may also be aligned along several directions or almost randomly. The existence of this phenomenon has been proven by the measuring of fibre orientations performed in this research, [Publication IV](#). The measurement results demonstrate that a part of fibres tends to align along some preferred direction, which may however be different in the samples taken from the same structural members. In a typical concrete member, which is reinforced by steel bars in the direction of expected tensile stresses, the stress behaviour would have an orthotropic character. A similar situation may be present in a SFRC member and the problem is to identify and model the directions of fibre alignments. Thus, the constitutive relation for SFRC is justified to be developed based on an orthotropic material model. In addition, a linear dependence between stresses and deformations is assumed. Let us examine a bended concrete member. In general, a compressed concrete is an elasto-plastic material, where simultaneously both the elastic and plastic deformations are developing. As a consequence, the relation between the stress and deformation should be non-linear. In a bended concrete, until the first cracks have appeared in the tension zone of a cross-section the relation between the stress and deformation can be considered as linear, Fig. 4.1. As

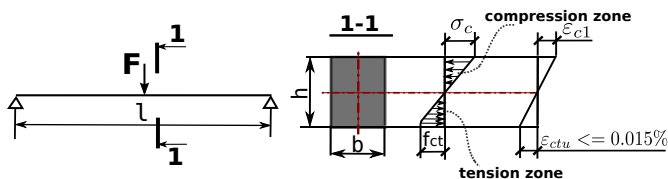


Figure 4.1. A bended concrete member. The stage at the very beginning of the formation of cracks in the tension zone. f^{ct} denotes the tension strength of concrete, σ^c is the concrete stress in compression zone, ϵ^{c1} is the concrete strain in compression, and $\epsilon^{ctu} \leq 0.015\%$ is the concrete ultimate strain in tension.

soon as cracks are occurring in the tension zone, the deformations start to grow rapidly and, as a result, the member breaks suddenly in a brittle manner. Drawing a parallel with SFRC it can be stated, that the properties of this material have a similar brittle character as it was pointed out by the behaviour of the full-size floor slabs tested. According to the diagrams of the bending test, Section 2.3.1 Fig. 2.3, the modes of the load-deformation curves were linear at the beginning and dropped sharply without any occurrence of plateaus (plasticity) in three out of six slabs. Essentially, the brittle failure of SFRC is a consequence from a relative low volume percentage (concentration)

of fibres, which typically, for example, in an elevated floor-slab is 1% – 2% per cubic meter of concrete. Increasing the concentration of fibres is economically not reasonable since the volume percentage of common reinforcement in the elevated floor-slab is usually between 1.25% – 1.5%. Besides, the high concentration of fibres will induce the clumping (clustering) of fibres, which will cause difficulties in the manufacturing of SFRC. The only difference between the behaviour of a bended concrete and SFRC member can be the appearance of the first cracks at a higher load in SFRC. In this regard, the preferred physically linear-elastic range is an appropriate way to approximate the behaviour of SFRC as also in load-bearing structures based on SFRC the cracking caused by loading should not be allowed.

4.3 Orthotropic elasticity of one meso-volume element of SFRC

The effective elasticity of one meso-volume element of SFRC, Fig. 4.2, can involve two basic terms: concrete matrix and short steel fibres.

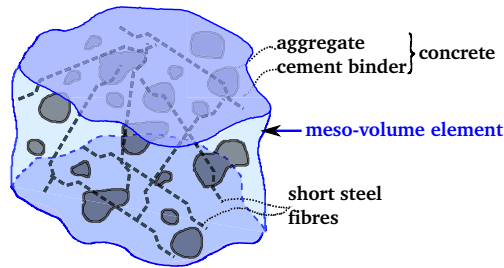


Figure 4.2. One meso-volume element of SFRC.

The fibres are assumed to contribute orthotropically and the concrete matrix is an isotropic part, such as:

$$\langle 4 \rangle \mathbf{C}^{(c)} = \underbrace{\dots}_{\text{isotropic concrete matrix}} + \underbrace{\dots}_{\text{orthotropic influence of fibres}}, \quad (4.1)$$

where $\langle 4 \rangle \mathbf{C}^{(c)}$ is the orthotropic meso-elasticity of the composite. The choice of a meso-scale for a characteristic volume (representative volume element, RVE) of SFRC is related to measured fibre orientations in the tested floor slabs, Section 3. The measurements revealed that the orientation of fibres has a local character and can vary in three-dimensions.

In the following, the energy approach is used for the constitutive mappings. The reasoning is based on assuming a hyperelastic material. The strain-energy density function W of the hyperelastic material depends on a deformation gra-

dient \mathbf{F} and is a potential function for the stress tensor [68],

$$\mathbf{S}(\mathbf{F}) = \frac{\partial}{\partial \mathbf{F}} W(\mathbf{F}) , \quad \langle 4 \rangle \mathbf{C}(\mathbf{F}) = \frac{\partial \mathbf{S}}{\partial \mathbf{F}} = \frac{\partial^2}{\partial \mathbf{F} \partial \mathbf{F}} W(\mathbf{F}) , \quad (4.2)$$

where $\langle 4 \rangle \mathbf{C}$ is the Lagrangian elastic modulus or 4th order elasticity tensor.

4.3.1 Modelling of isotropic concrete matrix and orthotropic influence of short steel fibres

The independence of the material from the reference frame means that its strain-energy density is invariant upon orthogonal transformations. This implies that a strain-energy density function of a hyperelastic material can be expressed as a function of the *Lagrangian* strain tensor \mathbf{E} [68], such as

$$W(\mathbf{F}) = W_E(\mathbf{E}) . \quad (4.3)$$

The anisotropic properties of materials are characterised by their symmetry group [69]. The anisotropic influence of short steel fibres may be described by the orthotropic material model, which is symmetric with respect to three mutually orthogonal planes meaning that the material properties remain unchanged by the reflections from these planes. The normal of a plane is called the principal material direction (material symmetry axis). Generally, an orthotropic material has three orthogonal planes and three principal material directions, $\{\mathbf{m}^i\}_{i=1,2,3}$, Fig. 4.3. Choosing a unit vector \mathbf{l}^1 directed in one of

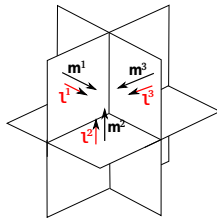


Figure 4.3. Orthotropic material with three principal material directions $\mathbf{m}^1, \mathbf{m}^2, \mathbf{m}^3$ called as material symmetry axes. $\mathbf{l}^1, \mathbf{l}^2, \mathbf{l}^3$ are the unit vectors along the symmetry axes.

the principal material directions, the following term can be defined [69]:

$$\mathbf{Q}\mathbf{l}^1 = \pm \mathbf{l}^1 , \quad \forall \mathbf{Q} \in \text{Orth}^3 . \quad (4.4)$$

Implementing an outer product of the unit vector \mathbf{l}^1 with itself, leads to a structural tensor \mathbf{L}^1 :

$$\mathbf{L}^1 = \mathbf{l}^1 \otimes \mathbf{l}^1 , \quad \mathbf{Q}\mathbf{L}^1\mathbf{Q}^T = \mathbf{L}^1 , \quad \forall \mathbf{Q} \in \text{Orth}^3 . \quad (4.5)$$

The tensor \mathbf{L}^1 is called the structural tensor since it lays down the material or structural symmetry [69]. Thereafter, the structural tensors \mathbf{L}^2 and \mathbf{L}^3

directed in two other principal material directions \mathbf{I}^2 and \mathbf{I}^3 may be composed in the same way as in Eq. (4.5). The structural tensors have the following features [69]:

$$\begin{aligned} \mathbf{L}^i : \mathbf{L}^j &= (\mathbf{I}^i \otimes \mathbf{I}^i) : (\mathbf{I}^j \otimes \mathbf{I}^j) = 0, \quad i \neq j, \\ (\mathbf{L}^i)^2 &= \mathbf{L}^i, \quad \sum_i^3 (\mathbf{L}^i) = \mathbf{I}, \quad \text{tr}(\mathbf{L}^i) = 1. \end{aligned} \quad (4.6)$$

The strain-energy density function for orthotropic material symmetry with three principal material directions can be defined as:

$$\begin{aligned} W_{E,\text{ortho}}(\mathbf{Q}\mathbf{E}\mathbf{Q}^T, \mathbf{Q}\mathbf{L}^i\mathbf{Q}^T) &= W_{E,\text{ortho}}(\mathbf{E}, \mathbf{L}^i), \quad \forall \mathbf{Q} \in \text{Orth}^3, \\ \mathbf{L}^i &= \mathbf{I}^i \otimes \mathbf{I}^i, \quad i = 1, 2, 3, \end{aligned} \quad (4.7)$$

where Orth^3 is the symmetry group, which includes all orthogonal transformations in three-dimensional space. In the case of isotropic material the distinctly directed structural tensors \mathbf{L}^i are simplified to arbitrarily chosen ones resulting in direction independent deformation and, consequently, the condition for material symmetry of isotropic material takes the following form:

$$W_{E,\text{iso}}(\mathbf{Q}\mathbf{E}\mathbf{Q}^T) = W_{E,\text{iso}}(\mathbf{E}), \quad \forall \mathbf{Q} \in \text{Orth}^3. \quad (4.8)$$

From Eq. (4.7) follows that the isotropy is a special case of orthotropy. Hence, the concrete matrix is considered to be isotropic.

The condition Eq. (4.7) is satisfied if the strain-energy density function is represented as an isotropic tensor function. The isotropic tensor function can be represented as a function of its principal traces $\{\text{tr}(\mathbf{E}^n)\}_{n=1,2,3}$, as the latter ones are uniquely defined by the eigenvalues of the characteristic polynomial [69]. Accordingly, the system of principal traces (or eigenvalues) forms the irreducible basis, the elements of which are independent, i.e. they cannot be expressed in a unique form in terms of the others. Taking into account the properties of the structural tensors Eq. (4.6), the strain-energy density function for orthotropic material symmetry can be represented by the isotropic tensor function of the arguments among which are the structural tensors:

$$\begin{aligned} W_{E,\text{ortho}}(\mathbf{E}, \mathbf{L}^i) &= \hat{W}_{E,\text{ortho}} \left(\underbrace{\text{tr}(\mathbf{E}), \text{tr}(\mathbf{E}^2), \text{tr}(\mathbf{E}^3)}_{\text{for isotropy}}, \underbrace{\text{tr}(\mathbf{L}^i), \text{tr}((\mathbf{L}^i)^2), \text{tr}((\mathbf{L}^i)^3)}_{\text{tr}(\mathbf{L}^i) = 1}, \right. \\ &\quad \left. \underbrace{\text{tr}(\mathbf{E}\mathbf{L}^i), \text{tr}(\mathbf{E}^2\mathbf{L}^i)}_{\text{tr}(\mathbf{E}), \text{tr}(\mathbf{E}^2) \text{ if isotropic}}, \underbrace{\text{tr}(\mathbf{E}(\mathbf{L}^i)^2)}_{\text{tr}(\mathbf{E}\mathbf{L}^i)}, \underbrace{\text{tr}(\mathbf{E}^2(\mathbf{L}^i)^2)}_{\text{tr}(\mathbf{E}^2\mathbf{L}^i)} \right) \\ &= \hat{W}_{E,\text{ortho}} \left(\text{tr}(\mathbf{E}\mathbf{L}^i), \text{tr}(\mathbf{E}^2\mathbf{L}^i), \text{tr}(\mathbf{E}^3) \right). \end{aligned} \quad (4.9)$$

Ten irreducible invariants in Eq. (4.9) are explained by the symmetry of the tensor-arguments, which reduces the number of permutations. The representation of an isotropic tensor function by the system of irreducible invariants, which depend on the amount and properties of tensor-arguments can be found in [71, 72]. Eq. (4.9) explicitly demonstrates that the traces $\text{tr}(\mathbf{E}\mathbf{L}^i)$, $\text{tr}(\mathbf{E}^2\mathbf{L}^i)$ can be utilised for the isotropic case since if \mathbf{L}^i are arbitrarily chosen, then $\text{tr}(\mathbf{E}\mathbf{L}^i) = \text{tr}(\mathbf{E})$, $\text{tr}(\mathbf{E}^2\mathbf{L}^i) = \text{tr}(\mathbf{E}^2)$. The 1st order term in Eq. (4.9) vanishes in order to satisfy the deformation and stress-free natural state. The trace $\text{tr}(\mathbf{E}^3)$ represents the non-linear isotropic matrix. Thereby, dropping the 1st order as well as 3rd order terms and considering that the 2nd order term $\text{tr}(\mathbf{E}^2\mathbf{L}^i)$ can be equivalently presented as [70]:

$$\text{tr}(\mathbf{E}^2\mathbf{L}^i) = \text{tr}(\mathbf{E}\mathbf{L}^i\mathbf{E}\mathbf{L}^j), \quad i > j, \quad (4.10)$$

the strain-energy density function for the orthotropic elastic material with three symmetry axes can be specified by the combination of mixed traces of Eq. (4.9), such as:

$$\hat{W}_{E,\text{ortho}}^{(2)}(\mathbf{E}, \mathbf{L}^i) = \frac{1}{2} \sum_{i,j=1}^3 \gamma^{ij} \text{tr}(\mathbf{E}\mathbf{L}^i) \text{tr}(\mathbf{E}\mathbf{L}^j) + \sum_{i,j \neq i}^3 G^{ij} \text{tr}(\mathbf{E}\mathbf{L}^i\mathbf{E}\mathbf{L}^j). \quad (4.11)$$

The latter model is known as the orthotropic St. Venant-Kirchhoff material [70]. The constants γ^{ij} , G^{ij} in Eq. (4.11) are the Lamé constants, which are given in terms of Young's modulus Y and Poisson's ratio ν , but here they are direction dependent, i.e. they refer to the material symmetry axes and planes, respectively. The values of γ^{ij} , G^{ij} define if the material is orthotropic or transversely isotropic. For isotropic case the elastic constants will be equal for all directions, i.e. $\gamma^{ij} = \gamma$, $G^{ij} = G$. The differentiation of the strain-energy function Eq. (4.11) with respect to \mathbf{E} leads to the orthotropic 2nd Piola-Kirchhoff stress tensor $\mathbf{S}_{E,\text{ortho}}$ [68]:

$$\mathbf{S}_{E,\text{ortho}} = \frac{\partial}{\partial \mathbf{E}} \hat{W}_{E,\text{ortho}}^{(2)}(\mathbf{E}, \mathbf{L}^i) = \sum_{i,j=1}^3 \gamma^{ij} \text{tr}(\mathbf{E}\mathbf{L}^j) \mathbf{L}^i + 2 \sum_{i,j \neq i}^3 G^{ij} \mathbf{L}^i \mathbf{E} \mathbf{L}^j, \quad (4.12)$$

which is linear with respect to \mathbf{E} . For isotropic material Eq. (4.12) is as follows:

$$\mathbf{S}_{E,\text{iso}} = \frac{\partial}{\partial \mathbf{E}} \hat{W}_{E,\text{iso}}^{(2)}(\mathbf{E}) = \gamma \mathbf{I} \text{tr}(\mathbf{E}) + 2G \mathbf{E}, \quad (4.13)$$

which is common form of Hooke's law.

Hereinafter, in Eqs. (4.11-4.13) the linearised hyperelasticity $\mathbf{E} \approx \boldsymbol{\varepsilon}$ implying the insignificant difference between the spatial and material coordinates of a material point in space, is utilised. Thus, the 2nd Piola-Kirchhoff stress tensor \mathbf{S} , usually used for finite deformations, is employed for the case of linear elasticity. The advantage of the 2nd Piola-Kirchhoff stress tensor is its symmetry

and the differentiation gives the *second* elasticity tensor (4th order elasticity tensor), which has minor and major symmetries. Essentially, by assuming $\frac{\partial}{\partial x} \approx \frac{\partial}{\partial X}$ the different stress measures shall give the same result.

The material symmetry axes of one meso-volume element of SFRC and, consequently, the direction dependent elasticity constants γ^{ij} , G^{ij} are identified utilising the orientation state of fibres, which is quantified by the orientation tensors and the orientation distribution function [29, 31].

In theory, the orientation distribution function (ODF) $f(\mathbf{n})$, where $\mathbf{n}(\theta, \phi)$ is a unit vector associated with the orientation of a rod-like particle (fibre) in space as e.g. in Fig. 4.4, is defined as the probability of finding a fibre between the angles θ_1 and $\theta_1 + d\theta$ and ϕ_1 and $\phi_1 + d\phi$, such as:

$$P(\theta_1 \leq \theta \leq \theta_1 + d\theta, \phi_1 \leq \phi \leq \phi_1 + d\phi) = f(\theta_1, \phi_1) \sin \theta_1 d\theta d\phi. \quad (4.14)$$

All possible directions of a fibre comply with a unit sphere S^2 (radius $r = 1$).

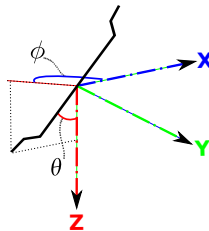


Figure 4.4. The orientation of a fibre (rod-like particle) in space. θ is the inclination angle, $\theta \in (0^\circ, 180^\circ)$, ϕ is the in-plane angle, $\phi \in (0^\circ, 360^\circ)$. In pCT scanning the ranges of definitions $\theta \in (0^\circ, 90^\circ)$ and $\phi \in (0^\circ, 360^\circ)$ are used.

The l -order symmetric orientation tensor $O_{\mu_1 \dots \mu_l}$ can be composed by l -order outer products of a unit vector \mathbf{n} with itself and then integrating the result with the ODF, $f(\mathbf{n})$, over all possible directions:

$$O_{\mu_1 \dots \mu_l} = \oint_{S^2} f(\mathbf{n}) n_{\mu_1} \otimes \dots \otimes n_{\mu_l} d^2 n. \quad (4.15)$$

The l -order orientation tensor contains the information about the lower order tensors. For example, the 4th order orientation tensor includes the information of the 2nd order orientation tensor. The symmetric traceless or irreducible part of the l -order orientation tensor, in the mesoscopic continuum theory called the l -order alignment tensor (AT) $A_{\mu_1 \dots \mu_l}$ [29], does not contain the information about the lower order tensors. The ATs are able to account for the anisotropy of the system, for example, the 2nd order alignment tensor represents the deviation of the orientation tensor from isotropy. Hence, in

the case of the isotropic distribution the ATs just vanish. In the mesoscopic continuum theory the l -order AT is defined as follows:

$$A_{\mu_1 \dots \mu_l} = \oint_{S^2} f(\mathbf{n}) \overline{n_{\mu_1} \otimes \dots \otimes n_{\mu_l}} d^2n, \quad (4.16)$$

where $\overline{n_{\mu_1} \otimes \dots \otimes n_{\mu_l}}$ is the l -order symmetric tensorial product of a vector \mathbf{n} (in Cartesian coordinates) from which the trace is removed and which gives an l -order symmetric irreducible tensor. The symmetric irreducible tensors are spherical harmonics [30], which belong to square-integrable functions L^2 and form, in case of a unit sphere, a complete orthonormal basis on L^2 , Appendix A.1. Any square-integrable function on a unit sphere can be expanded into the series of $(2l+1)$ main spherical harmonics. The ODF $f(\mathbf{n})$ is quadratically integrable function and it is defined on a unit sphere, and thus it may be decomposed into the series of symmetric irreducible tensors $\overline{n_{\mu_1} \otimes \dots \otimes n_{\mu_l}}$ forming a complete orthonormal basis, and the ATs are acting as the expansion coefficients:

$$f(\mathbf{n}) = \underbrace{\frac{1}{4\pi} \cdot f_0}_{\hat{f}(\mathbf{n})} + \frac{1}{4\pi} \sum_{l=1}^{\infty} \frac{(2l+1)!!}{l!} A_{\mu_1 \dots \mu_l} \overline{n_{\mu_1} \otimes \dots \otimes n_{\mu_l}}, \quad (4.17)$$

$$f_0 = \oint_{S^2} f(\mathbf{n}) d^2n = 1,$$

where $l!$ is the factorial $l! = l \cdot (l-1) \cdot \dots \cdot 2 \cdot 1$ and $(2l+1)!! = (2l+1) \cdot (2l-1) \cdot \dots \cdot 3 \cdot 1$ denotes the ‘‘factorial with double steps’’ [29, 30, 73]. The first term in Eq. (4.17) represents the zero harmonic, which is a constant equal to the mean integral value $\hat{f}(\mathbf{n})$ (can be interpreted as a mathematical expectation) of the original function $f(\mathbf{n})$ on a sphere. All other harmonics starting from $l=1$ approximate the deviation $(f(\mathbf{n}) - \hat{f}(\mathbf{n}))$ of the original function $f(\mathbf{n})$ from its mean value (can be interpreted as variance). If the expansion coefficients in a complete orthonormal basis are known then the original function may also be considered as known since the sum of the squares of all expansion coefficients equals to the mean square of the function given on a sphere [37], Appendix A.1. This can be used to approximate the ODF from the experimental data, e.g. measuring of fibre orientations using X-ray micro-tomography scanning (μ CT). The ODF satisfies the following conditions:

ODF is even, i.e. $f(\mathbf{n}) = f(-\mathbf{n})$,

ODF is normalised, i.e. $\int_{\theta=0}^{\pi} \int_{\phi=0}^{2\pi} f(\theta, \phi) \sin \theta d\theta d\phi = \oint_{S^2} f(\mathbf{n}) d^2\mathbf{n} = 1$.

Accordingly, as the ODF is even in \mathbf{n} , the odd-order alignment tensors (as well as the orientation tensors) in Eq. (4.17) vanish.

The eigenvalues λ^i ($|\lambda^1| \geq |\lambda^2| \geq |\lambda^3|$) of the 2^{nd} order alignment tensor can be used to introduce a scalar order-parameter S needed to evaluate how well the rod-like particles are aligned with each other [74, 75]. The parameters can be determined by firstly defining the order parameter tensor as $\mathbf{P} = \frac{3}{2}\mathbf{A}$ (the reason for the $\frac{3}{2}$ becomes clear later) with S being its according-to-amount largest eigenvalue:

$$S = \mathbf{d}^1 \cdot \underbrace{\mathbf{P}}_{:=\frac{3}{2}\mathbf{A}} \cdot \mathbf{d}^1, \quad \mathbf{d}^1 \cdot \mathbf{d}^1 = 1. \quad (4.18)$$

Inserting the definition of the alignment tensor Eq. (4.16) combined with the exchange of scalar products and integration leads to

$$S = \oint_{S^2} \left(\frac{1}{2}(3(\mathbf{d}^1 \cdot \mathbf{n})^2 - 1) \right) f(\mathbf{n}) d^2\mathbf{n} = \left\langle \frac{1}{2}(3(\mathbf{d}^1 \cdot \mathbf{n})^2 - 1) \right\rangle, \quad (4.19)$$

which is the average of the second Legendre polynomial $P_2(\mathbf{d}^1 \cdot \mathbf{n})$ and can be further rewritten by introducing $\mathbf{d}^1 \cdot \mathbf{n} =: x$ or $\alpha = \langle \mathbf{n}, \mathbf{d}^1 \rangle$ into

$$S = \langle P_2(\mathbf{d}^1 \cdot \mathbf{n}) \rangle \quad (4.20)$$

$$= \langle P_2(x) \rangle \quad (4.21)$$

$$= \langle P_2(\cos \alpha) \rangle, \quad (4.22)$$

where the meaning of $\alpha = \langle \mathbf{n}, \mathbf{d}^1 \rangle$ or $\mathbf{d}^1 \cdot \mathbf{n}$ is presented in Fig. 4.5. The values

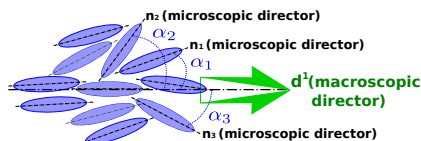


Figure 4.5. A macroscopic director \mathbf{d}^1 , i.e. the direction of average orientation of particles, corresponds to the eigenvector of the eigenvalue λ^1

of the scalar order-parameter are assumed in the range $S \in [-\frac{1}{2}, 1]$, where the following values correspond to special configurations: $S = 1$ corresponds to the transversely isotropic material symmetry with well aligned fibres, $S = 0$ to the isotropy and $S = -\frac{1}{2}$ describes the plane transversely isotropic case. Here one can see, that the choice of the factor $\frac{3}{2}$ leads directly to the correct coefficients in the Legendre polynomial and to have $S = 0$ for isotropy (no order) [76].

In addition, a biaxiality parameter, which measures the non-symmetry of the distribution with respect to \mathbf{d}^1 , Fig. 4.6, can be introduced in the following way (compare Eq. (4.18)):

$$\frac{2}{3}S = \lambda^1 \quad (4.23)$$

$$-\frac{1}{3}S - b_S = \lambda^2 \quad (4.24)$$

$$-\frac{1}{3}S + b_S = \lambda^3, \quad (4.25)$$

where $b_S = \frac{1}{2}(\lambda^3 - \lambda^2) = \text{sign}(S)b$ and the biaxiality $b \in [0, \frac{1}{3}|S|]$ [74, 75, 77]. The limits follow from the ordering of the eigenvalues, and $b_S = 0$ means, that the distribution is rotation symmetric around \mathbf{d}^1 . As the tensor is traceless, the sum of the eigenvalues λ^i vanishes, and so the sum of the left-hand sides of Eqs. (4.23), (4.24), (4.25) needs to vanish.

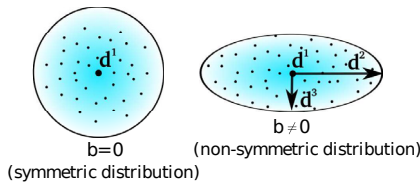


Figure 4.6. Biaxiality. $\mathbf{d}^1, \mathbf{d}^2, \mathbf{d}^3$ are the eigenvectors of the 2^{nd} order alignment tensor.

The 2^{nd} order alignment tensor is used to define the material symmetry axes of one meso-volume element of SFRC. The unit vectors \mathbf{l}^i (Fig. 4.3, Eq. (4.7)) pointing to the principal material directions are chosen to be the normalised eigenvectors $\mathbf{d}^1, \mathbf{d}^2, \mathbf{d}^3$ of the 2^{nd} order alignment tensor. The orientation distribution function $f(\mathbf{n})$ is utilised to estimate the contributions of fibres in the directions of the eigenvectors thus defining the direction dependent meso-elasticity constants of the composite, i.e. γ^{ij}, G^{ij} .

4.3.2 State space for SFRC

As the constitutive equations are different for different materials, the introduction of the concept of the state space is necessary. The variables to be included to the state space depend on the physical problem and on the material [29]. The mechanical properties of the studied composite depend on the orientation of short steel fibres and thus the state space for SFRC shall include the variables associated with the orientation distribution of fibres in a volume element. As it was stated in the previous section, the normalized eigenvectors \mathbf{d}^i of the 2^{nd} order alignment tensor \mathbf{A} are utilised to assign the material meso-symmetry. The orientation distribution function $f(\mathbf{n})$ is weighting the amount of fibres together with their elastic properties in the direction of the considered material meso-symmetry axis.

Hence, a possible state space for one meso-volume element of SFRC:

$$Z : = \left(Y^{(m)}, Y^{(f)}, \nu^{(m)}, V^{(m)}, V^{(f)}, \varepsilon^{(c)}, \mathbf{d}^i(\mathbf{A}), f(\mathbf{n}) \right), \quad (4.26)$$

with $V^{(m)} = 1 - V^{(f)}$,

where $Y^{(m)}$, $Y^{(f)}$ are the Young's modulus of the concrete and steel fibres respectively, $\nu^{(m)}$ is the Poisson's ratio of the concrete, $V^{(m)}$, $V^{(f)}$ are the volume fractions of the concrete and fibres, $\varepsilon^{(c)}$ is the average infinitesimal strain of the composite as long as the bond acts between the steel fibres and the concrete. The average strain is an equivalent strain, which includes the strains of both concrete and steel fibres since a complete bond is assumed between concrete and steel. This is usually justified by some identical physical and mechanical properties of concrete and steel, such as:

- while hardening the concrete adheres to the steel, and thus in a structure the relative deformations of both materials are equal;
- thermal expansion coefficients of concrete and steel are approximately the same, and thus the changes in the ambient temperature do not cause internal stresses in SRFC structures.

4.3.3 Orientation-weighted meso-elasticity of fibres in material meso-symmetry axes

Essentially, the system of eigenvectors, $\mathbf{d}^1, \mathbf{d}^2, \mathbf{d}^3$ forms the new orthonormal coordinate system—material meso-symmetry coordinates, which define the meso-scale of the composite, Fig. 4.7.

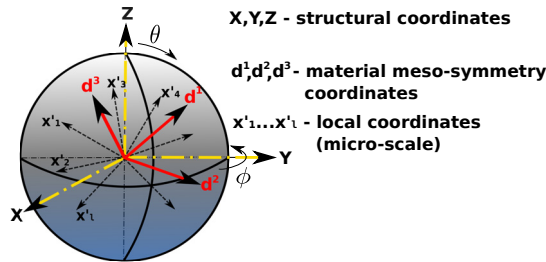


Figure 4.7. The position of the unit vectors—fibres— $x^1 \dots x^3$ relative to structural X, Y, Z and material meso-symmetry $\mathbf{d}^1, \mathbf{d}^2, \mathbf{d}^3$ coordinates.

In order to estimate the contribution of fibres to the directions of the meso-symmetry axes, it is necessary to transform the fibres from their local or micro-scale coordinates into the coordinates characterised by the structural reference frame, Fig. 4.8. Since only the tensile strength of the composite is under consideration, the stretching ability of an individual fibre can be characterised solely by its Young's modulus along its longitudinal axis. Elasticity of a fibre

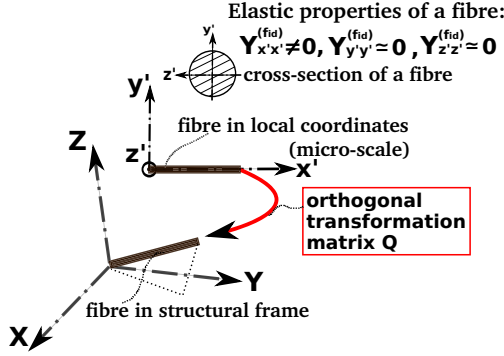


Figure 4.8. Transformation of a fibre from local to structural coordinates. $Y_{x'x'}^{(fia)}$ is the Young's modulus of a fibre along the longest axis in local coordinates. $Y^{(m)}$ is the Young's modulus of the matrix.

in its radial direction is assumed to be insignificant, Fig. 4.8. Applying the orthogonal transformation matrices $\mathbf{Q}(\mathbf{n})$, describing a rotation of the coordinate system, to the fourth-order-elasticity-tensor of a single fibre with one non-zero elasticity modulus $\langle 4 \rangle \mathbf{C}^{(fia)}$, and weighting with the given orientation distribution function $f(\mathbf{n})$, the orientation-weighted orthotropic meso-elasticity of fibres in the structural reference frame is obtained. The following step is to perform one more orthogonal transformation to get the orientation-weighted orthotropic meso-elasticity of fibres in material meso-symmetry coordinates determined by the eigenvectors of the 2^{nd} order alignment tensor, Fig. 4.7. In the mathematical formulation the described steps can be written as follows:

$$C_{ijkl}^{(f_{str})} = \oint_{S^2} Q_{im}(\mathbf{n}) Q_{jn}(\mathbf{n}) Q_{ko}(\mathbf{n}) Q_{lp}(\mathbf{n}) C_{mnop}^{(fia)} f(\mathbf{n}) d^2 \mathbf{n}, \quad (4.27)$$

where $C_{ijkl}^{(f_{str})}$ is the orientation-weighted orthotropic meso-elasticity tensor of fibres in structural coordinates, $Q_{im}(\mathbf{n})$ is the transformation matrix per one index of the 4^{th} order elasticity tensor of an individual fibre $C_{mnop}^{(fia)}$, and $f(\mathbf{n})$ is the considered orientation distribution function. The transformation matrices in Eq. (4.27) are identical and composed as a dot product (scalar multiplication) of two rotation matrices $\mathbf{R}^z(\phi)$, $\mathbf{R}^y(\theta)$, Fig. 4.9 and Eq. (4.28).

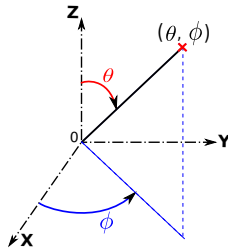


Figure 4.9. Definition of the inclination angle θ and in-plane angle ϕ .

$$\mathbf{Q}(\mathbf{n}) = \mathbf{R}^z(\phi) \cdot \mathbf{R}^y(\theta), \quad \text{where } \theta \in [0, \pi], \quad \phi \in [0, 2\pi] \quad (4.28)$$

$$R_{ij}^z(\phi) = \begin{pmatrix} \cos \phi & -\sin \phi & 0 \\ \sin \phi & \cos \phi & 0 \\ 0 & 0 & 1 \end{pmatrix}, \quad R_{ij}^y(\theta) = \begin{pmatrix} \cos \theta & 0 & -\sin \theta \\ 0 & 1 & 0 \\ \sin \theta & 0 & \cos \theta \end{pmatrix}$$

The further transformation of $C_{ijkl}^{(fstr)}$, which reads as:

$$C_{mnop}^{(fms)} = \hat{Q}_{mi} \hat{Q}_{nj} \hat{Q}_{ok} \hat{Q}_{pl} C_{ijkl}^{(fstr)}, \quad (4.29)$$

gives the orientation-weighted orthotropic meso-elasticity tensor of fibres in material meso-symmetry coordinates. The transformations in Eq. (4.29) diagonalize the tensor $C_{ijkl}^{(fstr)}$ since the transformation matrices are composed of the eigenvectors of the 2^{nd} order alignment tensor, such as:

$$\hat{Q}_{mi} = \begin{pmatrix} d_{11} & d_{12} & d_{13} \\ d_{21} & d_{22} & d_{23} \\ d_{31} & d_{32} & d_{33} \end{pmatrix}, \quad \text{where} \quad (4.30)$$

$$\mathbf{d}^1 = (d_{11}, d_{21}, d_{31}), \quad \mathbf{d}^2 = (d_{12}, d_{22}, d_{32}), \quad \mathbf{d}^3 = (d_{13}, d_{23}, d_{33}).$$

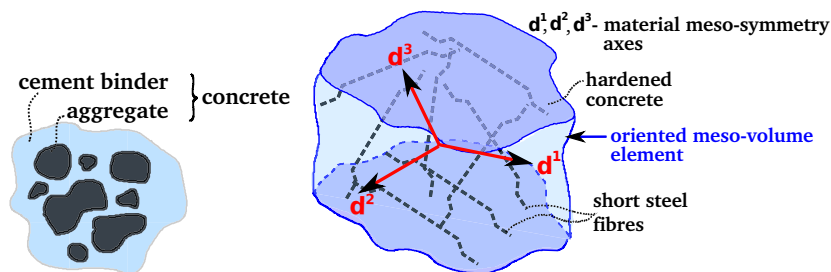
An important property of the orientation-weighted orthotropic meso-elasticity of fibres is that it averages out the heterogeneities—orientations of individual fibres—between the three meso-symmetry axes. From Eq. (4.29) one may specify the orientation-weighted orthotropic elasticity constants for fibres γ^{ij} ($i, j = 1, 2, 3$) and G^{ij} ($i, j = 1, 2, 3; i \neq j$) referring to the material meso-symmetry directions and planes. The latter constants are utilised in the orthotropic material model for one meso-volume element of SFRC.

$$\begin{aligned} \gamma^{11} &= C_{1111}^{(fms)}, & \gamma^{22} &= C_{2222}^{(fms)}, & \gamma^{33} &= C_{3333}^{(fms)} \\ \gamma^{23} &= C_{2233}^{(fms)}, & \gamma^{13} &= C_{1133}^{(fms)}, & \gamma^{12} &= C_{1122}^{(fms)} \\ G^{23} &= C_{2323}^{(fms)}, & G^{13} &= C_{3131}^{(fms)}, & G^{12} &= C_{1212}^{(fms)} \\ \gamma^{32} &= \gamma^{23}, & \gamma^{31} &= \gamma^{13}, & \gamma^{21} &= \gamma^{12} \end{aligned} \quad (4.31)$$

4.4 Constitutive relation for one meso-volume element of SFRC

A complete bond between the concrete and steel fibres results in the Taylor assumption [78], which assumes no fluctuations (equivalent deformations) within the characteristic volume element of a composite. The chosen linear-elastic

range and a small volume fraction (concentration) of fibres allow to employ the mean-field homogenisation approach to formulate the constitutive relation for SFRC [23, 79, 80]. Essentially, the concrete is a heterogeneous material consisting of cement binder and aggregate of different fractions, Fig. 4.10(a). Although, the elasticity parameters of the hardened concrete, found, for example, in Eurocode 2 [81], are homogenised since they characterise the concrete strength in general. Accordingly, the mean-field homogenisation, which uses the meso-volume element to specify the meso-symmetry axes, Fig. 4.10(b), can be utilised to approximate the structure and behaviour of SFRC on the macro-scale.



(a) Homogenisation of pure concrete. (b) Homogenised meso-volume element of SFRC specifying the meso-symmetry axes d^1, d^2, d^3 .

Figure 4.10. The mean-field homogenisations.

Physically, non-linearity induced by the cracking of SFRC implies the loss of bond between the concrete and steel fibres, which further activates the anchoring of fibres. This also indicates the difference in stresses and strains of the concrete matrix and steel fibres. Such fluctuations within the meso-volume element shall be considered while modelling the fracture mechanism of SFRC. The approaches, which could be helpful for considering these differences are presented in [23, 79, 82, 83]. The proposed linear-elastic material model is valid in the case of microcracks.

The orthotropic linear-elastic material model developed for the description of anisotropic behaviour of one meso-volume element of SFRC is established employing the isotropic and orthotropic St. Venant-Kirchhoff models with three symmetry directions. The strain-energy density function in material symmetry axes for one representative volume element of SFRC can be composed by the superposition of the isotropic concrete matrix and orthotropic influence of short steel fibres (Section 4.3.1) resulting in the homogenisation of the composite on the meso-scale, Fig. 4.10(b), such as:

$$\begin{aligned}
W(\boldsymbol{\varepsilon}^{(c)}) &= \underbrace{V^{(m)} \left(\frac{1}{2} \gamma (\text{tr}(\boldsymbol{\varepsilon}^{(c)}) \text{tr}(\boldsymbol{\varepsilon}^{(c)})) + G \text{tr}((\boldsymbol{\varepsilon}^{(c)})^2) \right)}_{\text{concrete, isotropic}} + \\
&\quad + \underbrace{V^{(f)} \left(\frac{1}{2} \sum_{i,j=1}^3 \gamma^{ij} \text{tr}(\boldsymbol{\varepsilon}^{(c)} \mathbf{L}^i) \text{tr}(\boldsymbol{\varepsilon}^{(c)} \mathbf{L}^j) + \sum_{i,j \neq i}^3 G^{ij} \text{tr}(\boldsymbol{\varepsilon}^{(c)} \mathbf{L}^i \boldsymbol{\varepsilon}^{(c)} \mathbf{L}^j) \right)}_{\text{fibres, orthotropic}}. \tag{4.32}
\end{aligned}$$

The differentiation of $W(\boldsymbol{\varepsilon}^{(c)})$ leads to a constitutive relation, which has the following form:

$$\begin{aligned}
\mathbf{S}^{(c)} &= \frac{\partial}{\partial \boldsymbol{\varepsilon}^{(c)}} W(\boldsymbol{\varepsilon}^{(c)}) \tag{4.33} \\
&= \underbrace{V^{(m)} \left(\gamma \mathbf{I} \text{tr}(\boldsymbol{\varepsilon}^{(c)}) + 2G \boldsymbol{\varepsilon}^{(c)} \right)}_{\text{concrete, isotropic}} + \underbrace{V^{(f)} \left(\sum_{i,j=1}^3 \gamma^{ij} \text{tr}(\boldsymbol{\varepsilon}^{(c)} \mathbf{L}^j) \mathbf{L}^i + 2 \sum_{i,j \neq i}^3 G^{ij} \mathbf{L}^i \boldsymbol{\varepsilon}^{(c)} \mathbf{L}^j \right)}_{\text{fibres, orthotropic}}. \tag{4.34}
\end{aligned}$$

The further differentiation of Eq. (4.34) gives the orientation-weighted orthotropic meso-elasticity of the composite, which reads as:

$$\begin{aligned}
C_{mnkl}^{(c)} &= \frac{\partial S_{mn}^{(c)}}{\partial \varepsilon_{kl}^{(c)}} = \frac{\partial^2}{\partial \varepsilon_{mn}^{(c)} \partial \varepsilon_{kl}^{(c)}} W(\boldsymbol{\varepsilon}^{(c)}); \tag{4.35} \\
\langle 4 \rangle \mathbf{C}^{(c)} &= \underbrace{V^{(m)} \left(\gamma \mathbf{I} \otimes \mathbf{I} + 2G \langle 4 \rangle \mathbf{I}^S \right)}_{\text{concrete, isotropic}} + \underbrace{V^{(f)} \left(\sum_{i,j}^3 \gamma^{ij} \mathbf{L}^i \otimes \mathbf{L}^j + \sum_{i,j \neq i}^3 2G^{ij} (\mathbf{L}^i \otimes \mathbf{L}^j)^S \right)}_{\text{fibres, orthotropic}}. \tag{4.36}
\end{aligned}$$

The term of fibres in Eq. (4.36) can be written in explicit form as follows:

$$\begin{aligned}
&\sum_{i,j}^3 \gamma^{ij} L_{mn}^i \otimes L_{kl}^j + \sum_{i,j \neq i}^3 2G^{ij} (L_{mn}^i \otimes L_{kl}^j)^S = \\
&= \left(\gamma^{11} L_{mn}^1 L_{kl}^1 + \gamma^{22} L_{mn}^2 L_{kl}^2 + \gamma^{33} L_{mn}^3 L_{kl}^3 + \gamma^{23} L_{mn}^2 L_{kl}^3 + \gamma^{13} L_{mn}^1 L_{kl}^3 + \gamma^{12} L_{mn}^1 L_{kl}^2 + \right. \\
&\quad \left. + \gamma^{32} L_{mn}^3 L_{kl}^2 + \gamma^{31} L_{mn}^3 L_{kl}^1 + \gamma^{21} L_{mn}^2 L_{kl}^1 \right) + \\
&\quad + \left(G^{23} \frac{1}{2} (L_{ml}^2 L_{kn}^3 + L_{mk}^2 L_{ln}^3) + G^{13} \frac{1}{2} (L_{ml}^1 L_{kn}^3 + L_{mk}^1 L_{ln}^3) + G^{12} \frac{1}{2} (L_{ml}^1 L_{kn}^2 + L_{mk}^1 L_{ln}^2) \right)
\end{aligned}$$

4.5 Example calculations of orientation-weighted 4th order meso-elasticity tensors based on experimental data

In this research the ODF is approximated employing the experimental data (Section 4.3.1). The sum expression of the alignment tensors based on the fibre orientations measured by μ CT reads as follows:

$$A_{i_1 \dots i_l} = \frac{1}{N} \sum_{k=1}^N \overline{v_{i_1}^{(k)} \otimes \dots \otimes v_{i_l}^{(k)}}, \tag{4.37}$$

where $v_i^{(k)}$ is the orientation of each fibre (in Cartesian coordinates) and N is the amount of fibres measured by μ CT. In Eq. (4.17) the infinite series for the function $f(\mathbf{n})$ is replaced by a partial sum of finite terms, whereas the M -th partial sum of the series contains $(M + 1)^2$ coefficients [37]. The sum expression for the approximation of the ODF reads:

$$f(\mathbf{v}) = \frac{1}{4\pi} \left(1 + \sum_{l=1}^M \frac{(2l+1)!!}{l!} \left[\frac{1}{N} \sum_{k=1}^N \overline{v_{i_1}^{(k)} \otimes \dots \otimes v_{i_l}^{(k)}} \right] \cdot \overline{v_{i_1} \otimes \dots \otimes v_{i_l}} \right), \quad (4.38)$$

where M is the order of approximation, $\overline{v_{i_1} \otimes \dots \otimes v_{i_l}}$ are the symmetric irreducible tensors considering all possible directions of a fibre, i.e. $\theta \in [0^\circ, 180^\circ]$ and $\phi \in [0^\circ, 360^\circ]$. If $M \rightarrow \infty$ the approximation turns to infinite series of spherical harmonics, which converges absolutely and uniformly to the original function $f(\mathbf{n})$. The approximation implemented using the coefficients defined considering a minimum squared error, Eq. (4.37), provides a good accuracy within the sum of the first expansion terms [37], Appendix A.1.

In the following, the ODF is calculated using the 2^{nd} order alignment tensor, A_{ij} , which defines the main material symmetry axes of one meso-volume element of SFRC. The higher-order alignment tensors are correcting the main symmetry axes received, however, the accuracy provided by the 2^{nd} order tensor is assumed to be acceptable for the present needs of building industry [31]. The calculation of the higher rank tensors and the respective approximation of the ODF need more numerical calculations.

The ODF is defined as a probability and thus it should be normalized. The normalization is implemented utilizing the Riemann sum, which is defined e.g. for the three dimensional case as follows:

$$F_{cart} = \sum_{k=1}^a \sum_{j=1}^b \sum_{i=1}^c f(x^i, y^j, z^k) \Delta x^i \Delta y^j \Delta z^k, \quad (4.39)$$

where $f(x^i, y^j, z^k)$ is the value of approximated function at a given point and $\Delta x^i \Delta y^j \Delta z^k$ are the lengths of intervals (partitions). Since the ODF is defined on a unit sphere, it is necessary to consider the difference between the volume elements in rectangular and spherical coordinates, Fig. 4.11. The Jacobian determinant of the transformation between the volume elements is defined as follows:

$$\frac{\partial(x, y, z)}{\partial(r, \theta, \phi)} = \begin{vmatrix} \sin \theta \cos \phi & r \cos \theta \cos \phi & -r \sin \theta \sin \phi \\ \sin \theta \sin \phi & r \cos \theta \sin \phi & r \sin \theta \cos \phi \\ \cos \theta & -r \sin \theta & 0 \end{vmatrix} = r^2 \sin \theta, \quad (4.40)$$

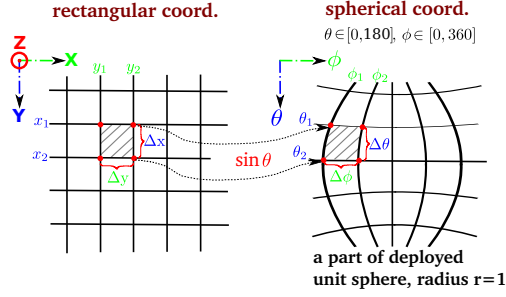


Figure 4.11. The transformation between a rectangular and a spherical volume element.

where $r^2 \sin \theta$ is the actual function that converts a rectangular volume element to spherical coordinates. In the case of a unit sphere ($r^2 = 1$) only $\sin \theta$ shall be used. The transition of a rectangular volume element to spherical coordinates and calculation of the Riemann sum for the unit sphere reads:

$$F_{sph} = \sin \theta^j \cdot \sum_{j=1}^b \sum_{i=1}^c f(x^i, y^j) \Delta x^i \Delta y^j . \quad (4.41)$$

Eqs. (4.42-4.44), Table 4.1 and Figs. 4.12, A.5.4 present calculated fibre orientation parameters of the middle parts (Fig. 2.17(a)) of two cylinder samples 2A and 2B scanned by μ CT. The orientation characteristics include: 2^{nd} order alignment tensor, eigenvalues $\lambda_1, \lambda_2, \lambda_3$, eigenvectors $\mathbf{d}^1, \mathbf{d}^2, \mathbf{d}^3$, scalar order-parameter S , biaxiality b_S , and the approximated orientation distribution functions.

Cylinder 2A

Cylinder 2B

2^{nd} order alignment tensor

$$A_{ij} = \begin{pmatrix} -0.037 & 0.277 & -0.010 \\ 0.277 & 0.038 & -0.013 \\ -0.010 & -0.013 & -0.001 \end{pmatrix}, \quad A_{ij} = \begin{pmatrix} 0.304 & 0.007 & -0.012 \\ 0.007 & -0.244 & -0.070 \\ -0.012 & -0.071 & -0.060 \end{pmatrix} \quad (4.42)$$

Sorted eigenvalues

$$\lambda_1, \lambda_2, \lambda_3 = 0.28, -0.28, -0.002 \quad \lambda_1, \lambda_2, \lambda_3 = 0.31, -0.27, -0.04 \quad (4.43)$$

Eigenvectors of the sorted eigenvalues

$$d_{ij} = \begin{pmatrix} \mathbf{d}^1 & \mathbf{d}^2 & \mathbf{d}^3 \\ -0.656 & 0.753 & 0.042 \\ -0.752 & -0.658 & 0.042 \\ 0.059 & -0.004 & 0.998 \end{pmatrix} \quad d_{ij} = \begin{pmatrix} \mathbf{d}^1 & \mathbf{d}^2 & \mathbf{d}^3 \\ 0.999 & -0.005 & 0.041 \\ 0.018 & 0.947 & -0.320 \\ -0.037 & 0.321 & 0.946 \end{pmatrix} \quad (4.44)$$

The orientation-weighted orthotropic meso-elasticity of fibres in the material meso-symmetry coordinates specified by the eigenvectors $\mathbf{d}^1, \mathbf{d}^2, \mathbf{d}^3$ are presented by employing the Kelvin-Mandel variant of the Voigt notation in Eq. (4.45).

$$\begin{array}{c}
 \text{Cylinder 2A} \\
 C_{\alpha\beta}^{(f_{ms})} = Y(f). \\
 \left(\begin{array}{cccccc}
 0.44 & 0.07 & 0.11 & 0 & 0 & 0 \\
 0.07 & -0.04 & 0.03 & 0 & 0 & 0 \\
 0.11 & 0.03 & 0.20 & 0 & 0 & 0 \\
 0 & 0 & 0 & 0.05 & 0 & 0 \\
 0 & 0 & 0 & 0 & 0.21 & 0 \\
 0 & 0 & 0 & 0 & 0 & 0.13
 \end{array} \right)
 \end{array}
 ,
 \begin{array}{c}
 \text{Cylinder 2B} \\
 C_{\alpha\beta}^{(f_{ms})} = Y(f). \\
 \left(\begin{array}{cccccc}
 0.46 & 0.07 & 0.1 & 0 & 0 & 0 \\
 0.07 & -0.03 & 0.02 & 0 & 0 & 0 \\
 0.1 & 0.02 & 0.20 & 0 & 0 & 0 \\
 0 & 0 & 0 & 0.05 & 0 & 0 \\
 0 & 0 & 0 & 0 & 0.21 & 0 \\
 0 & 0 & 0 & 0 & 0 & 0.14
 \end{array} \right)
 \end{array}
 \quad (4.45)$$

The values of the coefficients in Eq. 4.45 can be called as the probabilities of orientation efficiency. The positive matrix terms describe the optimal fibre orientation from the probabilistic point of view, whereas the negative entry corresponds to a physical case, when the fibres have least effective orientation, and, thus, it can be dealt with by setting it to zero. The situation with negative or zero terms on a main diagonal causes the orientation-weighted orthotropic meso-elasticity tensor of fibres to be indefinite. Nevertheless, the orthotropic elasticity tensor of the composite is still positive definite, since the concrete matrix, being considered as isotropic, compensates the negative-zero-terms of the orthotropic elasticity of fibres, which, from the physical point of view, means the strength of the pure concrete.

Fibre orientation distribution characteristics for the other cylinder samples scanned by μ CT are presented in Appendices A.4, A.5.

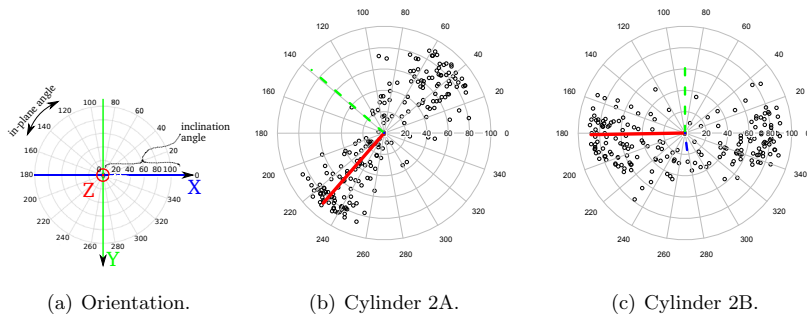


Figure 4.12. Scatter plots of fibre orientations with the triplets of the eigenvectors; \mathbf{d}^1 -solid red line, \mathbf{d}^2 -dashed green line, \mathbf{d}^3 -dot-dashed blue line. \mathbf{d}^1 is the director corresponding to according-to-amount-largest eigenvalue. In (a) the radius represents the inclination angle θ and in-plane angle ϕ is on circumference. Z-axis corresponds to the direction of the tensile stress in a slab, Fig. 3.1.

Table 4.1. The scalar-order parameter S and triplet of the eigenvectors from the 2^{nd} order alignment tensor in spherical coordinates. $S = 1$ corresponds to the transversely isotropic material symmetry, $S = 0$ to isotropy and $S = -\frac{1}{2}$ describes the plane isotropic case. The biaxiality b_S shows the non-symmetry of the distribution with respect to \mathbf{d}^1 .

Cylinder nr.	S	b_S	$\mathbf{d}^1(\theta, \phi)$, deg	$\mathbf{d}^2(\theta, \phi)$, deg	$\mathbf{d}^3(\theta, \phi)$, deg
2A	0.42	0.14	87, 229	90, 139	3, 45
2B	0.46	0.12	88, 181	71, 90	19, 277

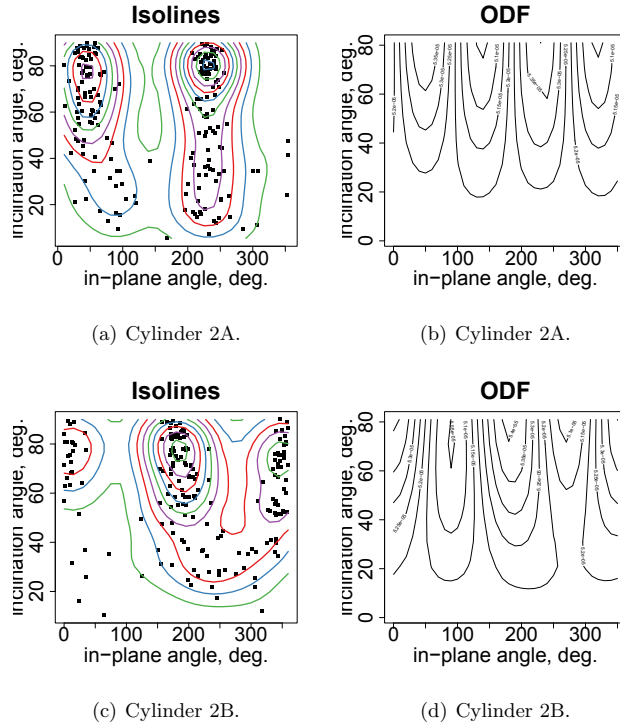


Figure 4.13. The isolines of the measured fibre orientation distributions and the ODFs of fibres approximated using the 2^{nd} order alignment tensor.

4.6 Application areas for the developed material model of SFRC

The application areas of the material model can be utilized by both the numerical computations and the development of SFRC products. The material model developed has a continuous formulation, which makes it attractive for implementing to the finite element programs used in engineering calculations. The results of computer simulations with different fibre orientation distributions may help the manufacturers to better understand the importance of

fibre orientation on the mechanical properties of SFRC and, accordingly, will motivate the development of new technological solutions.

4.6.1 Application in numerical calculations

The orientation tensors (or the alignment tensors) describe the orientation state of fibres compactly not only in a sense of representation, but also in a sense of the number of independent variables needed to characterize the orientation of fibres in each spatial (meso-volume) finite element. For example, the orientation state of fibres in a spatial element using the 2^{nd} order alignment tensor can be specified by 5 independent variables, those are 3 elements above the main diagonal and two elements on the main diagonal. The eigenvectors of the 2^{nd} order alignment tensor show the preferred alignment of fibres in each spatial finite element, Fig. 4.14. As a result one can get a vector field,

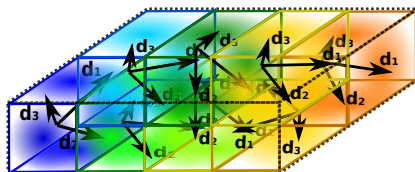


Figure 4.14. SFRC member with a preferred orientation of fibres represented by the triplets of the eigenvectors in each spatial (meso-volume) finite element.

which further may be used to simulate the flow of fibres in a visco-elastic fluid in order to predict fibre orientations.

4.6.2 Application in production technology

A challenge for SFRC manufacturers is to organise the production process to produce a particular orientation of fibres. Ordinary methods for casting concrete structures have not been developed for SFRC and new technological solutions considering the importance of fibre orientations on the mechanical properties of the composite are needed. For example, the optimal fibre orientation can be achieved in a structural member, where only unidirectional principal stress is expected. It may to be realised by utilising of the property of fibres to align along moulds or by the application of some electromagnetic devices. In the case of several principal stresses in a structural member the achievement of the optimal fibre orientation is partially possible and can be fulfilled by the systematic and automated product development as well as by the training of specialised teams for cast-in-place methods. It is expected that the material model encourages the manufacturers by simulating SFRC

properties to develop and evaluate their production technologies.

In general, the material symmetry axes of the composite may not coincide with the load-bearing directions of the structure and thus the information including the symmetry characteristics of the material can be tabularised for different ODFs. These tables may appear to be useful for both the manufacturers and designers as they could reduce the time needed for the analysis of a given ODF. From the industrial point of view, these tables give a tool for manufacturers to optimise production in the respect of composite properties. A designer may select an ODF in accordance with the principal stresses in a structure. To achieve the optimal load-bearing capacity, the selection of the ODF should be based on the expected principal stresses in a structure, which may restrict the approach to cases where load-combinations do not affect the nature of principal stresses.

5. Conclusions and future prospects

During the research two methods, a coupled approach based on sliced samples and μ CT scanning, have been developed and implemented for measuring the orientations of short steel fibres from hardened concrete.

The benefit of implemented slicing method is that a coupled approach allows to measure the orientation of individual fibres in the interval from $[0^\circ, 360^\circ]$, which in addition to eliminating the ambiguity of the in-plane angle present in photometry, and also speeds up the scanning time as the coordinates received in image analysis are used as the input for DC-conductivity testing. An important characteristic while using the slicing method is the ratio between the thickness of a slice and the length of used fibres, Section 2.5. The slicing method is beneficial in the case of straight and hooked-end fibres. If fibres are corrugated, the tracking or searching for the opposite end of a cut fibre may cause difficulties. The success of DC-conductivity testing combined with photometry may depend on a price. In the present experiment the direct material costs were below 500 euros. This price is low and not even comparable to the price of μ CT equipment. Even an improved robot version may cost only a few thousands euros.

The main advantage of the X-ray micro-tomography (μ CT) method is the ability to analyse the orientation of individual fibres based on a 3D voxel representation of a sample. Although the sample size is limited to the order of several dm^3 and the size of structural elements is in the order of m^3 , the precision of the measurements is superior to other methods. The most important parameters of the μ CT machine are the beam power, acceleration voltage, the scanning resolution of X-ray equipment, and computer hardware resources for the processing of scans.

The study confirmed that the concrete samples require a high beam power and acceleration voltage due to the absorbing nature of concrete. CT systems that are capable of delivering over 1500 W X-ray tube power and greater than

400 kV acceleration voltage, [84, 85], while maintaining sufficient resolution, are readily available as turn-key systems that require only limited knowledge of X-ray methods to operate. The values of the equipment used in this study were 11 W and 160 kV.

In conclusion, the main advantages of the measuring methods developed or tested in the study are:

- Combined work of DC-conductivity with photometry:
 - provides fast scanning time;
 - prevents the ambiguity in the in-plane angle;
 - does not require expensive technical solutions.
- μ CT scanning:
 - provides the precision of measurements superior to other methods;
 - offers the availability of CT-systems, which require limited knowledge of X-ray methods.

The outcomes from the measured fibre orientation distributions in the tested floor-slabs revealed a strong spatial heterogeneity in the orientation of fibres, meaning that the alignment of fibres varied along the length (Z -axis), width (X -axis) and the height (Y -axis) of the slabs. Accordingly, the theory that is capable to describe the properties of SFRC in three directions is necessary for the further elaboration of both the production and design of SFRC products.

The result of the modelling part of the research is the formulation of the orthotropic linear-elastic constitutive relation for one meso-volume element of SFRC subjected to small deformations. The approach presented is a mean-field homogenisation utilising a characteristic part of SFRC, i.e. the meso-volume element, which specifies the material symmetry axes on a meso-scale. The model utilises the full orientation information of fibres (two angles in spherical coordinates) and complies with material objectivity conditions. For describing the alignment of short steel fibres, the characteristics of the mesoscopic continuum theory are used: the 2^m order alignment tensor to identify the material meso-symmetry axes and the orientation distribution function to estimate the contribution of fibres to the symmetry axes defined.

The main advantages of the developed orthotropic linear-elastic constitutive model for one meso-volume element of SFRC are:

- the model is invariant under any orthogonal transformations;
- the model is based on dominating directions of the orientation distribution function;
- orthotropic meso-elasticity in the local symmetry axes of the composite are calculated based on the orientation distribution function and the 2nd order alignment tensor.

The future prospect of the material model developed is its implementation into numerical methods, such as finite element or finite volume methods to support the structural design. The material model formulated may also help the manufactures to learn and understand the properties of SFRC to select the most appropriate orientation distribution function for fibres. The adoption of new technologies to manufacturing process of SFRC is perhaps the only way to make the production of this composite controllable. As an outlook for the future research of SFRC, the necessity to study its failure mechanism should be noted. The understanding of SFRC failure may lead to the postulation of an orthotropic non-linear-plastic material model. Besides, the full-size experiments for validation of numerical simulations employing the linear or non-linear constitutive relations are endorsed.

Bibliography

- [1] A. Kallonen, J.-P. Suuronen, and R. Serimaa. μ -CT scans of SFRC. private communication, April 2011.
- [2] J. S. Sekhon. *Matching: Multivariate and Propensity Score Matching with Balance Optimization*, 2010. URL <http://CRAN.R-project.org/package=Matching>. R package version 4.7-11.
- [3] A. Bertram. *Elasticity and Plasticity of Large Deformations – an Introduction*. Springer, 2005.
- [4] A. C. Eringen. *Mechanics of Continua*. Wiley, New York, 1967.
- [5] M. N. L. Narasimhan. *Principles of continuum mechanics*. Wiley, New York, 1993.
- [6] P. Purnell, A. J. Buchanan, N. R. Short, C. L. Page, and A. J. Majumdar. Determination of bond strength in glass fibre reinforced cement using petrography and image analysis. *Journal of Materials Science*, 35:4653–4659, 2000. DOI: [10.1023/A:1004882419034](https://doi.org/10.1023/A:1004882419034).
- [7] Y. Wang, A.-H. Zureick, B.-S. Cho, and D. E. Scott. Properties of fibre reinforced concrete using recycled fibres from carpet industrial waste. *Journal of Materials Science*, 29:4191–4199, 1994. DOI: [10.1007/BF00414198](https://doi.org/10.1007/BF00414198).
- [8] Z. S. Metaxa, M. S. Konsta-Gdoutos, and S. P. Shah. Carbon nanofiber cementitious composites: Effect of debulking procedure on dispersion and reinforcing efficiency. *Cement and Concrete Composites*, 36(0):25 – 32, 2013. DOI: [10.1016/j.cemconcomp.2012.10.009](https://doi.org/10.1016/j.cemconcomp.2012.10.009).
- [9] R. F. Zollo. Fiber-reinforced concrete: an overview after 30 years of development. *Cement and Concrete Composites*, 19(2):107 – 122, 1997. DOI: [10.1016/S0958-9465\(96\)00046-7](https://doi.org/10.1016/S0958-9465(96)00046-7).
- [10] J. Tejchman and J. Kozicki. *Experimental and theoretical investigations of steel-fibrous concrete*. Springer series in geomechanics and geoen지니어ing. Springer, 1st edition, 2010.
- [11] F. Laranjeira. *Design-oriented constitutive model for steel fiber reinforced concrete*. PhD thesis, Universitat Politècnica de Catalunya, 2010. URL <http://www.tdx.cat/TDX-0602110-115910>.
- [12] S. Grünewald. *Performance-based design of self-compacting fibre reinforced concrete*. PhD thesis, Technische Universität

- Delft, 2004. URL <http://repository.tudelft.nl/view/ir/uuid:07a817aa-cba1-4c93-bbed-40a5645cf0f1/>.
- [13] J. Schnell, W. Breit, and F. Schuler. Use of computer-tomography for the analysis of fibre reinforced concrete. In Vlastimil Sruma, editor, *Proceedings of the fib Symposium Prague 2011*, pages 583–586, 2011.
- [14] P. Stroeven and J. Hu. Review paper – stereology: Historical perspective and applicability to concrete technology. *Materials and Structures*, 39:127–135, 2006. DOI: [10.1617/s11527-005-9031-6](https://doi.org/10.1617/s11527-005-9031-6).
- [15] J. Wuest, E. Denarié, E. Brühwiler, L. Tamarit, M. Kocher, and E. Gallucci. Tomography analysis of fiber distribution and orientation in ultra high-performance fiber-reinforced composites with high-fiber dosages. *Experimental Techniques*, 33(5):50–55, 2009. DOI: [10.1111/j.1747-1567.2008.00420.x](https://doi.org/10.1111/j.1747-1567.2008.00420.x).
- [16] S. Barnett, J.-F. Lataste, T. Parry, S. Millard, and M. Soutsos. Assessment of fibre orientation in ultra high performance fibre reinforced concrete and its effect on flexural strength. *Materials and Structures*, 43:1009–1023, 2010. DOI: [10.1617/s11527-009-9562-3](https://doi.org/10.1617/s11527-009-9562-3).
- [17] C. Redon, L. Chermant, J.-L. Chermant, and M. Coster. Assessment of fibre orientation in reinforced concrete using Fourier image transform. *Journal of Microscopy*, 191(3):258–265, 1998. DOI: [10.1046/j.1365-2818.1998.00393.x](https://doi.org/10.1046/j.1365-2818.1998.00393.x).
- [18] L. Ferrara, N. Ozyurt, and M. di Prisco. High mechanical performance of fibre reinforced cementitious composites: the role of “casting-flow induced” fibre orientation. *Materials and Structures*, 44:109–128, 2011. DOI: [10.1617/s11527-010-9613-9](https://doi.org/10.1617/s11527-010-9613-9).
- [19] B. E. Barragán, R. Gettu, M. A. Martin, and R. L. Zerbino. Uniaxial tension test for steel fibre reinforced concrete – aparametric study. *Cement and Concrete Composites*, 25(7):767–777, 2003. DOI: [10.1016/S0958-9465\(02\)00096-3](https://doi.org/10.1016/S0958-9465(02)00096-3).
- [20] L. Ferrara, M. Faifer, and S. Toscani. A magnetic method for non destructive monitoring of fiber dispersion and orientation in steel fiber reinforced cementitious composites — Part 1: method calibration. *Materials and Structures*, pages 1–15, 2011. DOI: [10.1617/s11527-011-9793-y](https://doi.org/10.1617/s11527-011-9793-y).
- [21] N. Ozyurt, T. O. Mason, and S. P. Shah. Non-Destructive Monitoring of Fiber Dispersion in FRCS Using AC-Impedance Spectroscopy. In *Measuring, Monitoring and Modeling Concrete Properties*, pages 285–290. Springer, 2007. DOI: [10.1007/978-1-4020-5104-3](https://doi.org/10.1007/978-1-4020-5104-3).
- [22] E. Becker and W. Bürger. *Kontinuumsmechanik*. Teubner Studienbücher, Stuttgart, 1975.
- [23] M. Taya and R. J. Aresenault. *Metal Matrix Composites: Thermomechanical Behavior*. Pergamon Press, Oxford, 1989.
- [24] aci commitee 544 (Stark et al.). Design considerations for steel fiber reinforced concrete. ACI 544.4R-88, 1999.
- [25] A. Jansson. *Fibres in reinforced concrete structures-analysis, experiments and design*. PhD thesis, Chalmers University of Technology, 2008. URL <http://publications.lib.chalmers.se/records/fulltext/68889.pdf>.

- [26] L. G. Sorelli, A. Meda, and G. Plizzari. Steel fiber concrete slabs on ground: A structural matter. *ACI Structural Journal*, 103:551–558, 2006.
- [27] CNR Advisory Committee on Technical Recommendations for Construction. Guide for the design and construction of fiber-reinforced concrete structures. CNR-DT 204/2006, 2006.
- [28] M. Eik and J. Puttonen. Challenges of Steel Fibre Reinforced Concrete in Load Bearing Structures. *Rakenteiden Mekaniikka*, 44(1):44–64, 2011.
- [29] W. Muschik, C. Papenfuss, and H. Ehrentraut. *Concepts of Continuum Thermodynamics*. Kielec University of Technology, Technische Universität Berlin, 1996.
- [30] H. Ehrentraut and W. Muschik. On Symmetric irreducible tensors in d -dimensions. *ARI - An International Journal for Physical and Engineering Sciences*, 51:149–159, 1998. DOI: [10.1007/s007770050048](https://doi.org/10.1007/s007770050048).
- [31] S. G. Advani and C. L. Tucker III. The use of tensors to describe and predict fiber orientation in short fiber composites. *Journal of Rheology*, 31(8):751–784, 1987. DOI: [10.1122/1.549945](https://doi.org/10.1122/1.549945).
- [32] C. Papenfuss, T. Boehme, H. Herrmann, W. Muschik, and J. Verhas. Dynamics of the size and orientation distribution of microcracks and evolution of macroscopic damage parameters. *Journal of Non-Equilibrium Thermodynamics*, 32(2): 129–142, 2007. DOI: [10.1515/JNETDY.2007.005](https://doi.org/10.1515/JNETDY.2007.005).
- [33] L. Waldmann. Kinetische Theorie des Lorentz-Gases aus rotierenden Molekülen. *Zeitschrift für Naturforschung A - A Journal of Physical Sciences*, 18a:1033–1048, 1963.
- [34] S. Hess. Fokker–Planck-equation approach to flow alignment in liquid crystals. *Zeitschrift für Naturforschung A - A Journal of Physical Sciences*, 31a:1034–1037, 1976.
- [35] S. Hess. Irreversible thermodynamics of nonequilibrium alignment phenomena in molecular liquids and in liquid crystals (1). *Zeitschrift für Naturforschung A - A Journal of Physical Sciences*, 30a:728–738, 1975.
- [36] S. G. Advani and C. L. Tucker III. Closure approximations for three-dimensional structure tensors. *Journal of Rheology*, 34(3):367–386, 1990. DOI: [10.1122/1.550133](https://doi.org/10.1122/1.550133).
- [37] J.M Neiman and L.S Sugairova. Сферические функции и их применение (*Spherical functions and their application*). Московский государственный университет геодезии и картографии (Moscow State University of Geodesy and Cartography), 2005. URL http://vm.miigaik.ru/kollektiv_kafedr/preppages/neiman_um/.
- [38] F. Laranjeira, S. Grünewald, J. Walraven, K. Blom, C. Molins, and A. Aguado. Characterization of the orientation profile in fiber reinforced concrete. *Materials and Structures*, 44:1093–1111, 2011. DOI: [10.1617/s11527-010-9686-5](https://doi.org/10.1617/s11527-010-9686-5).
- [39] F. Laranjeira, C. Molins, and A. Aguado. Predicting the pullout response of inclined hooked steel fibers. *Cement and Concrete Research*, 40(10):1471–1487, 2010. DOI: [10.1016/j.cemconres.2010.05.005](https://doi.org/10.1016/j.cemconres.2010.05.005).

- [40] P.J.J. Dumont, S. Le Corre, L. Orgéas, and D. Favier. A numerical analysis of the evolution of bundle orientation in concentrated fibre-bundle suspensions. *Journal of Non-Newtonian Fluid Mechanics*, 160(2–3):76–92, 2009. DOI: [10.1016/j.jnnfm.2009.03.001](https://doi.org/10.1016/j.jnnfm.2009.03.001).
- [41] T.-H. Le, P.J.J. Dumont, L. Orgéas, D. Favier, L. Salvo, and E. Boller. X-ray phase contrast microtomography for the analysis of the fibrous microstructure of SMC composites. *Composites Part A: Applied Science and Manufacturing*, 39(1):91 – 103, 2008. DOI: [10.1016/j.compositesa.2007.08.027](https://doi.org/10.1016/j.compositesa.2007.08.027).
- [42] M. Krause, J. Hausherr, B. Burgeth, C. Herrmann, and W. Krenkel. Determination of the fibre orientation in composites using the structure tensor and local X-ray transform. *Journal of Materials Science*, 45:888–896, 2010. DOI: [10.1007/s10853-009-4016-4](https://doi.org/10.1007/s10853-009-4016-4).
- [43] C. Redon, L. Chermant, J.-L. Chermant, and M. Coster. Automatic image analysis and morphology of fibre reinforced concrete. *Cement and Concrete Composites*, 21(5-6):403 – 412, 1999. DOI: [10.1016/S0958-9465\(99\)00025-6](https://doi.org/10.1016/S0958-9465(99)00025-6).
- [44] J.F. Lataste, M. Behloul, and D. Breyse. Characterisation of fibres distribution in a steel fibre reinforced concrete with electrical resistivity measurements. *NDT & E International*, 41(8):638 – 647, 2008. DOI: [10.1016/j.ndteint.2008.03.008](https://doi.org/10.1016/j.ndteint.2008.03.008).
- [45] P. Purnell, A. J. Buchanan, N. R. Short, C. L. Page, and A. J. Majumdar. Determination of bond strength in glass fibre reinforced cement using petrography and image analysis. *Journal of Materials Science*, 35:4653–4659, 2000. DOI: [10.1023/A:1004882419034](https://doi.org/10.1023/A:1004882419034).
- [46] P. Stroeven. *Stereology of concrete reinforced with short steel fibres*. PhD thesis, Technische Universiteit Delft, 1986. URL http://repository.tudelft.nl/assets/uuid:fb1416c4-2061-4767-9d5a-925480382d19/Stroeven_1986.pdf.
- [47] J. Buffiere, E. Maire, J. Adrien, J. Masse, and E. Boller. In Situ Experiments with X-ray Tomography: an Attractive Tool for Experimental Mechanics. *Experimental Mechanics*, 50:289–305, 2010. DOI: [10.1007/s11340-010-9333-7](https://doi.org/10.1007/s11340-010-9333-7).
- [48] P. Penttilä, J.-P. Suuronen, S. Kirjoranta, M. Peura, K. Jouppila, M. Tenkanen, and R. Serimaa. X-ray characterization of starch-based solid foams. *Journal of Materials Science*, 46:3470–3479, 2011. DOI: [10.1007/s10853-011-5252-y](https://doi.org/10.1007/s10853-011-5252-y).
- [49] K. Leppänen, I. Bjurhager, M. Peura, A. Kallonen, J.-P. Suuronen, P. Penttilä, J. Love, K. Fagerstedt, and R. Serimaa. X-ray scattering and microtomography study on the structural changes of never-dried silver birch, european aspen and hybrid aspen during drying. *Holzforschung*, 65:865–873, Jul 2011. DOI: [10.1515/HF.2011.108](https://doi.org/10.1515/HF.2011.108).
- [50] J.-P. Suuronen, A. Kallonen, M. Eik, J. Puttonen, R. Serimaa, and H. Herrmann. Analysis of short fibres orientation in steel fibre-reinforced concrete (SFRC) by X-ray tomography. *Journal of Materials Science*, 48:1358–1367, 2013. DOI: [10.1007/s10853-012-6882-4](https://doi.org/10.1007/s10853-012-6882-4).
- [51] P. Stähli, R. Custer, and J. van Mier. On flow properties, fibre distribution, fibre orientation and flexural behaviour of FRC. *Materials and Structures*, 41: 189–196, 2008. DOI: [10.1617/s11527-007-9229-x](https://doi.org/10.1617/s11527-007-9229-x).

- [52] M. D. Abràmoff, P. J. Magalhães, and S. J. Ram. Image Processing with ImageJ. *Biophotonics International*, 11(7):36–42, 2004.
- [53] T. Collins. Pseudo-flat field filter for ImageJ, 2004. URL <http://www.uhnresearch.ca/facilities/wcif/fdownload.html>.
- [54] EMC2 (Enhanced Machine controller). URL <http://www.linuxcnc.org/>. Software, <http://www.linuxcnc.org/>.
- [55] L.A. Feldkamp, L.C. Davis, and J.W. Kress. Practical cone-beam algorithm. *Journal of the Optical Society of America*, 1(6):612–619, 1984.
- [56] J. Weickert, B. M. Ter Haar Romeney, and M. A. Viergever. Efficient and reliable schemes for nonlinear diffusion filtering. *IEEE Transactions on Image Processing*, 7(3):398–410, 1998.
- [57] R Development Core Team. *R: A Language and Environment for Statistical Computing*. R Foundation for Statistical Computing, Vienna, Austria, 2011. URL <http://www.R-project.org>.
- [58] M. L. Delignette-Muller, R. Pouillot, J.-B. Denis, and C. Dutang. *fitdistrplus: help to fit of a parametric distribution to non-censored or censored data*, 2010. R package version 0.1-3.
- [59] W. N. Venables and B. D. Ripley. *Modern Applied Statistics with S*. Springer, New York, 4th edition, 2002. URL <http://www.stats.ox.ac.uk/pub/MASS4>.
- [60] A. G. Stephenson. evd: Extreme Value Distributions. *R News*, 2(2):31–32, June 2002. URL <http://CRAN.R-project.org/doc/Rnews/>.
- [61] R. Pouillot and M.-L. Delignette-Muller. Evaluating variability and uncertainty in microbial quantitative risk assessment using two R packages. *International Journal of Food Microbiology*, 142(3):330–40, 2010. DOI: [10.1016/j.ijfoodmicro.2010.07.011](https://doi.org/10.1016/j.ijfoodmicro.2010.07.011).
- [62] D. Adler and D. Murdoch. *rgl: 3D visualization device system (OpenGL)*, 2010. URL <http://CRAN.R-project.org/package=rgl>. R package version 0.91.
- [63] D. Wuertz, many others, and see the SOURCE file. *fMultivar: Multivariate Market Analysis*, 2009. URL <http://CRAN.R-project.org/package=fMultivar>. R package version 2100.76.
- [64] E. Dimitriadou, K. Hornik, F. Leisch, D. Meyer, and A. Weingessel. *e1071: Misc Functions of the Department of Statistics (e1071), TU Wien*, 2011. URL <http://CRAN.R-project.org/package=e1071>. R package version 1.5-25.
- [65] P. Poncet. *modeest: Mode Estimation*, 2010. URL <http://CRAN.R-project.org/package=modeest>. R package version 1.14.
- [66] G. Casella and J. O. Berger. *Statistical Inference*. Duxbury Press, 2nd edition, 2001.
- [67] A. J. M. Spencer. *Continuum mechanics*. Dover Pubns, 1980.
- [68] C. Truesdell and W. Noll. *The Non-Linear Field Theories of Mechanics, Encyclopedia of Physics*. Springer-Verlag, 1965.
- [69] M. Itskov. *Tensor Algebra and Tensor Analysis for Engineers With Applications to Continuum Mechanics*. Springer, 2009.

- [70] M. Itskov and N. Aksel. A class of orthotropic and transversely isotropic hyperelastic constitutive models based on a polyconvex strain energy function. *International Journal of Solids and Structures*, 41(14):3833 – 3848, 2004. DOI: [10.1016/j.ijsolstr.2004.02.027](https://doi.org/10.1016/j.ijsolstr.2004.02.027).
- [71] A.J.M. Spencer and R.S. Rivlin. Isotropic integrity bases for vectors and second-order tensors. *Archive for Rational Mechanics and Analysis*, 9(1):45–63, 1962. ISSN 0003-9527. DOI: <http://dx.doi.org/10.1007/BF00253332>.
- [72] P. P. Teodorescu and N. A. Nicorovici. *Applications of the theory of groups in mechanics and physics*, volume 140 of *Fundamental Theories of Physics*. Springer Netherlands, 2004. DOI: <http://dx.doi.org/10.1007/978-1-4020-2047-6>.
- [73] H. Herrmann and M. Eik. Some comments on the theory of short fibre reinforced material. *Proceedings of the Estonian Academy of Sciences*, 60(3):179–183, 2011. DOI: [10.3176/proc.2011.3.06](https://doi.org/10.3176/proc.2011.3.06).
- [74] R. Eppenga and D. Frenke. Monte Carlo study of the isotropic and nematic phases of infinitely thin hard platelets. *Molecular Physics*, 52:1303–1334, 1984.
- [75] H. Steuer. *Thermodynamical Properties Of A Model Liquid Crystal*. PhD thesis, TU Berlin, 2004. URL <http://opus.kobv.de/tuberlin/volltexte/2004/919/>.
- [76] I. Pardowitz and S. Hess. On the theory of irreversible processes in molecular liquids and liquid crystals, nonequilibrium phenomena associated with the second and fourth rank alignment tensors. *Physica A: Statistical Mechanics and its Applications*, 100(3):540 – 562, 1980. DOI: [10.1016/0378-4371\(80\)90166-1](https://doi.org/10.1016/0378-4371(80)90166-1).
- [77] T. J. Jankun-Kelly and K. Mehta. Superellipsoid-based, real symmetric traceless tensor glyphs motivated by nematic liquid crystal alignment visualization. In *IEEE Transactions on Visualization and Computer Graphics (Proceedings Visualization/Information Visualization 2006)*, pages 1197–1204, 2006. DOI: [10.1109/TVCG.2006.181](https://doi.org/10.1109/TVCG.2006.181).
- [78] H. A. Meier, P. Steinmann, and E. Kuhl. Towards multiscale computation of confined granular media: Contact Forces, Stresses and Tangent Operators. *Technische Mechanik*, 28:32–42, 2008. URL http://www.ovgu.de/ifme/zeitschrift_tm/2008_Heft1/04_Meier_Steinmann.pdf.
- [79] B. Klusemann and B. Svendsen. Homogenization methods for multi-phase elastic composites: Comparisons and benchmarks. *Technische Mechanik*, 30:374–386, 2010. URL http://www.ovgu.de/ifme/zeitschrift_tm/2010_Heft4/07_Klusemann.html.
- [80] L.C. Brinson and W.S. Lin. Comparison of micromechanics methods for effective properties of multiphase viscoelastic composites. *Composite Structures*, 41(3–4):353 – 367, 1998. ISSN 0263-8223. DOI: [http://dx.doi.org/10.1016/S0263-8223\(98\)00019-1](http://dx.doi.org/10.1016/S0263-8223(98)00019-1).
- [81] European Committee for Standardization. EN 1992-1-1 Eurocode 2: Design of concrete structures - Part 1-1: General rules and rules for buildings. Brussels, 2005. EN, CEN.
- [82] F. Larsson, R. Lillbacka, and K. Runesson. On the adaptive use of the Taylor assumption in computational homogenization of thin metal sheets. *International*

- Journal of Material Forming*, 2(1):903–906, 2009. DOI: [10.1007/s12289-009-0632-4](https://doi.org/10.1007/s12289-009-0632-4).
- [83] S. Mercier, A. Molinari, S. Berbenni, and M. Berveiller. Comparison of different homogenization approaches for elastic–viscoplastic materials. *Modelling and Simulation in Materials Science and Engineering*, 20(2):1–22, 2012. DOI: <http://dx.doi.org/10.1088/0965-0393/20/2/024004>.
- [84] GE Measurement & Control. phoenix|x-ray v|tome|x l 450, 2013. URL <http://www.ge-mcs.com/en/radiography-x-ray/ct-computed-tomography.html>. (page visited Oct. 15th 2013).
- [85] YXLON International. Y.CT Compact, 2013. URL <http://www.yxlon.com/Products/CT-systems/Y-CT-Compact>. (page visited Oct. 15th 2013).
- [86] V.V Zhuk and G.I Natanson. Тригонометрические ряды Фурье и элементы теории аппроксимации: учебное пособие (*Trigonometric Fourier series and the elements of the theory of approximation*). Издательство Ленинградского Университета (Leningrad University Publishing), 1983. URL <http://books.google.ee/books?id=K1TvAAAAAAAJ>.

A. Appendicies

A.1 Orientation distribution function as a spherical harmonic function

Let us consider H_l to be $(2l + 1)$ dimensional Hilbert subspace (vector space) spanned by all spherical harmonics of rank l . Then for $l \in \mathbb{N}$:

$$H_l = \text{span}_{(\mu_1 \dots \mu_l) \in \{1,2,3\}^l} h_{\mu_1 \dots \mu_l}^{(l)}, \quad (\text{A.1.1})$$

where $h_{\mu_1 \dots \mu_l}^{(l)}$ is a spherical harmonic function. The Hilbert space H of square-integrable functions L^2 can be represented as a direct sum of finite dimensional subspaces H_l , such as:

$$H = \bigoplus_{l=0}^{\infty} H_l, \quad H \in L^2. \quad (\text{A.1.2})$$

The orientation distribution function $f(\mathbf{n})$, where $\mathbf{n} \in (\theta, \phi)$ is a unit vector, belongs to L^2 .

Applying the Laplace operator on \mathbb{R}^3 , i.e. $\Delta = \left(\frac{\partial^2}{\partial x_1^2} + \frac{\partial^2}{\partial x_2^2} + \frac{\partial^2}{\partial x_3^2} \right)$, on symmetric irreducible (symmetric traceless) tensors, $\overline{n_{\mu_1} \dots n_{\mu_l}}$, where a unit vector n_{μ} (radius $r = 1$) can be presented in Cartesian coordinates as $n(\theta, \phi) = \hat{n}(x = \sin \theta \cos \phi, y = \sin \theta \sin \phi, z = \cos \theta)$, the following can be received:

$$\Delta \overline{\hat{n}_{\mu_1} \dots \hat{n}_{\mu_l}} = 0, \quad (\text{A.1.3})$$

which explains $\overline{n_{\mu_1} \dots n_{\mu_l}}$ to be a harmonic function [30]. Applying the Laplace-Beltrami operator, which reads as:

$$\Delta_S = \frac{1}{\sin \theta} \cdot \frac{\partial}{\partial \theta} \left(\sin \theta \cdot \frac{\partial}{\partial \theta} \right) + \frac{1}{\sin^2 \theta} \cdot \frac{\partial^2}{\partial \phi^2}, \quad (\text{A.1.4})$$

the following can be received:

$$\Delta_S \overline{n_{\mu_1} \dots n_{\mu_l}} = -l(l+1) \overline{n_{\mu_1} \dots n_{\mu_l}}, \quad (\text{A.1.5})$$

which shows that the coordinate functions $\overline{n_{\mu_1} \cdots n_{\mu_l}}$ are the eigenfunctions of the Laplace-Beltrami operator corresponding to eigenvalues $\lambda_l = -l(l+1)$. The eigenfunctions of Laplace-Beltrami operator are called spherical harmonics, which represent the angular portion of a set of orthogonal solutions of the Laplace equation written in spherical coordinates. The eigenfunction with the corresponding eigenvalue $\lambda_l \geq 0$ satisfies:

$$\Delta_S \overline{n_{\mu_1} \cdots n_{\mu_l}} + \lambda_l \overline{n_{\mu_1} \cdots n_{\mu_l}} = 0 . \quad (\text{A.1.6})$$

Accordingly, the symmetric irreducible tensors $\overline{n_{\mu_1} \cdots n_{\mu_l}}$ are spherical harmonic functions [30]:

$$h_{\mu_1 \dots \mu_l}^{(l)}(\mathbf{n}) := \overline{n_{\mu_1} \cdots n_{\mu_l}} . \quad (\text{A.1.7})$$

Any spherical harmonic function of rank l , $Y_l(\theta, \phi)$, can be represented as a linear combination of $(2l+1)$, Eq. (A.1.5), main spherical functions each depending on either *sines* or *cosines* of the angles θ and ϕ [37]. The main spherical functions may have the following form:

$$\begin{aligned} P_l^{(0)}(\cos \theta), P_l^{(1)}(\cos \theta) \cdot \cos \phi, P_l^{(2)}(\cos \theta) \cdot \cos 2\phi, \dots, P_l^{(l)}(\cos \theta) \cdot \cos l\phi, \\ P_l^{(1)}(\cos \theta) \sin \phi, P_l^{(2)}(\cos \theta) \cdot \sin 2\phi, \dots, P_l^{(l)}(\cos \theta) \cdot \sin l\phi, \end{aligned}$$

where $P_l^{(k)}$ is an l -th rank polynomial of $\cos \theta$ or an $(l-1)$ -th rank polynomial of $\cos \theta$ times $\sin \theta$. Accordingly, any arbitrary l -th rank spherical harmonic function can be represented as follows:

$$Y_l(\theta, \phi) = \sum_{k=0}^l P_l^{(k)}(\cos \theta) [c_l^k \cdot \cos k\phi + s_l^k \cdot \sin k\phi] = \sum_{m=0}^{2l} a_l^m Y_l^m(\theta, \phi), \quad (\text{A.1.8})$$

where c_l^k, s_l^k are $(2l+1)$ arbitrary constants, $P_l^{(k)}(\cos \theta)$ are: if $k=0$, the Legendre polynomials and if $k=1, 2, \dots, l$ the associated Legendre polynomials. The index l is the rank of the main spherical function $Y_l^m(\theta, \phi)$ and the index m is an auxiliary and indicates the order [37]. The index m has the following values:

$$\begin{aligned} \text{if } m \leq l, \quad Y_l^m(\theta, \phi) &= P_l^{(k)}(\cos \theta) \cdot \cos k\phi, \quad a_l^m = c_l^k, \quad k = m \quad (\text{A.1.9}) \\ \text{if } m > l, \quad Y_l^m(\theta, \phi) &= P_l^{(k)}(\cos \theta) \cdot \sin k\phi, \quad a_l^m = s_l^k, \quad k = m - l . \end{aligned}$$

The Legendre and the associated Legendre polynomials can be determined using the following recursive formulas, respectively:

$$P_l(\cos \theta) = \frac{2l-1}{l} \cdot \cos \theta \cdot P_{l-1}(\cos \theta) - \frac{l-1}{l} P_{l-2}(\cos \theta) , \quad (\text{A.1.10})$$

$$\text{wherein } P_l(0) = \begin{cases} 0, & \text{if } l \text{ is odd} \\ \frac{l!(-1)^{l/2}}{(\frac{l}{2}!)^2 \cdot 2^{l/2}}, & \text{if } l \text{ is even} \end{cases} \quad (\text{A.1.11})$$

$$\begin{aligned}
 P_l^{(k)}(\cos \theta) &= \frac{2l-1}{l-k} \cdot \cos \theta \cdot P_{l-1}^{(k)}(\cos \theta) - \frac{l+k-1}{l-k} \cdot P_{l-2}^{(k)}(\cos \theta) , \\
 0 \leq k \leq l-2, \quad l \geq 2 .
 \end{aligned} \tag{A.1.12}$$

The Legendre and the associated Legendre polynomials form an orthogonal system on the interval $[-1, 1]$.

The spherical harmonics belong to square-integrable functions L^2 and form an orthogonal basis on L^2 . For the completeness of the basis it is necessary and sufficient that the number of basis vectors coincide with the dimension of the functional space. On a unit sphere S^2 the Legendre and the associated Legendre polynomials form a complete orthonormal basis. Consequently, the same holds true for the tensor family $\{\overline{n_{\mu_1} \cdots n_{\mu_l}}\}$. On a unit sphere any square-integrable function $g \in L^2$ can be expanded as a series of main spherical harmonics in complete orthonormal basis, such as:

$$g(\theta, \phi) = \sum_{l=0}^{\infty} Y_l(\theta, \phi) = \sum_{l=0}^{\infty} \sum_{m=0}^{2l} a_l^m Y_l^m(\theta, \phi) , \tag{A.1.13}$$

where a_l^m are acting as expansion coefficients [37], such as:

$$a_l^m = \frac{\langle g, Y_l^m \rangle}{\|Y_l^m\|^2} = \tag{A.1.14}$$

$$\begin{cases}
 m \leq l, \quad k = m \\
 c_l^k = \frac{(2l+1)}{2\pi \cdot \delta_k} \cdot \frac{(l-k)!}{(l+k)!} \cdot \int_0^{2\pi} \int_0^\pi g(\theta, \phi) \cdot \underbrace{P_l^{(k)}(\cos \theta) \cos k\phi}_{Y_l^m} \cdot \underbrace{\sin \theta \cdot d\phi d\theta}_{d\Omega} , \\
 m > l, \quad k = l - m \\
 s_l^k = \frac{(2l+1)}{2\pi \cdot \delta_k} \cdot \frac{(l-k)!}{(l+k)!} \cdot \int_0^{2\pi} \int_0^\pi g(\theta, \phi) \cdot \underbrace{P_l^{(k)}(\cos \theta) \sin k\phi}_{Y_l^m} \cdot \underbrace{\sin \theta \cdot d\phi d\theta}_{d\Omega} ,
 \end{cases}$$

where $\delta_k = 1$, if $k > 0$, if $k = 0$, $\delta_0 = 2$,

$\sin \theta \cdot d\phi d\theta = d\Omega$.

$\langle g, Y_l^m \rangle$ in Eq. (A.1.14) means a scalar multiplication defined for any two arbitrary functions p and q on L^2 as:

$$\langle p, q \rangle = \int_a^b p(x)q(x)dx , \tag{A.1.15}$$

$\|Y_l^m\|^2$ is a square norm of a function and $d\Omega$ comes from the integration over a flat rectangular area $[0, \pi; 0, 2\pi]$ instead of a surface integral \oint_{S^2} on a unit sphere. If in some complete basis system the expansion coefficients a_l^m in Eq. (A.1.13) are known then the function $g(\theta, \phi)$ can be also considered as known and the following identity holds true:

$$\sum_{l=0}^{\infty} \sum_{m=0}^{2l} (\bar{a}_l^m)^2 = \frac{1}{4\pi} \int_{\Omega} g^2(\theta, \phi) d\Omega , \tag{A.1.16}$$

where \bar{a}_l^m is the normalized expansion coefficient:

$$\begin{aligned}\bar{a}_l^m &= \sqrt{\frac{\delta_k}{2 \cdot (2l+1)} \cdot \frac{(l+k)!}{(l-k)!}} \cdot a_l^m \\ &= \frac{1}{4\pi} \int_0^{2\pi} \int_0^\pi g(\theta, \phi) \cdot \bar{Y}_l^m \cdot \sin \theta \cdot d\phi d\theta.\end{aligned}\quad (\text{A.1.17})$$

The normalization of Y_l^m reads as:

$$\bar{Y}_l^m(\theta, \phi) = \sqrt{\frac{2 \cdot (2l+1)}{\delta_k} \cdot \frac{(l-k)!}{(l+k)!}} \cdot Y_l^m(\theta, \phi). \quad (\text{A.1.18})$$

The identity Eq. (A.1.16) is called the Parseval's identity. In terms of completely normalized functions Eqs. (A.1.17), (A.1.18), the Eq. (A.1.13) has the following form:

$$g(\theta, \phi) = \sum_{l=0}^{\infty} \bar{Y}_l(\theta, \phi) = \sum_{l=0}^{\infty} \sum_{m=0}^{2l} \bar{a}_l^m \bar{Y}_l^m(\theta, \phi). \quad (\text{A.1.19})$$

The spherical harmonic function of rank l , $Y_l(\theta, \phi)$, in decomposition presented in Eq. (A.1.13) represent the sum of $(l+1)$ terms, which differ from each other by the value of k . Each term having the form as:

$$P_l^{(k)}(\cos \theta) [c_l^k \cdot \cos k\phi + s_l^k \cdot \sin k\phi], \quad k = 1, 2, 3, \dots, l \quad (\text{A.1.20})$$

can be considered, similar to the harmonic analysis of one argument function employing the Fourier series, as the l -th harmonic of the original function. If $l = 0$, then:

$$\bar{Y}_0^{(0)}(\theta, \phi) = Y_0^{(0)}(\theta, \phi) \equiv 1 \quad \text{and} \quad (\text{A.1.21})$$

$$\bar{a}_{00} = a_{00} = c_{00} = \frac{1}{4\pi} \int_{\Omega} g(\theta, \phi) d\Omega = \hat{g}, \quad (\text{A.1.22})$$

meaning that the zero harmonic in Eq. (A.1.13) is a constant, which is equal to the mean integral value \hat{g} of the original function $g(\theta, \phi)$ on a sphere. All other harmonics starting from $l = 1$ approximate the deviation $(g - \hat{g})$ of the original function $g(\theta, \phi)$ from its mean value. The series presented in Eq. (A.1.13) are also called Laplace series for the function $g(\theta, \phi)$ and the expansion terms in Eqs. (A.1.13), (A.1.14) are Laplace spherical harmonics. Hence, while decomposing the given function on a unit sphere, $g(\theta, \phi)$, $g \in S^2$, by spherical harmonics, the series terms are always Laplace spherical functions. The values of the coefficients in Eq. (A.1.14) are determined under the least squares method assuming the condition of a minimum squared error σ_n^2 , such as:

$$\sigma_n^2 = \int_{\Omega} g^2(\theta, \phi) d\Omega - \sum_{l=0}^n \sum_{m=0}^{2l} \frac{2\pi \cdot \delta_k (l+k)!}{(2l+1)(l-k)!} \cdot (a_l^m)^2. \quad (\text{A.1.23})$$

The infinite Laplace series $l \rightarrow \infty$ converges to the original function absolutely and uniformly and thus the same holds for Eq. (A.1.23) meaning that if $n \rightarrow \infty$ then $\sigma_n^2 \rightarrow 0$ and Eq. (A.1.23) takes the form of the Parseval's identity Eq. (A.1.16). Accordingly, the sum of the squares of all the coefficients of the expansion is closely related to the mean square of the given function on a sphere. The approximation employing the coefficients defined considering a minimum squared error provides a good accuracy within the sum of the first terms of the Laplace series [37].

Spherical harmonics expansion is the modification of the Fourier series decomposing any original function g by an orthogonal basis into the linear combination (sum) of harmonic oscillations with different frequencies. The classical trigonometric Fourier series for the real valued function $g(x)$ integrable on an interval $(x_0, x_0 + T)$, $x_0, T \in \mathbb{R}$ and periodic with a period T outside the interval, for the integers $\mathbb{N} \geq 0$ and $T = 2\pi$ reads as follows:

$$g(x) = \frac{m_0}{2} + \sum_{k=1}^{\mathbb{N}} \left(m_k \cos \frac{2\pi kx}{T} + b_k \sin \frac{2\pi kx}{T} \right), \quad (\text{A.1.24})$$

where m_0, m_k, b_k , $k = 1, 2 \dots$ are called the Fourier coefficients of the function g [86].

Let us consider now a function $f(\mathbf{n})$, where \mathbf{n} defines a unit vector on a two-dimensional unit sphere S^2 , to be square-integrable, such as: $f(\mathbf{n}) \in L^2(S^2, \mathbb{R})$. According to Eqs. (A.1.3) and (A.1.5) the symmetric irreducible tensors $\overline{n_{\mu_1} \dots n_{\mu_l}}$ are spherical harmonic functions and they form a complete orthonormal basis, since based on Eqs. (A.1.10), (A.1.12) the main spherical harmonics are either Legendre or associated Legendre polynomials. Following Eq. (A.1.21), if $l = 0$ the zero harmonic $Y_0^{(0)}$ can be set to be equal to 1. Consequently, the following representation of $f(\mathbf{n})$ can be obtained:

$$f(\mathbf{n}) = \alpha_0 \cdot 1 + \sum_{l=1}^{\infty} (2l-1)! \alpha_{\mu_1 \dots \mu_l} \overline{n_{\mu_1} \dots n_{\mu_l}}, \quad (\text{A.1.25})$$

where α_0 and $\alpha_{\mu_1 \dots \mu_l}$ are expansion coefficients which read as, see also Eqs. (A.1.19), (A.1.22):

$$\alpha_0 = \frac{1}{4\pi} \oint_{S^2} f(\mathbf{n}) \cdot 1 \cdot d^2n, \quad (\text{A.1.26})$$

$$\alpha_{\mu_1 \dots \mu_l} = \frac{1}{4\pi} \frac{(2l+1)}{l!} \oint_{S^2} f(\mathbf{n}) \cdot \overline{n_{\mu_1} \dots n_{\mu_l}} d^2n, \quad (\text{A.1.27})$$

where $\mathbf{n} \in (\theta, \phi)$, $\theta \in [0^\circ, 180^\circ]$; $\phi \in [0^\circ, 360^\circ]$ are the parameters of a current point on a sphere. Thereby, Eq. (A.1.25) is the decomposition of a function

$f(\mathbf{n})$ by an orthonormal system formed by the symmetric irreducible tensors $\overline{n_{\mu_1} \cdots n_{\mu_l}}$, and the expansion coefficients $\alpha_0, \alpha_{\mu_1 \dots \mu_l}$ in complete basis of $\overline{n_{\mu_1} \cdots n_{\mu_l}}$, according to Eq. (A.1.16), can be used to uniquely reconstruct the original function $f(\mathbf{n})$.

A.2 Density distribution of the inclination angle θ

The results of the bootstrap Kolmogorov-Smirnov tests applied on the density distributions of the inclination angle θ received employing the photos of slice surfaces are presented in Tables A.2.1, A.2.2, A.2.3, A.2.4, A.2.5.

Table A.2.1. Results of the two-sample bootstrap Kolmogorov-Smirnov test (function `ks.boot` from [2]) applied on the density distribution of the inclination angle θ in the slab 2. Reduced cuboid refer to the cuboid, where only every fourth slice surface is taken into account.

	Cuboid 2.1 (side of a slab)				Cuboid 2.2 (centre of a slab)			
Inclination angle θ								
	whole cuboid		reduced cuboid		whole cuboid		reduced cuboid	
Distribution	D	p -value	D	p -value	D	p -value	D	p -value
Gaussian	0.104	e-16	0.100	e-16	0.077	e-16	0.066	4.5e-07
Gamma	0.041	e-11	0.051	5.0e-06	0.058	e-16	0.055	5.7e-05
Gumbel	0.038	e-09	0.043	0.0002	0.041	e-09	0.042	0.0041
Weibull	0.088	e-16	0.081	e-14	0.067	e-16	0.060	6.6e-06
Log-normal	0.038	e-09	0.036	0.0031	0.058	e-16	0.055	5.5e-05

Table A.2.2. Results of the two-sample bootstrap Kolmogorov-Smirnov test (function `ks.boot` from [2]) applied on the density distribution of the inclination angle θ in the slab 3. Reduced cuboid refer to the cuboid, where only every fourth slice surface is taken into account.

	Cuboid 3.1 (side of a slab)				Cuboid 3.2 (centre of a slab)			
Inclination angle θ								
	whole cuboid		reduced cuboid		whole cuboid		reduced cuboid	
Distribution	D	p -value	D	p -value	D	p -value	D	p -value
Gaussian	0.099	e-16	0.108	e-16	0.067	e-16	0.072	e-08
Gamma	0.040	e-09	0.048	6.4e-05	0.057	e-16	0.049	0.0003
Gumbel	0.038	e-08	0.045	0.0002	0.042	e-09	0.042	0.0030
Weibull	0.087	e-16	0.079	e-12	0.061	e-16	0.069	e-08
Log-normal	0.035	2.6e-07	0.039	0.0025	0.053	e-14	0.056	2.4e-05

Table A.2.3. Results of the two-sample bootstrap Kolmogorov-Smirnov test (function `ks.boot` from [2]) applied on the density distribution of the inclination angle θ in the slab 4. Reduced cuboid refer to the cuboid, where only every fourth slice surface is taken into account.

	Cuboid 4.1 (side of a slab)				Cuboid 4.2 (centre of a slab)			
Inclination angle θ								
	whole cuboid		reduced cuboid		whole cuboid		reduced cuboid	
Distribution	D	p -value	D	p -value	D	p -value	D	p -value
Gaussian	0.085	e-16	0.087	e-13	0.068	e-16	0.082	e-10
Gamma	0.035	1.0e-06	0.032	0.0381	0.054	e-14	0.058	4.1e-05
Gumbel	0.031	2.4e-05	0.025	0.1713	0.044	e-09	0.045	0.003
Weibull	0.075	e-16	0.070	e-08	0.061	e-16	0.071	2.3e-07
Log-normal	0.025	0.001	0.031	0.05177	0.057	e-15	0.06	1.8e-05

Table A.2.4. Results of the two-sample bootstrap Kolmogorov-Smirnov test (function `ks.boot` from [2]) applied on the density distribution of the inclination angle θ in the slab 5. Reduced cuboid refer to the cuboid, where only every fourth slice surface is taken into account.

	Cuboid 5.1(side of a slab)				Cuboid 5.2(centre of a slab)			
Inclination angle θ								
	whole cuboid		reduced cuboid		whole cuboid		reduced cuboid	
Distribution	D	<i>p</i> -value	D	<i>p</i> -value	D	<i>p</i> -value	D	<i>p</i> -value
Gaussian	0.110	e-16	0.117	e-16	0.078	e-16	0.094	e-15
Gamma	0.052	e-15	0.058	e-06	0.046	e-11	0.044	0.0009
Gumbel	0.047	e-12	0.056	2.9e-06	0.031	1.6e-05	0.036	0.0103
Weibull	0.093	e-16	0.099	e-16	0.060	e-16	0.068	e-08
Log-normal	0.040	e-09	0.046	0.0002	0.046	e-11	0.048	0.0002

Table A.2.5. Results of the two-sample bootstrap Kolmogorov-Smirnov test (function `ks.boot` from [2]) applied on the density distribution of the inclination angle θ in the slab 6. Reduced cuboid refer to the cuboid, where only every fourth slice surface is taken into account.

	Cuboid 6.1(side of a slab)				Cuboid 6.2(centre of a slab)			
Inclination angle θ								
	whole cuboid		reduced cuboid		whole cuboid		reduced cuboid	
Distribution	D	<i>p</i> -value	D	<i>p</i> -value	D	<i>p</i> -value	D	<i>p</i> -value
Gaussian	0.096	e-16	0.095	e-15	0.082	e-16	0.081	4.3e-07
Gamma	0.037	2.8e-07	0.037	0.013	0.065	e-15	0.073	8.9e-06
Gumbel	0.036	4.7e-07	0.035	0.019	0.053	e-10	0.062	0.0003
Weibull	0.075	e-16	0.075	e-09	0.072	e-16	0.068	4.9e-05
Log-normal	0.031	2.7e-05	0.043	0.002	0.065	e-15	0.074	7.0e-06

A.3 Variations of fibre orientation distributions along the X - and Y -axes of the slabs

Figs. A.3.1, A.3.2 present the variations of fibre orientation distributions along the height of the whole (i.e. top, middle and bottom parts) cylinder samples 1B, 4A and 4B. The statistical data presented allow to observe the orientation of fibres in the compression (top) and tension (bottom) zones of the tested slabs.

Figs. A.3.3, A.3.4 demonstrate the variations of fibre orientation distributions in the side and centre cylinders.

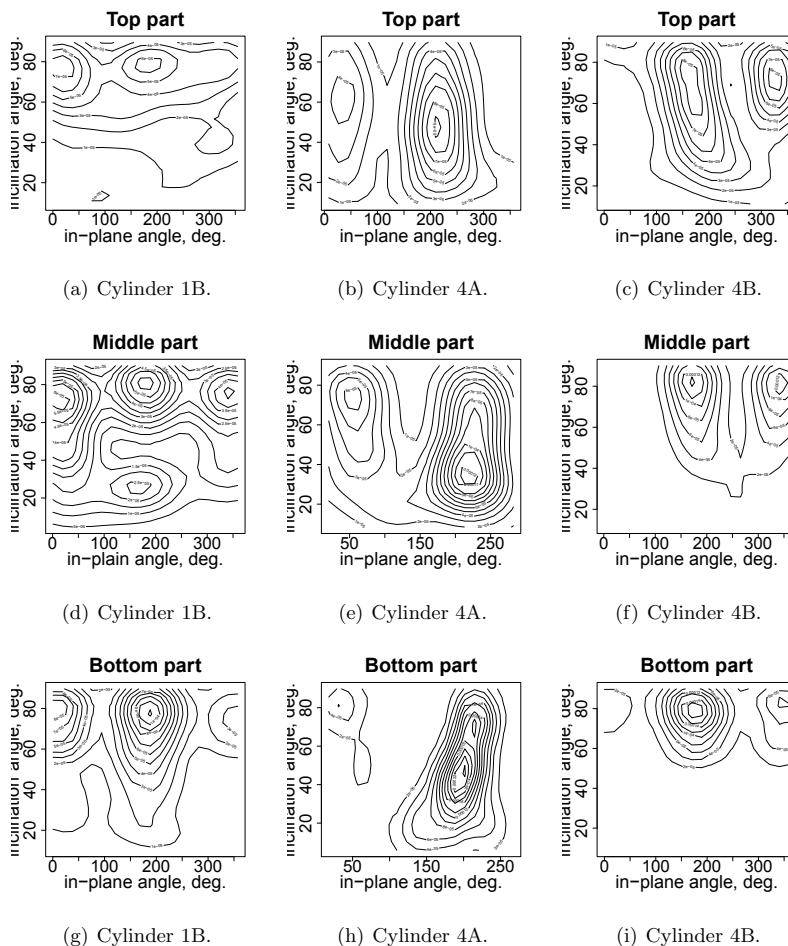
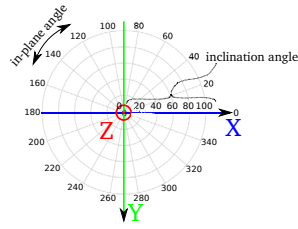
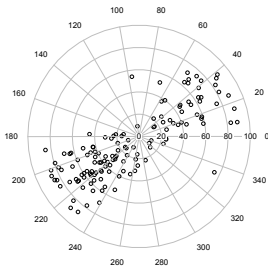


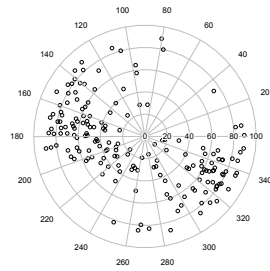
Figure A.3.1. Variations in bivariate densities of the inclination angle θ and in-plane angle ϕ measured by μ CT between the side (“Cylinder *.A”) and centre (“Cylinder *.B”), and along the height of the whole cylinder samples.



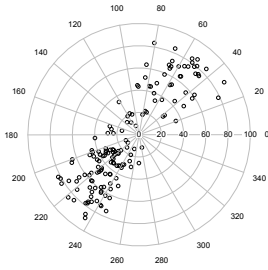
(a) Orientation.



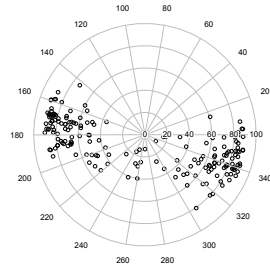
(b) **Top part.** Cylinder 4A.



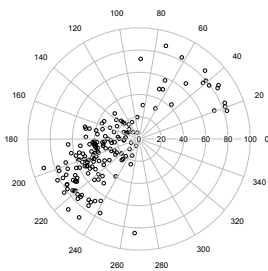
(c) Cylinder 4B.



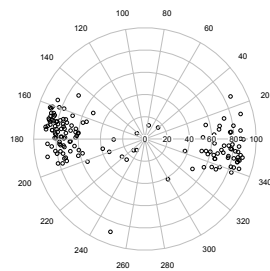
(d) **Middle part.** Cylinder 4A.



(e) Cylinder 4B.

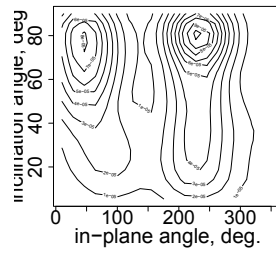


(f) **Bottom part.** Cylinder 4A.

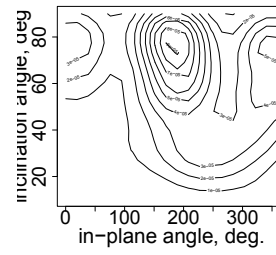


(g) Cylinder 4B.

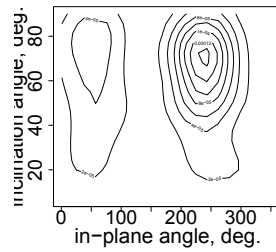
Figure A.3.2. Scatter plots of fibre orientation variations measured by μ CT between the side ("Cylinder *.A") and centre ("Cylinder *.B"), and along the height of the whole cylinder samples. In (a) the radius represents the inclination angle θ and in-plane angle ϕ is on circumference. Z-axis corresponds to the direction of the tensile stress in a slab, Fig. 2.4.



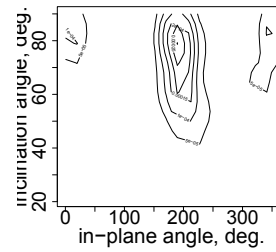
(a) Cylinder 2A.



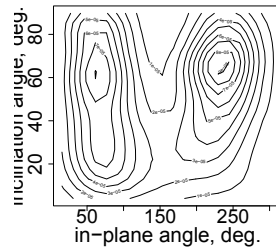
(b) Cylinder 2B.



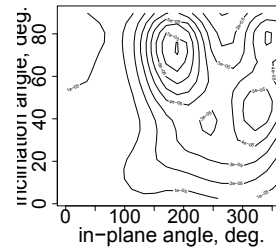
(c) Cylinder 3A.



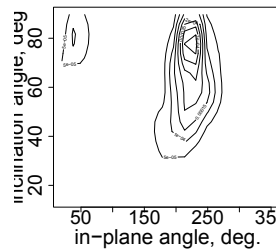
(d) Cylinder 3B.



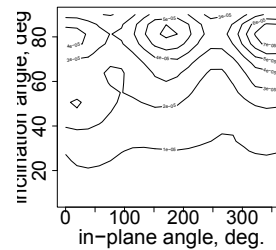
(e) Cylinder 5A.



(f) Cylinder 5B.



(g) Cylinder 6A.



(h) Cylinder 6B.

Figure A.3.3. Variations in bivariate densities of the inclination angle θ and in-plane angle ϕ measured by μ CT between the side ("Cylinder *.A") and centre ("Cylinder *.B") cylinder samples.

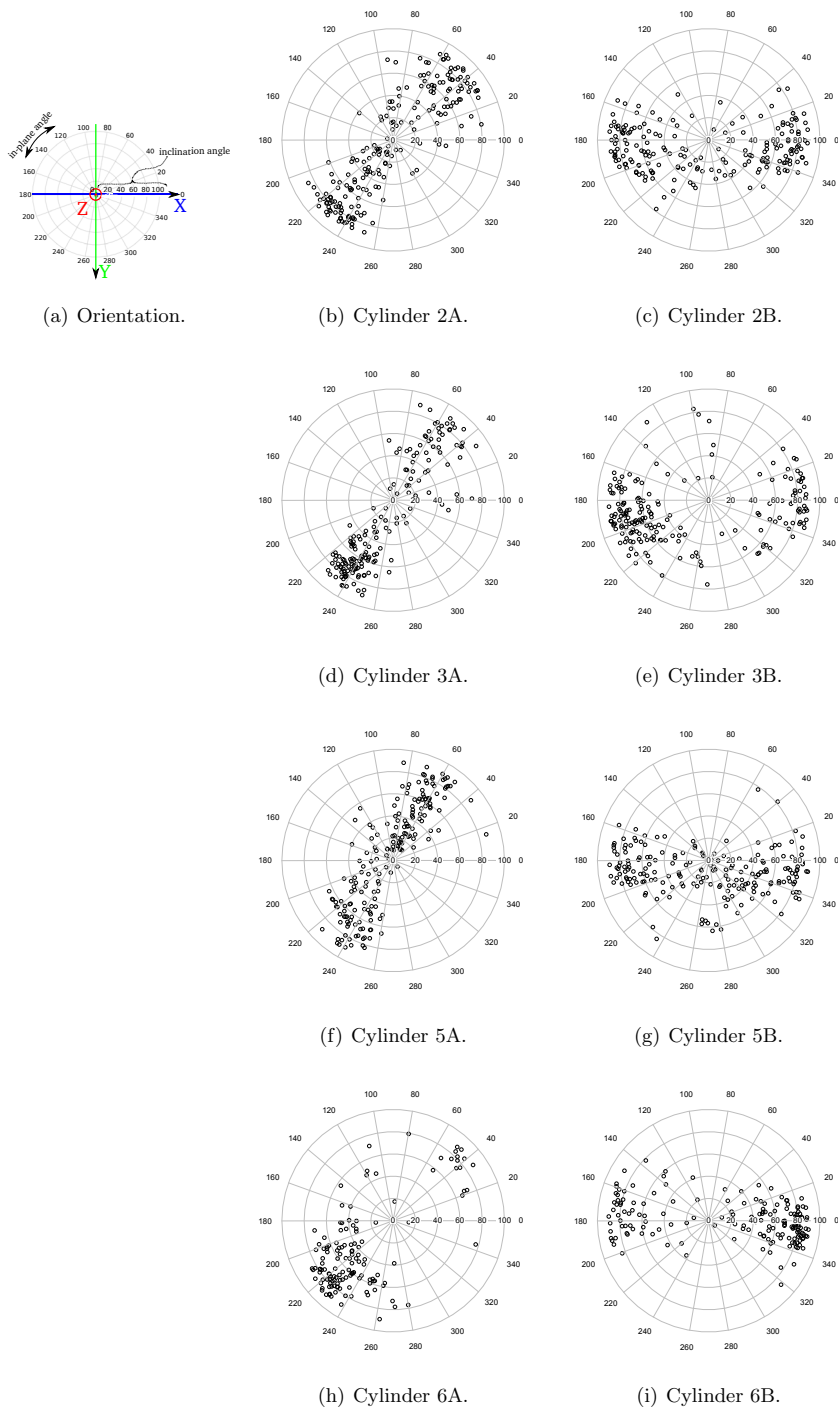


Figure A.3.4. Scatter plots of fibre orientation variations measured by μ CT between the side ("Cylinder *.A") and centre ("Cylinder *.B") cylinder samples. In (a) the radius represents the inclination angle θ and in-plane angle ϕ is on circumference. Z-axis corresponds to the direction of the tensile stress in a slab, Fig. 2.4.

A.4 Measured fibre alignments characterized by the eigenvectors of the 2^{nd} order alignment tensor in the tested slabs

Tables A.4.1, A.4.2 and A.4.3 present fibre orientation distribution characteristics for the top, middle and bottom parts of the cylinder samples scanned by μ CT, respectively. The orientation characteristics include the scalar-order parameter S and triplet of the eigenvectors $\mathbf{d}^1, \mathbf{d}^2, \mathbf{d}^3$ from the 2^{nd} order alignment tensor in the spherical coordinate system. $S = 1$ corresponds to the transversely isotropic material symmetry, $S = 0$ to isotropy and $S = -\frac{1}{2}$ describes the plane isotropic case. The biaxiality b_S shows the non-symmetry of the distribution with respect to \mathbf{d}^1 . Figs. A.4.1, A.4.2, A.4.3 demonstrate the location of the eigenvectors $\mathbf{d}^1, \mathbf{d}^2, \mathbf{d}^3$ in all measured cylinder samples. The location of the top, middle and bottom parts is given in Fig. 2.17(a).

Table A.4.1. Fibre orientation distribution characteristics for the top parts of the cylinder samples.

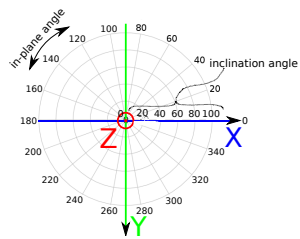
Cylinder nr.	S	b_S	$\mathbf{d}^1(\theta, \phi)$, deg	$\mathbf{d}^2(\theta, \phi)$, deg	$\mathbf{d}^3(\theta, \phi)$, deg
1A	0.49	0.13	53, 222	81, 126	38, 24
1B	0.33	0.009	82, 2	17, 119	75, 269
4A	-0.43	-0.11	87, 122	53, 215	37, 28
4B	0.35	0.11	78, 160	63, 64	30, 272

Table A.4.2. Fibre orientation distribution characteristics for the middle parts of the cylinder samples.

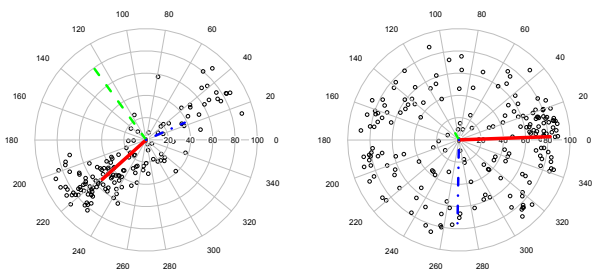
Cylinder nr.	S	b_S	$\mathbf{d}^1(\theta, \phi)$, deg	$\mathbf{d}^2(\theta, \phi)$, deg	$\mathbf{d}^3(\theta, \phi)$, deg
1A	0.52	0.11	28, 227	89, 136	62, 45
1B	0.53	0.09	74, 3	85, 271	17, 163
3A	0.52	0.12	76, 237	85, 145	15, 36
3B	0.59	0.05	79, 190	47, 89	45, 291
4A	-0.44	-0.13	81, 322	51, 224	41, 63
4B	0.62	0.09	89, 169	66, 78	24, 262
5A	-0.44	-0.05	80, 329	77, 61	17, 204
5B	-0.39	-0.06	73, 87	87, 356	18, 256
6A	0.65	0.03	68, 223	64, 324	36, 98
6B	0.63	0.08	81, 356	83, 265	12, 139

Table A.4.3. Fibre orientation distribution characteristics for the bottom parts of the cylinders.

Cylinder nr.	S	b_S	$\mathbf{d}^1(\theta, \phi)$,deg	$\mathbf{d}^2(\theta, \phi)$,deg	$\mathbf{d}^3(\theta, \phi)$,deg
1A	0.70	0.07	14, 52	90, 321	76, 231
1B	0.65	0.09	87, 185	87, 275	4, 57
4A	0.59	0.09	45, 203	73, 311	50, 56
4B	0.72	0.05	86, 175	80, 84	11, 287

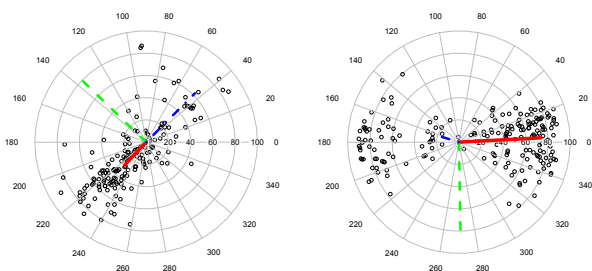


(a) Orientation.



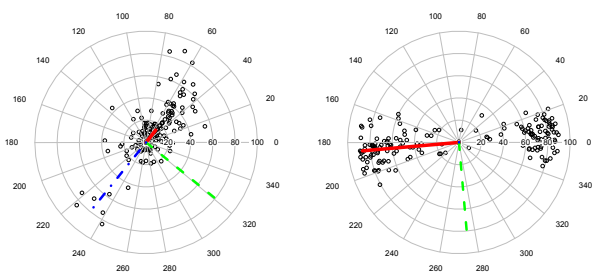
(b) **Top part.** Cylinder 1A.

(c) Cylinder 1B.



(d) **Middle part.** Cylinder 1A.

(e) Cylinder 1B.



(f) **Bottom part.** Cylinder 1A.

(g) Cylinder 1B.

Figure A.4.1. Fibre orientation distributions with the triplets of the eigenvectors \mathbf{d}^1 , \mathbf{d}^2 , \mathbf{d}^3 for the height of the whole cylinder samples 1A and 1B. \mathbf{d}^1 -solid red line, \mathbf{d}^2 -dashed green line, \mathbf{d}^3 -dot-dashed blue line. \mathbf{d}^1 is the director corresponding to according-to-amount-largest eigenvalue. In (a) the radius represents the inclination angle θ and in-plane angle ϕ is on circumference. Z-axis corresponds to the direction of the tensile stress in a slab, Fig. 2.4.

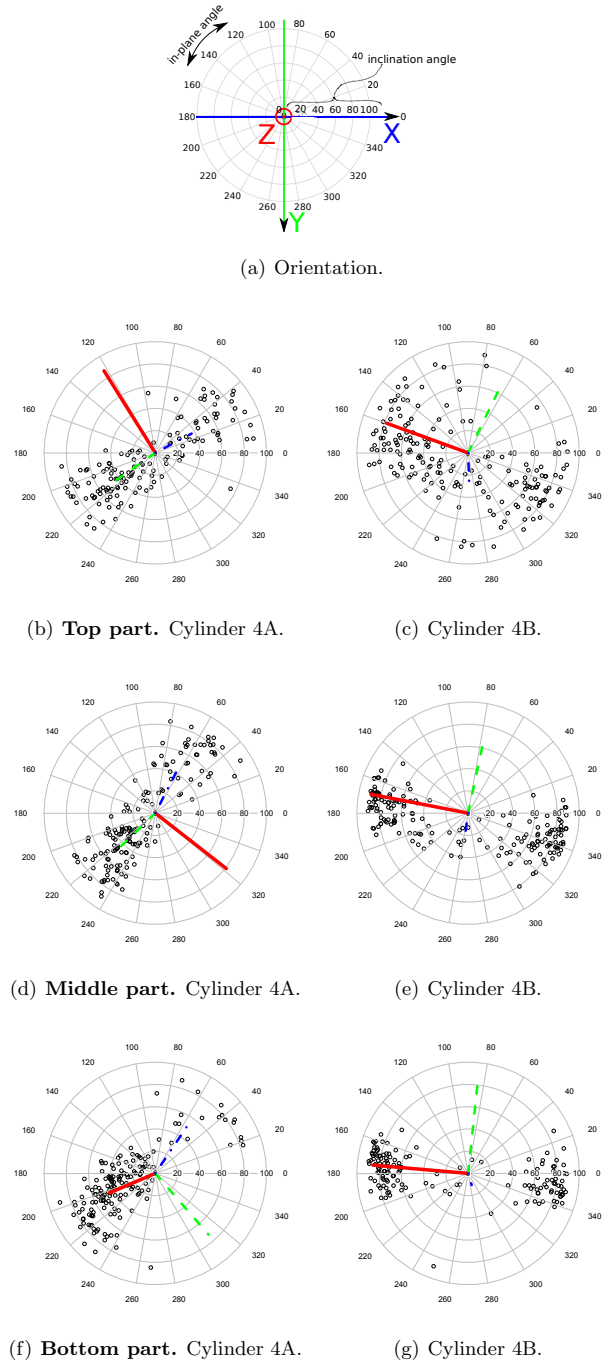


Figure A.4.2. Fibre orientation distributions with the triplets of the eigenvectors \mathbf{d}^1 , \mathbf{d}^2 , \mathbf{d}^3 for the height of the whole cylinder samples 4A and 4B. \mathbf{d}^1 -solid red line, \mathbf{d}^2 -dashed green line, \mathbf{d}^3 -dot-dashed blue line. \mathbf{d}^1 is the director corresponding to according-to-amount-largest eigenvalue. In (a) the radius represents the inclination angle θ and in-plane angle ϕ is on circumference. Z-axis corresponds to the direction of the tensile stress in a slab, Fig. 2.4.

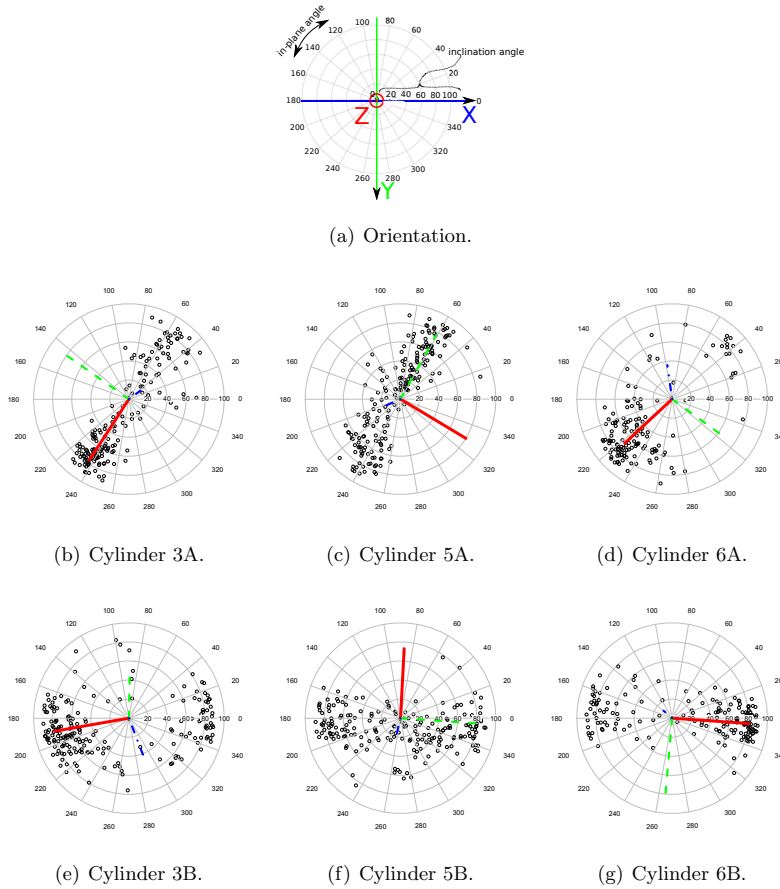


Figure A.4.3. Fibre orientation distributions with the triplets of the eigenvectors \mathbf{d}^1 , \mathbf{d}^2 , \mathbf{d}^3 for the middle parts of the cylinder samples. \mathbf{d}^1 -solid red line, \mathbf{d}^2 -dashed green line, \mathbf{d}^3 -dot-dashed blue line. \mathbf{d}^1 is the director corresponding to according-to-amount-largest eigenvalue. In (a) the radius represents the inclination angle θ and in-plane angle ϕ is on circumference. Z-axis corresponds to the direction of the tensile stress in a slab, Fig. 2.4.

A.5 Measured fibre orientation distribution functions in the tested slabs

Figs. A.5.1, A.5.2, A.5.3–A.5.5 present the approximated with the 2^{nd} order alignment tensor ODFs of fibres in the top, bottom and middle parts, respectively. The density values of the approximated ODFs are normalized according to the explanation given in Section 4.5. The orientation-weighted orthotropic elasticity of fibres in material meso-symmetry axes are calculated in the cylinder samples 3A, 3B, 5A, 5B, 6A, 6B and presented in Eqs. (A.5.1–A.5.3) employing the Kelvin-Mandel variant of the Voigt notation.

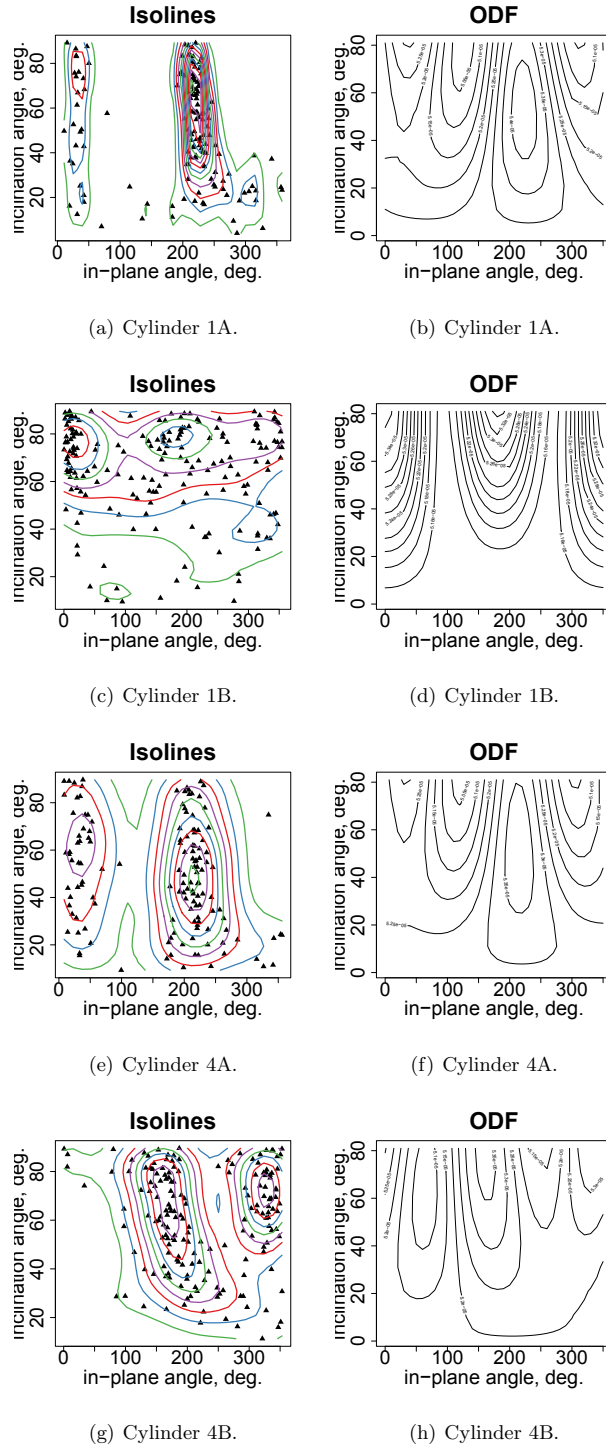


Figure A.5.1. The top parts of the cylinder samples. The isolines of the measured fibre orientation distributions and the ODFs of fibres approximated using the 2^{nd} order alignment tensor.

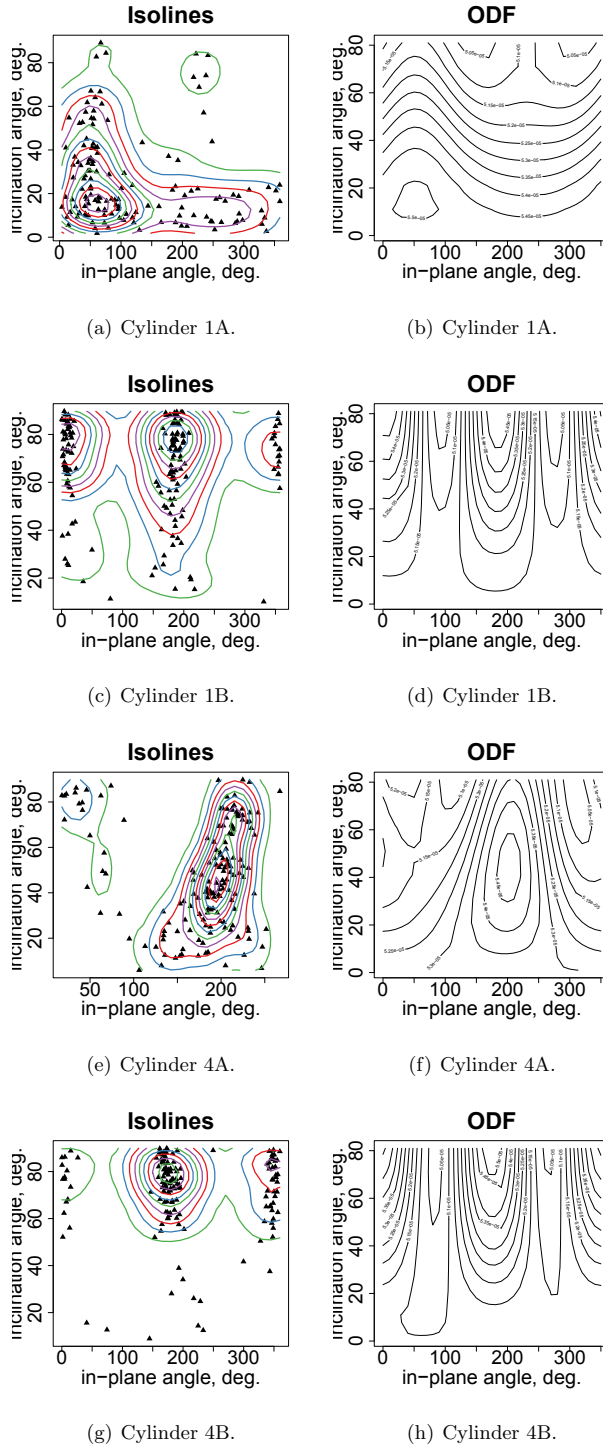


Figure A.5.2. The bottom parts of the cylinder samples. The isolines of the measured fibre orientation distributions and the ODFs of fibres approximated using the 2^{nd} order alignment tensor.

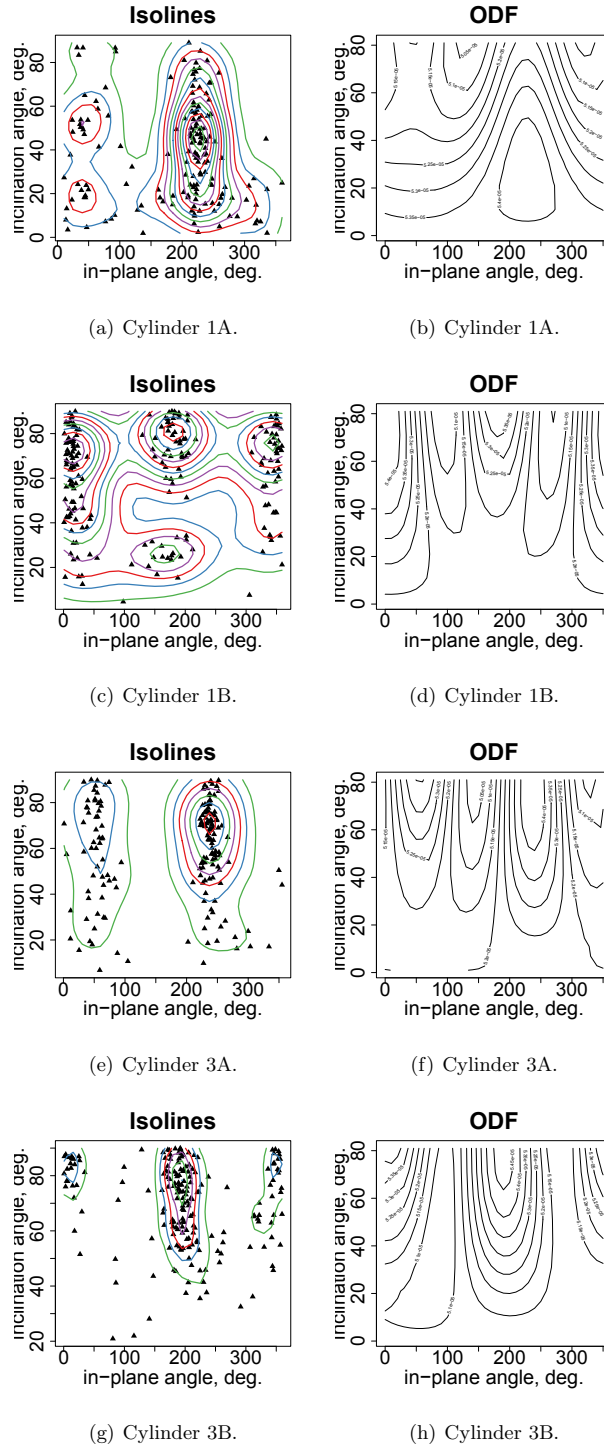


Figure A.5.3. The middle parts of the cylinder samples 1A–3B. The isolines of the measured fibre orientation distributions and the ODFs of fibres approximated using the 2nd order alignment tensor.

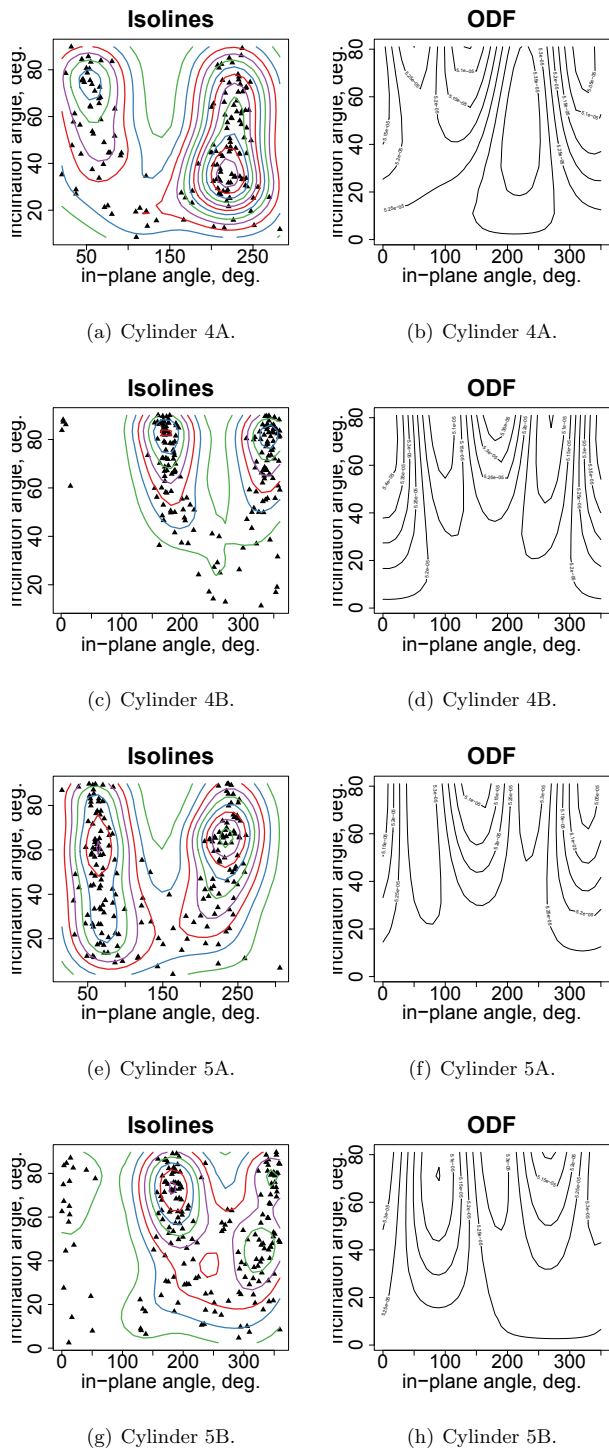


Figure A.5.4. The middle parts of the cylinder samples 4A–5B. The isolines of the measured fibre orientation distributions and the ODFs of fibres approximated using the 2nd order alignment tensor.

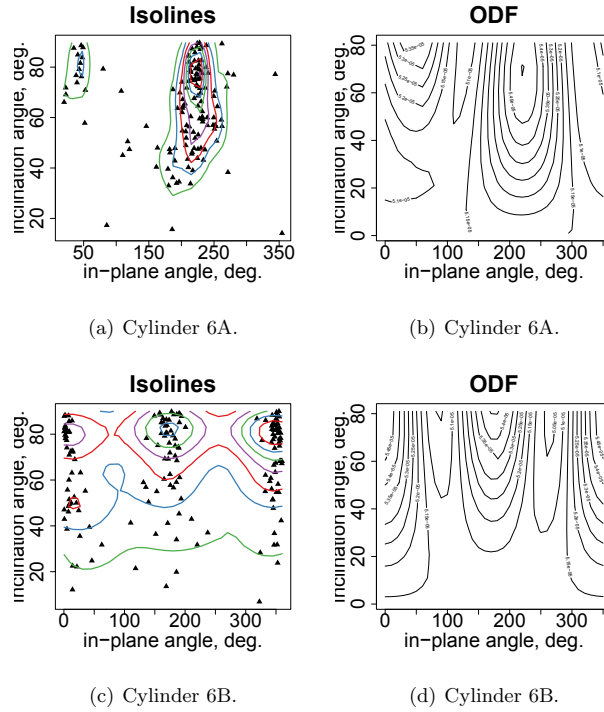


Figure A.5.5. The middle parts of the cylinder samples 6A–6B. The isolines of the measured fibre orientation distributions and the ODFs of fibres approximated using the 2^{nd} order alignment tensor.

For the middle parts of the cylinder samples 3A and 3B the orientation-weighted orthotropic meso-elasticity of fibres in material meso-symmetry axes are:

$$C_{\alpha\beta}^{(f_{ms})} = Y(f). \quad C_{\alpha\beta}^{(f_{ms})} = Y(f).$$

$$\begin{pmatrix} 0.50 & 0.07 & 0.11 & 0 & 0 & 0 \\ 0.07 & -0.06 & 0.02 & 0 & 0 & 0 \\ 0.11 & 0.02 & 0.16 & 0 & 0 & 0 \\ 0 & 0 & 0 & 0.04 & 0 & 0 \\ 0 & 0 & 0 & 0 & 0.22 & 0 \\ 0 & 0 & 0 & 0 & 0 & 0.15 \end{pmatrix}, \quad \begin{pmatrix} 0.54 & 0.09 & 0.1 & 0 & 0 & 0 \\ 0.09 & -0.01 & 0.01 & 0 & 0 & 0 \\ 0.1 & 0.01 & 0.07 & 0 & 0 & 0 \\ 0 & 0 & 0 & 0.02 & 0 & 0 \\ 0 & 0 & 0 & 0 & 0.20 & 0 \\ 0 & 0 & 0 & 0 & 0 & 0.18 \end{pmatrix}$$

(A.5.1)

For the middle parts of the cylinder samples 5A and 5B they are, respectively:

$$C_{\alpha\beta}^{(f_{ms})} = Y(f). \quad C_{\alpha\beta}^{(f_{ms})} = Y(f).$$

$$\begin{pmatrix} -0.05 & 0.05 & 0.04 & 0 & 0 & 0 \\ 0.05 & 0.37 & 0.11 & 0 & 0 & 0 \\ 0.04 & 0.11 & 0.28 & 0 & 0 & 0 \\ 0 & 0 & 0 & 0.22 & 0 & 0 \\ 0 & 0 & 0 & 0 & 0.08 & 0 \\ 0 & 0 & 0 & 0 & 0 & 0.11 \end{pmatrix}, \quad \begin{pmatrix} -0.02 & 0.06 & 0.04 & 0 & 0 & 0 \\ 0.06 & 0.36 & 0.1 & 0 & 0 & 0 \\ 0.04 & 0.1 & 0.26 & 0 & 0 & 0 \\ 0 & 0 & 0 & 0.21 & 0 & 0 \\ 0 & 0 & 0 & 0 & 0.08 & 0 \\ 0 & 0 & 0 & 0 & 0 & 0.11 \end{pmatrix}$$

(A.5.2)

and for the middle parts of the cylinder samples 6A and 6B they are:

$$\begin{aligned}
 C_{\alpha\beta}^{(fms)} = Y^{(f)}. & & C_{\alpha\beta}^{(fms)} = Y^{(f)}. \\
 \begin{pmatrix} 0.57 & 0.09 & 0.1 & 0 & 0 & 0 \\ 0.09 & -0.01 & 0.01 & 0 & 0 & 0 \\ 0.1 & 0.01 & 0.04 & 0 & 0 & 0 \\ 0 & 0 & 0 & 0.01 & 0 & 0 \\ 0 & 0 & 0 & 0 & 0.20 & 0 \\ 0 & 0 & 0 & 0 & 0 & 0.19 \end{pmatrix}, & & \begin{pmatrix} 0.56 & 0.09 & 0.11 & 0 & 0 & 0 \\ 0.09 & -0.04 & 0.01 & 0 & 0 & 0 \\ 0.11 & 0.01 & 0.09 & 0 & 0 & 0 \\ 0 & 0 & 0 & 0.01 & 0 & 0 \\ 0 & 0 & 0 & 0 & 0.21 & 0 \\ 0 & 0 & 0 & 0 & 0 & 0.17 \end{pmatrix} \\
 & & \text{(A.5.3)}
 \end{aligned}$$

Curriculum Vitae

MARIKA EIK

PERSONAL INFORMATION

DATE OF BIRTH December 11, 1976
NATIONALITY Estonian
CONTACT ☒ marika.eik@aalto.fi ☎ +372 555 68712
☒ me@cens.ioc.ee

EDUCATION

- 2009 – 2014** **Aalto University School of Engineering (AALTO)** Espoo, Finland
Department of Civil and Structural Engineering
- SUBJECT **D.Sc., Technology**
THESIS Orientation of short steel fibres in concrete: measuring and modelling
SUPERVISOR **Prof. Dr. Jari Puttonen**, jari.puttonen@aalto.fi
Department of Civil and Structural Engineering, AALTO
- 2007 – 2014** **Tallinn University of Technology (TUT)** Tallinn, Estonia
Faculty of Civil Engineering, Institute of Cybernetics at TUT
- SUBJECT **Ph.D., Engineering**
THESIS Orientation of short steel fibres in concrete: measuring and modelling
SUPERVISOR **Dr. rer. nat. Heiko Herrmann**, hh@cens.ioc.ee
Mechanics and Applied Mathematics Department, Institute of Cybernetics at TUT
- 2004 – 2007** **Tallinn University of Technology** Tallinn, Estonia
Faculty of Civil Engineering, Department of Structural Design
- SUBJECT **M.Sc., Civil Engineering**
THESIS Post-tensioned roof-ceiling project of Mikkeli's parking house
SUPERVISOR **Prof. Emeeritus Vello Otsmaa**, vello.otsmaa@ttu.ee
Faculty of Civil Engineering, Department of Structural Design, TUT
- 1999 – 2004** **Tallinn University of Technology** Tallinn, Estonia
Faculty of Civil Engineering, Department of Structural Design
- SUBJECT **Diploma *cum laude*, Civil Engineering**
THESIS Design of load-bearing structures of **Sammutin** Oy fire engines factory
SUPERVISOR **Prof. Emeeritus Vello Otsmaa**, vello.otsmaa@ttu.ee
Faculty of Civil Engineering, Department of Structural Design, TUT
- 1995–1998** **Tallinn University of Applied Sciences** Tallinn, Estonia
SUBJECT **Diploma with honours, Civil Engineering**

RESEARCH EXPERIENCE

2011 – Present **Institute of Cybernetics at TUT** Tallinn, Estonia
Mechanics and Applied Mathematics Department
SUPERVISOR **Dr. rer. nat. Heiko Herrmann**

The research is focused on the concrete reinforced by short steel fibres, SFRC. The examinations within two research branches: measuring of fibre orientations from the hardened concrete matrix and modelling of composite properties considering the anisotropic behaviour occurring due to different alignments of short steel fibres. The empirical investigations implemented include the following measuring techniques: DC-conductivity testing combined with photometry and X-ray micro-tomography scanning. The material model developed for one meso-volume element of SFRC is orthotropic linear-elastic and is valid in the case of microcracks. The model can be implemented in numerical applications. Doctor-level study project

2010 – Present **Aalto University School of Engineering** Espoo, Finland
Department of Civil and Structural Engineering
SUPERVISOR **Prof. Dr. Jari Puttonen**

The subject of the research is also focused on the concrete reinforced by short steel fibres, SFRC. Doctor-level study project

2004 – 2007 **Tallinn University of Technology** Tallinn, Estonia
Faculty of Civil Engineering, Department of Structural Design
SUPERVISOR **Prof. Emeeritus Vello Otsmaa**

The design–strength calculations–of post-tensioned cast concrete slab, simple- and continuous beams employing unbonded stressing tendons. The study of the method based on the load balancing principle, the application of the method to identify the initial necessary stressing force in a structure. Master-level studies

SCHOLARSHIPS AND AWARDS

- Jaanus Otsa doctoral Scholarship of TUT Development Foundation and TUT Alumni Association, 2012

TEACHING

- Seminars on Structural Mechanics I, TUT 2010
- Geotechnical laboratories, TUT 2008

WORK EXPERIENCE

2011 – Present **Institute of Cybernetics at TUT** Tallinn, Estonia
Mechanics and Applied Mathematics Department
POSITION **Researcher/Ph.D. student**

2010 – Present **Aalto University School of Engineering** Espoo, Finland
Department of Civil and Structural Engineering
POSITION **Doctoral Candidate**

2007 – 2009 Nordecon Betoon OÜ Tallinn, Estonia
POSITION **Project Manager/Designer**

Design of load-bearing cast concrete structures

2003 – 2007 Mittatyö Eesti OÜ Tallinn, Estonia
Yväskylä, Finland

POSITION **Project Manager/Designer**

Design of load-bearing pre-cast concrete structures

06/2003–03/2003 Neoprojekt OÜ Tallinn, Estonia
POSITION **Designer (Civil Engineering)**

01/2003–05/2003 E-Inseneribüroo OÜ Tallinn, Estonia
POSITION **Designer (Civil Engineering)**

06/2002–08/2002 E-Betoonement AS Tallinn, Estonia
POSITION **Designer (Civil Engineering)**

02/1998–08/1999 Elisor AS Tallinn, Estonia
POSITION **Assistant of surveying engineer**

Preparation and design of topological base-plans.

LANGUAGES

ESTONIAN mother tongue
RUSSIAN mother tongue
ENGLISH fluent
FINNISH good
GERMAN basic

COMPUTER SKILLS

Operating Systems	UNIX/Linux, Windows
Programming	Routine use of R, experience with Matlab, Visual Basic
Computer algebra systems	Maxima
Text processors	Routine use of LaTeX, experience with OpenOffice
Scientific and engineering software	AutoCad, Robot Structural Analysis, ImageJ

PUBLICATIONS

- M. Eik, J. Puttonen; **Challenges of steel fibre reinforced concrete in load bearing structures.** *Rakenteiden mekaniikka (Journal of Structural Mechanics)*, 44, 1, 44-64, <http://rmseura.tkk.fi/rmlehti/2011/nro1/>, June 2011
- H. Herrmann, M. Eik; **Some comments on the theory of short fibre reinforced materials.** *Proceedings of the Estonian Academy of Sciences*, 60, 3, 179-183, <http://dx.doi.org/10.3176/proc.2011.3.06>, June 2011

- M. Eik, H. Herrmann; **Raytraced images for testing the reconstruction of fibre orientation distributions.** *Proceedings of the Estonian Academy of Sciences*, 61, 2, 128-136, <http://dx.doi.org/10.3176/proc.2012.2.05>, June 2012
- J.-P. Suuronen, A. Kallonen, M. Eik, J. Puttonen, R. Serimaa, H. Herrmann; **Analysis of short fibres orientation in steel fibre reinforced concrete (SFRC) using X-ray tomography.** *Journal of Materials Science*, 48, 3, 1358-1367, <http://dx.doi.org/10.1007/s10853-012-6882-4>, February 2013
- M. Eik, K. Lõhmus, M. Tigasson, M. Listak, J. Puttonen, H. Herrmann; **DC-conductivity testing combined with photometry for measuring fibre orientations in SFRC.** *Journal of Materials Science*, 48, 10, 3745-3759, <http://dx.doi.org/10.1007/s10853-013-7174-3>, May 2013
- M. Eik, J. Puttonen, H. Herrmann; **Fibre orientation phenomenon in concrete composites: measuring and theoretical modelling.** *7th International Conference FIBRE CONCRETE 2013, Technology, Design, Application; Conference Proceedings*, 1-4, September 2013

CONFERENCE PRESENTATIONS

- | | | |
|-------------|---|------------------------|
| 2011 | 6th International Conference on Composite Structures (ICCS16) | Porto, Portugal |
| ORAL | M. Eik, H. Herrmann
Measuring Fibre Orientation in Steel Fibre Reinforced Concrete | |
| 2012 | 8th European Solid Mechanics Conference (ESMC16) | Graz, Austria |
| ORAL | M. Eik, J. Puttonen, H. Herrmann
Orientation distribution of fibres in short-fibre reinforced concrete: evaluation and introduction to constitutive relations | |
| 2013 | 7th International Conference FIBRE CONCRETE 2013 Technology, Design, Application | Prague, Czech Republic |
| ORAL | M. Eik, J. Puttonen, H. Herrmann
Fibre orientation phenomenon in concrete composites: measuring and theoretical modelling | |

EXTRAS

- Licenses** category B driver's license
Interests dog breeding, photography, yoga, travelling

MARIKA EIK

ISIKUANDMED

SÜNNIAEG 11. Detsember, 1976
SÜNNIKOHT Tallinn
KODAKONDSUS Eesti
KONTAKT ✉ marika.eik@aalto.fi ☎ +372 555 68712
✉ me@cens.ioc.ee

HARIDUSKÄIK

2009 – 2014 Aalto University School of Engineering (AALTO)
Ehitusteaduskond Espoo, Soome
ERIALA **D.Sc., Tehnikateadused**
LÕPUTÖÖ TEEMA Metallist lühikiudude orientatsioon betoonis: mõõtmise ja modelleerimine
JUHENDAJA **Prof. Dr. Jari Puttonen**, jari.puttonen@aalto.fi
Ehitusteaduskond, AALTO

2007 – 2014 Tallinna Tehnikaülikool (TTÜ) Tallinn, Eesti
Ehitusteaduskond, Küberneetika Instituut
ERIALA **Ph.D., Inseneriteadused**
LÕPUTÖÖ TEEMA Metallist lühikiudude orientatsioon betoonis: mõõtmise ja modelleerimine
JUHENDAJA **Dr. rer. nat. Heiko Herrmann**, hh@cens.ioc.ee
Mehaanika ja rakendusmatemaatika osakond, TTÜ Küberneetika Instituut

2004 – 2007 Tallinna Tehnikaülikool Tallinn, Eesti
Ehitusteaduskond, Ehitiste projekteerimise instituut
ERIALA **M.Sc., Ehitustehnika**
LÕPUTÖÖ TEEMA Mikkelil autoparkla järeltõmmatud pingearmatuuriga katuslae projekt
JUHENDAJA **Prof. Emeeritus Vello Otsmaa**, vello.otsmaa@ttu.ee
Ehitusteaduskond, Ehitiste projekteerimise instituut, TTÜ

1999 – 2004 Tallinna Tehnikaülikool Tallinn, Eesti
Ehitusteaduskond
ERIALA **Diploma cum laude, Ehitusprojekteerimine**
LÕPUTÖÖ TEEMA Sammutin Oy tuletõrjemasinate tehase kandekonstruksioonide projekt
JUHENDAJA **Prof. Emeeritus Vello Otsmaa**, vello.otsmaa@ttu.ee
Ehitusteaduskond, Ehitiste projekteerimise instituut, TTÜ

1995–1998 Tallinna Tehnikakõrgkool Tallinn, Eesti
ERIALA **Diplom kiitusega, Hoonete ehitus**

TEADUSTÖÖ KOGEVUS

2011 – ... TTÜ Küberneetika Instituut Tallinn, Eesti
Mehaanika ja rakendusmatemaatika osakond
JUHENDAJA **Dr. rer. nat. Heiko Herrmann**

Teadustöö käsitleb tsemendipõhist komposiitmaterjali, mis on moodustatud betoonmassi (matriitsi) ja lühikeste teraskiudude kokku segamisega, mille tulemuseks on teraskiudbetoon. Uuringud hõlmavad kahte teadusharu: lühikeste teraskiudude orientatsiooni jaotuse mõõtmise kivistunud betoonmatriitsis ning komposiidi omaduste modelleerimist võttes arvesse anisotroopset käitumist, mis tuleneb lühikiudude erinevast orientatsiooni jaotusest matriitsis. Empiiriliste uuringute käigus on arendatud kahte meetodit lühikiudude orientatsiooni jaotuse mõõtmiseks: alalisvoolu juhtivuse mõõtmine kombineerituna fotoanalüüsiga ning mikro-kompuutertomograafia. Teadustöö käigus välja töötatud materjalimudel ühe teraskiudbetooni meso-ruumelemendi jaoks on ortotroopne lineaarne-elastne ning kehtib mikropragude puhul. Antud materjalimudelit saab rakendada numbrilistes arvutustes.
Doktoriõpe

2010 – ... Aalto University School of Engineering Espoo, Soome
Ehitusteaduskond
JUHENDAJA **Prof. Dr. Jari Puttonen**

Teadustöö teema on samuti suunatud teraskiudbetooni uurimisele. Doktoriõpe

2004 – 2007 Tallinna Tehnikaülikool Tallinn, Eesti
Ehitusteaduskond, Ehitiste projekteerimise instituut
JUHENDAJA **Prof. Emeeritus Vello Otsmaa**

Magistritöö käsitleb järeltõmmatud armatuuriga betoonplaadi, ühe- ja mitmesildelise talade projekteerimist. Nimetatud kandekonstruktsioonid on pingestatud nakketa pingestustrossidega. Lisaks, on uuritud koormuse tasakaalustamise meetodit ja selle rakendamist esialgse algeelpingestusjõu hindamisel. Magistriõpe

STIPENDIUMID JA AUTASUD

- TTÜ Arengufond, Jaanus Otsa doktoriõppe stipendium, 2012

ÕPETUSTEGEVUS

- Seminarid Ehitusmehaanikas I, TTÜ 2010
- Geotehnikalaborid, TTÜ 2008

TEENISTUSKÄIK

2011 – ... TTÜ Küberneetika Instituut Tallinn, Eesti
Mehaanika ja rakendusmatemaatika osakond
AMETIKOHT **Teadur/doktorant**

2010 – ... Aalto University School of Engineering Espoo, Soome
Ehitusteaduskond
AMETIKOHT **Doktorant**

2007 – 2009 Nordecon Betoon OÜ Tallinn, Eesti
AMETIKOHT **Projektijuht/Projekteerija**

Monoliitraudbetoonist kandekonstruksioonide projekteerimine

2003 – 2007 Mittatyö Eesti OÜ Tallinn, Eesti
AMETIKOHT **Projektijuht/Projekteerija** Yväskylä, Soome

Kandvate raudbetoonkonstruksioonide projekteerimine (raudbetooelemendid)

06/2003–03/2003 Neoprojekt OÜ Tallinn, Eesti
AMETIKOHT **Projekteerija (Ehitus)**

01/2003–05/2003 E-Inseneribüroo OÜ Tallinn, Eesti
AMETIKOHT **Projekteerija (Ehitus)**

06/2002–08/2002 E-Betooelement AS Tallinn, Eesti
AMETIKOHT **Projekteerija (Ehitus)**

02/1998–08/1999 Elisor AS Tallinn, Eesti
AMETIKOHT **Geodeesiainseneri assistent**

Geodeetiliste alusplaanide ettevalmistamine ja vormistamine

KEELTEOSKUS

EESTI KEEL	emakeel
VEENE KEEL	emakeel
INGLISE KEEL	kõrgtase
SOOME KEEL	kesktase
SAKSA KEEL	algtase

ARVUTIOSKUS

Operatsioonisüsteemid	UNIX/Linux, Windows
Programmeerimine	R, Matlab, Visual Basic
Kompuuteralgebra süsteemid	Maxima
Tekstitöötlus	LaTeX, OpenOffice
Teadus- ja inseneritarkvara	AutoCad, Robot Structural Analysis, ImageJ

PUBLIKATSIOONID

- M. Eik, J. Puttonen; **Challenges of steel fibre reinforced concrete in load bearing structures.** *Rakenteiden mekaniikka (Journal of Structural Mechanics)*, 44, 1, 44-64, <http://rmseura.tkk.fi/rmlehti/2011/nro1/>, June 2011
- H. Herrmann, M. Eik; **Some comments on the theory of short fibre reinforced materials.** *Proceedings of the Estonian Academy of Sciences*, 60, 3, 179-183, <http://dx.doi.org/10.3176/proc.2011.3.06>, June 2011
- M. Eik, H. Herrmann; **Raytraced images for testing the reconstruction of fibre orientation distributions.** *Proceedings of the Estonian Academy of Sciences*, 61, 2, 128-136, <http://dx.doi.org/10.3176/proc.2012.2.05>, June 2012

- J.-P. Suuronen, A. Kallonen, M. Eik, J. Puttonen, R. Serimaa, H. Herrmann; **Analysis of short fibres orientation in steel fibre reinforced concrete (SFRC) using X-ray tomography.** *Journal of Materials Science*, 48, 3, 1358-1367, <http://dx.doi.org/10.1007/s10853-012-6882-4>, February 2013
- M. Eik, K. Lõhmus, M. Tigasson, M. Listak, J. Puttonen, H. Herrmann; **DC-conductivity testing combined with photometry for measuring fibre orientations in SFRC.** *Journal of Materials Science*, 48, 10, 3745-3759, <http://dx.doi.org/10.1007/s10853-013-7174-3>, May 2013
- M. Eik, J. Puttonen, H. Herrmann; **Fibre orientation phenomenon in concrete composites: measuring and theoretical modelling.** *7th International Conference FIBRE CONCRETE 2013, Technology, Design, Application; Conference Proceedings*, 1-4, September 2013

ETTEKANDED RAHVUSVAHELISTEL KONVERENTSIDEL

- 2011** *6th* **International Conference on Composite Structures (ICCS16)** Porto, Portugal
- SUULINE M. Eik, H. Herrmann
Measuring Fibre Orientation in Steel Fibre Reinforced Concrete
- 2012** *8th* **European Solid Mechanics Conference (ESMC16)** Graz, Austria
- SUULINE M. Eik, J. Puttonen, H. Herrmann
Orientation distribution of fibres in short-fibre reinforced concrete: evaluation and introduction to constitutive relations
- 2013** *7th* **International Conference FIBRE CONCRETE 2013 Technology, Design, Application** Prague, Czech Republic
- SUULINE M. Eik, J. Puttonen, H. Herrmann
Fibre orientation phenomenon in concrete composites: measuring and theoretical modelling

LISAD

- Juhiload** B-kategooria
Hobid koerte aretus, fotograafia, yoga, reisimine

List of Publications

This thesis consists of an overview and of the following publications which are referred to in the text by their Roman numerals.

**DISSERTATIONS DEFENDED AT
TALLINN UNIVERSITY OF TECHNOLOGY ON
CIVIL ENGINEERING**

1. **Heino Mölder.** Cycle of Investigations to Improve the Efficiency and Reliability of Activated Sludge Process in Sewage Treatment Plants. 1992.
2. **Stellian Grabko.** Structure and Properties of Oil-Shale Portland Cement Concrete. 1993.
3. **Kent Arvidsson.** Analysis of Interacting Systems of Shear Walls, Coupled Shear Walls and Frames in Multi-Storey Buildings. 1996.
4. **Andrus Aavik.** Methodical Basis for the Evaluation of Pavement Structural Strength in Estonian Pavement Management System (EPMS). 2003.
5. **Priit Vilba.** Unstiffened Welded Thin-Walled Metal Girder under Uniform Loading. 2003.
6. **Irene Lill.** Evaluation of Labour Management Strategies in Construction. 2004.
7. **Juhan Idnurm.** Discrete Analysis of Cable-Supported Bridges. 2004.
8. **Arvo Iital.** Monitoring of Surface Water Quality in Small Agricultural Watersheds. Methodology and Optimization of monitoring Network. 2005.
9. **Liis Sipelgas.** Application of Satellite Data for Monitoring the Marine Environment. 2006.
10. **Ott Koppel.** Infrastruktuuri arvestus vertikaalselt integreeritud raudtee-ettevõtja korral: hinnakujunduse aspekt (Eesti peamise raudtee-ettevõtja näitel). 2006.
11. **Targo Kalamees.** Hygrothermal Criteria for Design and Simulation of Buildings. 2006.
12. **Raido Puust.** Probabilistic Leak Detection in Pipe Networks Using the SCEM-UA Algorithm. 2007.
13. **Sergei Zub.** Combined Treatment of Sulfate-Rich Molasses Wastewater from Yeast Industry. Technology Optimization. 2007.
14. **Alvina Reihan.** Analysis of Long-Term River Runoff Trends and Climate Change Impact on Water Resources in Estonia. 2008.
15. **Ain Valdmann.** On the Coastal Zone Management of the City of Tallinn under Natural and Anthropogenic Pressure. 2008.
16. **Ira Didenkulova.** Long Wave Dynamics in the Coastal Zone. 2008.
17. **Alvar Toode.** DHW Consumption, Consumption Profiles and Their Influence on Dimensioning of a District Heating Network. 2008.
18. **Annely Kuu.** Biological Diversity of Agricultural Soils in Estonia. 2008.
19. **Andres Tulli.** Hiina konteinerveod läbi Eesti Venemaale ja Hiinasse tagasisaadetavate tühjade konteinerite arvu vähendamise võimalused. 2008.

20. **Heiki Onton**. Investigation of the Causes of Deterioration of Old Reinforced Concrete Constructions and Possibilities of Their Restoration. 2008.
21. **Harri Moora**. Life Cycle Assessment as a Decision Support Tool for System optimisation – the Case of Waste Management in Estonia. 2009.
22. **Andres Kask**. Lithohydrodynamic Processes in the Tallinn Bay Area. 2009.
23. **Loreta Kelpšaitė**. Changing Properties of Wind Waves and Vessel Wakes on the Eastern Coast of the Baltic Sea. 2009.
24. **Dmitry Kurennoy**. Analysis of the Properties of Fast Ferry Wakes in the Context of Coastal Management. 2009.
25. **Egon Kivi**. Structural Behavior of Cable-Stayed Suspension Bridge Structure. 2009.
26. **Madis Ratassepp**. Wave Scattering at Discontinuities in Plates and Pipes. 2010.
27. **Tiia Pedusaar**. Management of Lake Ülemiste, a Drinking Water Reservoir. 2010.
28. **Karin Pachel**. Water Resources, Sustainable Use and Integrated Management in Estonia. 2010.
29. **Andrus Räämet**. Spatio-Temporal Variability of the Baltic Sea Wave Fields. 2010.
30. **Alar Just**. Structural Fire Design of Timber Frame Assemblies Insulated by Glass Wool and Covered by Gypsum Plasterboards. 2010.
31. **Toomas Liiv**. Experimental Analysis of Boundary Layer Dynamics in Plunging Breaking Wave. 2011.
32. **Martti Kiisa**. Discrete Analysis of Single-Pylon Suspension Bridges. 2011.
33. **Ivar Annus**. Development of Accelerating Pipe Flow Starting from Rest. 2011.
34. **Emlyn D. Q. Witt**. Risk Transfer and Construction Project Delivery Efficiency – Implications for Public Private Partnerships. 2012.
35. **Oxana Kurkina**. Nonlinear Dynamics of Internal Gravity Waves in Shallow Seas. 2012.
36. **Allan Hani**. Investigation of Energy Efficiency in Buildings and HVAC Systems. 2012.
37. **Tiina Hain**. Characteristics of Portland Cements for Sulfate and Weather Resistant Concrete. 2012.
38. **Dmitri Loginov**. Autonomous Design Systems (ADS) in HVAC Field. Synergetics-Based Approach. 2012.
39. **Kati Kõrbe Kaare**. Performance Measurement for the Road Network: Conceptual Approach and Technologies for Estonia. 2013.
40. **Viktoria Voronova**. Assessment of Environmental Impacts of Landfilling and Alternatives for Management of Municipal Solid Waste. 2013.

41. **Joonas Vaabel.** Hydraulic Power Capacity of Water Supply Systems. 2013.
42. **Inga Zaitseva-Pärnaste.** Wave Climate and its Decadal Changes in the Baltic Sea Derived from Visual Observations. 2013.
43. **Bert Viikmäe.** Optimising Fairways in the Gulf of Finland Using Patterns of Surface Currents. 2014.
44. **Raili Niine.** Population Equivalence Based Discharge Criteria of Wastewater Treatment Plants in Estonia. 2014.

This doctoral thesis is conducted under a convention for the joint supervision of thesis at Aalto University (Finland) and Tallinn University of Technology (Estonia). The research implemented is concentrated on the concrete reinforced by short steel fibres, SFRC. The examinations performed comprise two research branches: measuring of fibre orientations from the hardened concrete matrix and modelling of composite properties considering the anisotropic behaviour occurring due to different alignments of short fibres.

The outcomes of empirical investigations proved that the elaborated and implemented measuring techniques: DC-conductivity testing combined with photometry and X-ray micro-tomography scanning, offer possibilities to improve and develop the manufacturing process of SFRC products (look into the summary). The advantage of the material model postulated is that it uses the full orientation information of fibres and employs tensor quantities. The model can be implemented in numerical applications.



TALLINN UNIVERSITY OF
TECHNOLOGY



ISBN 978-952-60-5591-6
ISBN 978-952-60-5592-3 (pdf)
ISBN 978-9949-23-594-0 (pdf, TUT)
ISSN-L 1799-4934
ISSN 1799-4934 (printed)
ISSN 1799-4942 (pdf)

Aalto University
School of Engineering
Department of Civil and Structural
Engineering

www.aalto.fi

**BUSINESS +
ECONOMY**

**ART +
DESIGN +
ARCHITECTURE**

**SCIENCE +
TECHNOLOGY**

CROSSOVER

**DOCTORAL
DISSERTATIONS**